A measurement of R_b at LEP2 with the ALEPH detector

Richard D. Hill

Imperial College of Science, Technology and Medicine

A thesis submitted for the degree of Doctor of Philosophy of the University of London and the Diploma of Imperial College

April 2003

A measurement of R_b at LEP2 with the ALEPH detector

Richard D. Hill
Imperial College of Science, Technology and Medicine

A thesis submitted for the degree of Doctor of Philosophy of the University of London and the Diploma of Imperial College

April 2003

ABSTRACT

This thesis presents measurements of the branching ratio R_b at the LEP2 energies of 188.6, 191.6, 195.5, 199.5, 201.6, 204.9 and 206.5 GeV using data recorded by the ALEPH detector. A combined measurement for all the data combined is also presented. The analysis uses an improved experimental method over previous LEP2 measurements. A hemisphere tag is used to calibrate an event tag, thus achieving the reliability of the hemisphere tag whilst capitalising on the higher statistical resolution afforded by the event tag. Both tags take advantage of the relatively long lifetime of B hadrons and the associated longer track impact parameters. The choice of the signal selection cut has also been improved, being based on the minimisation of the total error on R_b and thus ensuring the most accurate possible measurement. A comprehensive set of possible sources of systematic error has been evaluated. The final value for the combined 189 to 207 GeV data set is:

$$R_b \text{ at } 197.9 \text{ GeV} = 0.151 \pm 0.012 \text{ (stat)} \pm 0.007 \text{ (syst)}$$

which is within 1.05 standard deviations of the Standard Model prediction. This result is therefore not indicative of new physics.

For my Mum and Dad

Without whom this would never have been possible...

Acknowledgements

I am extremely grateful to the Imperial College High Energy Physics department for the opportunity to do this PhD. Many thanks to Julia Sedgbeer, Peter Dornan, David Websdale, Bill Cameron and Gavin Davies for all their time, help, encouragement and wisdom.

I would also like to thank the members of the ALEPH "Beyond Electroweak Working Group" for their continual peer reviews, advice and inspiration throughout my two years at CERN. Many thanks to Christoph Geweniger, Corinne Goy, Roberto Tenchini, Brigitte Bloch-Devaux, Oliver Buchmüller and Ann Moutoussi for their invaluable assistance.

Finally I must thank all those who have made the experience both here in London and in Geneva so much fun - Scott, Neil, Pete, Manni, Matt N., Matt P., Rich, Jim, Jeremy, Zaria, Jonah and of course "Elephant Halbert"!

Contents

List of Figures

List of Tables

Chapter 1

Introduction

The goal of particle physics is a complete description of the fundamental nature of our Universe. The current theoretical model of fundamental particles and their interactions is known as the *Standard Model*. However the Standard Model is believed to be far from complete. Much effort is therefore now directed at finding new physics and developing theories beyond the Standard Model.

This thesis presents an experimental measurement of the branching ratio R_b, a quantity predicted by the Standard Model which is defined as:

$$R_b = \frac{\sigma\left(\mathrm{e}^+\mathrm{e}^- \to b\overline{b}\right)}{\sigma\left(\mathrm{e}^+\mathrm{e}^- \to q\overline{q}\right)} \tag{1.1}$$

where b is the bottom or beauty quark, q refers to all quark flavours and σ is the electroweak production cross-section. The measurements of R_b presented in this thesis were made using data recorded by the ALEPH detector at CERN. During the years 1998 to 2000 ALEPH recorded approximately 20,000 electron-positron annihilations[1] in the LEP particle accelerator at energies between 189 and 207 GeV. These events in conjunction with backgrounds estimated from simulated data (Monte Carlo) were used to calculate values for R_b at the individual energy points of 188.6, 191.6, 195.5, 199.5, 201.6, 204.9 and 206.5 GeV[2]. Additionally all the data were combined in order to calculate a statistically more accurate value for R_b.

[1]This number excludes all radiative events where the interaction energy was less than 90 % of the centre-of-mass energy.

[2]For convenience, throughout this thesis the individual LEP2 energies are normally referred to by their integer values.

1.1 Motivation

The Standard Model framework allows accurate theoretical predictions for the value of R_b, at a given energy, to be calculated. Comparing the theoretical values with experimental measurements thus allows a conceptually simple method of checking the integrity of the Standard Model. Experimental measurements which are significantly different from the theoretical prediction would be evidence of new physics.

Measurements of R_b may also be used to probe for new physics at much higher energies than those at which the measurements are actually made. If the experimental values for R_b are found to agree with the theoretical predictions, this allows limits to be placed on the energy scales at which new physics could manifest itself. These energy scales are calculated within particular models for new physics such as compositeness or supersymmetry.

R_b is therefore an important quantity for particle physicists to measure. It allows both a direct test for new physics and also an indication of the energy scales at which new physics might become apparent. It is for these reasons that R_b was measured for the BEW Group at CERN.

1.2 What's new

As R_b is a powerful Standard Model test there have been many previous measurements at a variety of energies by various collaborations. In particular, precise measurements have been made at LEP1[3] where very high statistics are available (see for example references [1] and [2]). In this analysis, measurements of R_b have been made at new (higher) LEP2 energies with an improved experimental technique and analysis tools.

[3]LEP1 refers to the period from 1989 to 1995 during which the LEP machine was run at centre-of-mass energies around the value of the Z^0 vector boson mass (91.2 GeV), known as the Z^0 peak. LEP2 refers to the period post 1995 at which LEP was run at energies above the Z^0 peak up to 209 GeV in 2000.

Prior to the measurements presented in this thesis, the highest energy at which R_b had been measured by the ALEPH collaboration was 183 GeV. In this thesis new measurements for R_b beyond 183 GeV are presented. For each energy point at which LEP ran during the three years 1998 to 2000, individual values for R_b were measured. The analysis method used to measure R_b has been improved. Due to the low statistics available for each LEP2 energy point, previous measurements of R_b have used an *event* tag to identify $b\bar{b}$ events. The event tag relies on estimating the $b\bar{b}$ selection efficiency ϵ_b from Monte Carlo, whilst a *hemisphere* tag allows the $b\bar{b}$ efficiency to be measured from data[4]. Thus whilst the hemisphere tag is a much more reliable method, it suffers from a poorer statistical resolution than the event tag as two quantities (R_b and ϵ_b) are both extracted from the data. Prior to this analysis, the hemisphere tag method has only been used at LEP1, where very high statistics are available.

By combining all the available statistics between 189 and 207 GeV the use of the hemisphere tag becomes feasible. The hemisphere tag was used to calibrate the event tag results, therefore achieving the higher statistical resolution of the event tag with the reliability of the hemisphere tag. This is a considerable improvement over previous LEP2 measurements [3] which have calibrated the event tag according to an observed R_b dependence on the event thrust angle at the Z^0 peak.

An improved cut for selecting signal ($b\bar{b}$) events has been used in this analysis. Previous LEP2 measurements have used a selection cut based on maximising the signal statistical significance according to Monte Carlo. This analysis adopted a selection cut based on the minimisation of the total error on R_b as measured in data. This ensures the most accurate possible measurement with the available statistics.

The evaluation of the statistical and systematic errors has also been improved. Previous ALEPH measurements have calculated the statistical errors according to

[4]For definitions of the event and hemisphere tags (known as "b-tags"), see Chapter 4 and in particular Sections 4.6.4 and 4.6.6.

Poisson statistics. In this analysis statistical errors are evaluated according to Binomial statistics. Additional sources of uncertainty have been considered, including jet clustering and jet rate errors. The evaluation of other errors has been improved, for example the *udsc* background. The resolution of the systematic errors has also been improved by combining all the data, thus providing the best possible measurement of the systematic uncertainties. Finally, the latest ALEPH analysis software packages and Monte Carlo data sets were used throughout, ensuring the most up to date detector calibration are modelling were utilised.

1.3 Thesis overview

The contents of this thesis may be summarised as follows:

- Chapter 1 is the introduction. The analysis, its motivations and the author's contribution are defined.

- Chapter 2 provides a theoretical introduction to the Standard Model and shows how R_b may be used to put limits on new physics.

- Chapter 3 details the experimental apparatus used in the analysis. The LEP machine, ALEPH detector, Monte Carlo and `ALPHA` software framework are described.

- Chapter 4 describes the event selection procedure, the event and hemisphere tags, and the analysis methods used to extract a value for R_b.

- Chapter 5 describes an analysis of the performance of the two b-tags and impact parameter smearing using Z^0 peak calibration data. A *udsc* background check using semi-leptonic W^+W^- events is also described.

- Chapter 6 presents the results for R_b at each LEP2 energy between 189 and 207 GeV evaluated with both the event and hemisphere tags.

- Chapter 7 describes the evaluation of each systematic error considered in the analysis for both the event and hemisphere tag measurements.

- Chapter 8 describes the technique used to calibrate the event tag with the hemisphere tag, and how the statistical and systematic errors were evaluated for the calibrated results.

- Chapter 9 summarises the thesis and offers some conclusions. Suggestions for further work and future prospects are also discussed.

1.4 Testimony

This thesis in its entirety was written by the author. The author was not responsible for the development of some of the software tools used in this analysis. The `ALPHA` analysis framework, b-tag probability calculation, and smearing parameter code were all developed by the ALEPH collaboration for previous analyses. The ALEPH collaboration is also responsible for the development and production of all Monte Carlo used in this analysis. Where possible, all results, algorithms and tools for which the author is not responsible are referenced.

The author was responsible for all the experimental work, analysis and evaluation of results presented in this thesis. This includes:

- The modification of the hemisphere tag method in order to account for the additional backgrounds present at LEP2 energies compared to the Z^0 peak.

- The evaluation of the event and hemisphere b-tag performance with Z^0 peak calibration data.

- The evaluation of impact parameter smearing and the generation of smearing parameters.

- The cross-check of $udsc$ background using semi-leptonic W^+W^- events.

- Event selection, estimation of backgrounds from Monte Carlo and the evaluation of R_b using both an event and hemisphere tag for each energy point between 189 and 207 GeV and for all data combined.

- The evaluation of all systematic and statistical errors for each measurement of R_b with both the event and hemisphere tags.

- The error analysis and evaluation of the optimum selection cuts for both the event and hemisphere tags.

- The calibration of the event tag with the hemisphere tag and the final results.

The author was responsible for writing the majority of the event selection and analysis code in `FORTRAN77` and `PERL5`. All physics plots, except where referenced, were generated by the author using PAW [4]. He is indebted to his colleagues at Imperial College and at CERN without whom this analysis would not have been possible.

Chapter 2

R_b and the Standard Model

2.1 Introduction

The *Standard Model* is the basic theoretical framework describing the fundamental particles in nature and their interactions. Many observables can be calculated from the theory and thus validated with experimental measurements. The motivation therefore for particle physics experiments is to test the Standard Model, and so possibly discover new physics.

In this chapter the structure of the Standard Model, the unification of the electromagnetic and weak forces, the Higgs mechanism and generation of fermion masses are described. Possible extensions to the Standard Model are then discussed. This is followed by a description of the processes involved in the production of hadrons in e^+e^- annihilations, and finally how electroweak measurements, including R_b, may be used to put limits on the energy scales of possible new physics.

2.2 Review of the Standard Model

The goal of particle physics is a complete description of the fundamental constituents of matter and their interactions. The current theoretical model of the fundamental particles in nature is known as the Standard Model, the present form of which was completed in 1973. In a nutshell, the Standard Model is essentially the Glashow-Weinberg-Salam (GWS) electroweak model of leptons [5], extended via the Glashow-Iliopoulos-Maiani (GIM) mechanism [6] to include quarks, and thus additionally incorporates colour and the strong interaction [7]. Gravity has no role in the Standard Model as no quantum theory of gravity yet exists. However gravity is so much weaker[1] than the other forces at today's accelerator energies[2] that its effect is believed to be negligible.

To date, the Standard Model has passed every experimental test [3]. However, it is believed that the Standard Model is far from complete and probably only represents a low energy approximation of a single, unified fundamental description of nature. Many of the parameters in the Standard Model, such as the fermion masses or the (relative) strengths of the forces, are not predicted and the Standard Model therefore relies on experimental measurements for their values. There is also no explanation for why there are three generations of matter[4]. Although electromagnetism and the weak nuclear force have been successfully unified, no such unification has been achieved with the strong force which is currently "tacked on" to electroweak theory. Most tellingly, however, there is no quantum description of gravity, which must surely have a place in the Standard Model of the future.

Much effort now is therefore directed at discovering new physics beyond the Standard Model. Although any new physics must manifest itself at higher energies than is currently available in modern accelerators, the signature of such physics may well be detectable at much lower energies. However, even if no such signatures are found, this allows limits to be placed on the energy scales of possible new physics. Confirmation of all Standard Model predictions is therefore of great importance, both with respect to validating the current theory and constraining new physics at higher energies.

[1] For example the electromagnetic force is approximately 10^{36} times stronger than the gravitational force at 1 GeV.

[2] The Tevatron at Fermilab in the United States is currently the world's most energetic collider, with a centre of mass energy of $\sim$2 TeV.

[3] Although as discussed in Section 2.5.2, evidence for neutrino oscillations indicate that neutrinos carry a small mass.

[4] From analysis of the Z^0 width at LEP the number of light neutrino generations has been measured as 2.984 ± 0.008 [8].

2.3 Fundamental particles and forces

The Standard Model describes the interactions between matter particles as being mediated by force carrying "messenger" particles. All the matter particles carry spin $\frac{1}{2}$ (fermions)[5] with the force mediating particles all carrying spin 1 (bosons). The fermions are divided into *quarks* and *leptons* of which there are six of each (excluding their anti-matter partners) arranged as pairs (doublets) in three *generations*.

The leptons carry integer electric charge and the quarks carry fractional electric charge[6]. Electric charge is responsible for the *electromagnetic* force, which is mediated by the *photon*. The photon is massless[7] and electrically neutral, and is therefore stable and does not self-interact. As such the range of the electromagnetic force is infinite. The electromagnetic force binds electrons to nuclei to form atoms, and atoms together in lattices and molecules, and thus is responsible for the macroscopic structure of matter.

Quarks also carry a *colour* charge, analogous to the electric charge, which is responsible for the *strong nuclear* force. This force is mediated by the *gluon* which is also massless. However the gluons carry colour themselves and therefore self-interact. Due to this self-interaction the strength of the strong field increases with the distance between two quarks, a phenomenon known as *asymptotic freedom*. The strong force is therefore very short range. It would also appear that a result of this asymptotic freedom is *quark confinement*, meaning that coloured quarks can only ever exist in the colour neutral combinations of *baryons* and *mesons*[8]. The strong force is thus responsible for the nuclear structure of matter.

There is no charge associated with the *weak nuclear* force[9]. However all matter particles interact via the weak force, and it is this force which is responsible for nuclear beta decay. The weak force is mediated by the *intermediate vector bosons*

[5] Spin is the quantum of intrinsic angular momentum carried by a fundamental particle.
[6] In units of the electronic charge e.
[7] The current limit on the photon mass is $< 2 \times 10^{-16}$ eV [8].
[8] To date all searches for free quarks have been negative [8].
[9] Although particles interacting via the weak force are described as carrying *weak hypercharge*.

of which there are three: the W^+, W^- and Z^0. These are very massive and, with the exception of the top quark, are the heaviest fundamental particles currently confirmed to exist[10]. The weak force is therefore very short range.

Gravity is the fourth and final fundamental force. All particles with mass interact via the gravitational force which is extremely weak and infinite in range. The *graviton* is the hypothetical exchange particle mediating the force, although its existence has yet to be confirmed. Unlike electromagnetism, gravity appears to act only as an attractive force. As such this force dominates at cosmological scales and is therefore responsible for the large scale structure of the Universe.

2.4 The structure of the Standard Model

The Standard Model is a *gauge* theory describing the strong, weak and electromagnetic interactions of fundamental particles. It is based on the concept of *local gauge invariance* where, under a space-time dependent phase transformation, the Lagrangian density $\mathcal{L}$ for a field ψ remains invariant:

$$\psi \ \rightarrow \ \psi e^{ig\boldsymbol{T}\chi(x)} \ ; \ \ \delta\mathcal{L} \ = \ 0 \tag{2.1}$$

where χ is a space-time dependent phase with $x = (\boldsymbol{x}, t)$, g is a constant and $\boldsymbol{T}$ a group generator. Each force transforms according to a particular group symmetry, with the generators of the group corresponding to the mediators of the force. Thus electromagnetism with just one mediator has group symmetry U(1), the weak force with three mediators has group symmetry SU(2) and the strong force with eight gluons has group symmetry SU(3)[11].

The electromagnetic and weak forces are unified by invoking a weak *hypercharge* with symmetry U(1) and a weak *isospin* with symmetry SU(2). The three isospin fields W^a_μ $(a = 1, 2, 3)$ and one hypercharge field B_μ mix to produce the physical intermediate bosons, for which the appropriate masses are generated via Spontaneous

[10] Although data taken at LEP2 up to energies of 209 GeV have shown a 3 σ excess for the Standard Model Higgs boson with mass $M_H = 115$ GeV [9].

[11] The Special Unitary group SU(N) has N^2 - 1 generators, and the Unitary group U(N) has N^2 generators.

Fermion Generation			**Quantum Number**		
1	2	3	q	Y	I_3
		Leptons			
$\begin{pmatrix}\nu_e \\ e\end{pmatrix}_L$	$\begin{pmatrix}\nu_\mu \\ \mu\end{pmatrix}_L$	$\begin{pmatrix}\nu_\tau \\ \tau\end{pmatrix}_L$	$\begin{matrix}0 \\ -1\end{matrix}$	-1	$\begin{matrix}+\frac{1}{2} \\ -\frac{1}{2}\end{matrix}$
e_R	μ_R	τ_R	-1	-2	0
		Quarks			
$\begin{pmatrix}u \\ d\end{pmatrix}_L$	$\begin{pmatrix}c \\ s\end{pmatrix}_L$	$\begin{pmatrix}t \\ b\end{pmatrix}_L$	$\begin{matrix}+\frac{2}{3} \\ -\frac{1}{3}\end{matrix}$	$+\frac{1}{3}$	$\begin{matrix}+\frac{1}{2} \\ -\frac{1}{2}\end{matrix}$
u_R	c_R	t_R	$+\frac{2}{3}$	$+\frac{4}{3}$	0
d_R	s_R	b_R	$-\frac{1}{3}$	$-\frac{2}{3}$	0

Table 2.1: Quantum numbers for Standard Model fermions, where q is the electric charge, Y is the weak hypercharge and I_3 is the third component of isospin.

Symmetry Breaking (SSB) and the Higgs mechanism. There is no electroweak unification with the strong force, so that the overall Standard Model gauge symmetry is given by:

$$SU(3)_C \otimes SU(2)_L \otimes U(1)_Y \tag{2.2}$$

where the C refers to the colour charge of the strong force carried by quarks and gluons, L refers to the fact that the weak force only binds to isospin doublets (*isodoublets*) of left-handed particles and singlets of right-handed particles[12] and Y is the weak hypercharge. The arrangement of the fundamental fermions and their properties is shown in Table 2.1. The force-carrying mediators and their properties are shown in Table 2.2.

2.4.1 Quantum Electrodynamics

Quantum electrodynamics (QED) is the quantum field theory of electromagnetism, deriving from Maxwell's equations of electrodynamics. It is one of the most suc-

[12] In other words there are no right handed neutrinos.

Boson	Quantum Number			Mass (GeV)	Interaction
	q	Y	I_3		
W^+	$+1$	$+1$	$+\frac{1}{2}$	80.42 ± 0.06	Weak
Z^0	0	0	0	91.187 ± 0.002	Weak
W^-	-1	-1	$-\frac{1}{2}$	80.42 ± 0.06	Weak
γ	0	0	0	0	QED
g	0	0	0	0	QCD

Table 2.2: Quantum numbers for Standard Model bosons, where q is the electric charge, Y is the weak hypercharge and I_3 is the third (z) component of isospin.

cessful theoretical models of all time, agreeing with all experimental tests to a very high degree of accuracy[13]. However the QED Lagrangian can also be constructed from the requirement of local U(1) gauge invariance, and as such was the first gauge theory to be developed in the Standard Model.

The equation of motion for a free particle with mass m, spin $\frac{1}{2}$ and wavefunction ψ is given by the Dirac equation [11]:

$$(i\gamma^\mu \partial_\mu - m)\,\psi \;=\; 0 \tag{2.3}$$

where ψ is a function of space-time $x = (\boldsymbol{x}, t)$. The corresponding Lagrangian density from the Euler-Lagrange equation is

$$\mathcal{L} \;=\; \overline{\psi}\,(i\gamma^\mu \partial_\mu - m)\,\psi \tag{2.4}$$

where $\overline{\psi}$ is the complex conjugate of ψ. Under a *global* U(1) gauge transformation

$$\psi \;\rightarrow\; \psi e^{ig\chi}\;;\;\; \overline{\psi} \;\rightarrow\; \overline{\psi} e^{-ig\chi}\;, \tag{2.5}$$

where χ is independent of space-time, the exponentials cancel so that $\delta\mathcal{L} = 0$ and the Lagrangian is therefore invariant. However under a *local* U(1) gauge transformation, where the phase parameter χ is a function of space-time so that $\chi = \chi(x)$, then

$$\delta\mathcal{L} \;=\; -\,\overline{\psi}\gamma^\mu g\,(\partial_\mu \chi)\,\psi \tag{2.6}$$

[13]Probably the best known confirmation of QED is from experimental determinations of the Lamb shift. For example see [10].

and the Lagrangian is therefore no longer invariant. Gauge invariance may then be recovered by postulating a gauge field $A_\mu(x)$ with which the fermion field interacts. Adding to the Lagrangian an interaction term

$$\mathcal{L}_{\text{int}} = \overline{\psi}\gamma^\mu g A_\mu \psi \ , \tag{2.7}$$

the total Lagrangian is now given by

$$\mathcal{L} = \overline{\psi}\left[i\gamma^\mu\left(\partial_\mu - igA_\mu\right) - m\right]\psi \ , \tag{2.8}$$

which is invariant under a local U(1) transformation if the gauge field A_μ transforms as

$$A_\mu \rightarrow A_\mu + \partial_\mu \chi \ . \tag{2.9}$$

Thus demanding local U(1) gauge invariance has led to the introduction of a new gauge field A_μ with which the fermion field ψ interacts. However there must also be a term for the propagation of this new field in the Lagrangian. Defining the field strength tensor

$$F_{\mu\nu} = \partial_\mu A_\nu - \partial_\nu A_\mu \ , \tag{2.10}$$

the term $aF_{\mu\nu}F^{\mu\nu}$, where a is a constant, is gauge invariant and quadratic in the derivative of the field A_μ, and thus a suitable kinetic term. By comparison with the Lagrangian from QED[14] it can be seen that a should take the value $-\frac{1}{4}$ so that the final Lagrangian density is given by

$$\mathcal{L}_{QED} = -\frac{1}{4}F_{\mu\nu}F^{\mu\nu} + \overline{\psi}\left(i\gamma^\mu D_\mu - m\right)\psi \tag{2.11}$$

where the *covariant* derivative D_μ is defined as

$$D_\mu = \partial_\mu - igA_\mu \ . \tag{2.12}$$

The gauge field A_μ describes the photon and the constant g the coupling or interaction strength, which in QED is given by the electric charge e. The Lagrangian does not contain a mass term for the field A_μ and the addition of any such term is seen to break the gauge invariance. A massless photon can therefore be considered

[14] This is the only place that a direct comparison with QED is used, everything else being derived from the requirement of local gauge invariance.

a consequence of preserving local U(1) gauge invariance.

As the gauge transformations discussed here commute, the gauge is said to be *abelian*. The QED Lagrangian is thus a U(1) abelian gauge theory describing the motion of fermions and their electromagnetic interactions, mediated by the photon *propagator*.

2.4.2 Non-abelian gauge theories

The principle of local U(1) gauge invariance can be naturally extended to the group SU(2) which describes *isospin* transformations of a doublet field ψ_i:

$$\psi_i \;\rightarrow\; \left(e^{ig'\chi^a \boldsymbol{T}^a}\right)_i^j \psi_j \tag{2.13}$$

where g' is the isospin coupling constant and $\boldsymbol{T}^a$ ($a = 1, 2, 3$) are the three generators of SU(2), defined as one half the Pauli spin matrices. These isospin transformations do not commute and are thus known as *non-abelian* transformations. The Lagrangian density for a spin $\frac{1}{2}$ isodoublet is

$$\mathcal{L} \;=\; \overline{\psi}^i \left(i\gamma^\mu \partial_\mu - m\right) \psi_i \tag{2.14}$$

where the index i is summed over 1 and 2 for each of the isodoublet components. As in the QED case, the Lagrangian is invariant under global gauge transformations where χ is not a function of space-time. However, for a local gauge transformation:

$$\chi^a \;=\; \chi^a(x) \;; \quad \delta\mathcal{L} \;=\; -\,\overline{\psi}^i \left(\boldsymbol{T}^a\right)_i^j \gamma^\mu g' \left(\partial_\mu \chi^a\right) \psi_j \tag{2.15}$$

and therefore the Lagrangian is not locally invariant. Local gauge invariance can be restored by introducing interactions with three gauge fields A_μ^a ($a = 1, 2, 3$), one for each generator of isospin, by defining the covariant derivative as

$$\boldsymbol{D}_\mu \;=\; \left(\partial_\mu \boldsymbol{I} - ig\boldsymbol{T}^a A_\mu^a\right) \tag{2.16}$$

where $\boldsymbol{I}$ is the unit matrix and the gauge fields transform as

$$A_\mu^a \;\rightarrow\; A_\mu^a \;-\; \epsilon_{abc} A_\mu^b g' \chi^c \;+\; \partial_\mu \chi^a \quad . \tag{2.17}$$

A kinetic term is then added to the Lagrangian for the propagation of the vector fields, which is the generalised non-abelian form of the kinetic Maxwell Lagrangian known as the *Yang-Mills* Lagrangian:

$$\mathcal{L}_{\mathrm{YM}} \;=\; -\frac{1}{4}\boldsymbol{F}^{a}_{\boldsymbol{\mu\nu}}\boldsymbol{F}^{\boldsymbol{a\mu\nu}} \;;\quad \boldsymbol{F}_{\mu\nu} \;=\; -\frac{i}{g}\left[\boldsymbol{D}_\mu, \boldsymbol{D}_\nu\right] \;, \tag{2.18}$$

so that the SU(2) locally invariant Lagrangian is now given by

$$\mathcal{L} \;=-\frac{1}{4}\boldsymbol{F}^{a}_{\boldsymbol{\mu\nu}}\boldsymbol{F}^{\boldsymbol{a\mu\nu}} + \overline{\psi}^{i}\left(i\gamma^\mu \boldsymbol{D}_\mu - m\boldsymbol{I}\right)^{j}_{i}\psi_j \quad . \tag{2.19}$$

As in the QED case, the addition of a mass term for the vector fields breaks the local gauge invariance. However, experimental measurements have shown the intermediate vector bosons to be very massive. Therefore a way of breaking the symmetry and thus generating masses for the gauge bosons must be found that does not violate local gauge invariance.

2.4.3 Spontaneous symmetry breaking

A general classical Lagrangian for a complex scalar field Φ is given by [12]:

$$\mathcal{L} \;=\; \partial_\mu\Phi^*\partial^\mu\Phi - V(\Phi) \;;\quad \Phi \;=\; \frac{1}{\sqrt{2}}\left(\phi_1 + i\phi_2\right) \tag{2.20}$$

with the potential $V(\Phi)$ defined as

$$V(\Phi) \;=\; \mu^2\Phi^*\Phi + \lambda\left|\Phi^*\Phi\right|^2 \quad . \tag{2.21}$$

This Lagrangian is invariant under global U(1) transformations and, provided μ^2 is positive, has a minimum at $\Phi = 0$. This lowest energy state is known as the vacuum. However, if the sign of μ^2 is reversed so that the potential is now given by

$$V(\Phi) \;=\; -\,\mu^2\Phi^*\Phi + \lambda\left|\Phi^*\Phi\right|^2 \tag{2.22}$$

then there is no longer a minimum at $\Phi = 0$ but a *maximum*. In fact the minimum now occurs at

$$\Phi \;=\; e^{i\theta}\sqrt{\frac{\mu^2}{2\lambda}} \;;\quad 0 \le \theta \le 2\pi \tag{2.23}$$

so that there is an infinite number of possible vacuum states[15]. Any choice of vacuum state is valid and will not break the global gauge invariance. Thus, for convenience, the "true" vacuum is defined at $\theta = 0$ so that

$$\Phi \;=\; \sqrt{\frac{\mu^2}{2\lambda}} \;\equiv\; \frac{v}{\sqrt{2}} \quad . \tag{2.24}$$

Breaking the vacuum symmetry whilst maintaining gauge invariance[16] is known as *spontaneous symmetry breaking* (SSB). Small perturbations away from this chosen minimum can then be described by expanding the field:

$$\Phi \;=\; \frac{1}{\sqrt{2}}\left(v + \sigma + i\eta\right) \tag{2.25}$$

which, substituting into Equation 2.22, yields

$$V \;=\; \mu^2\sigma^2 + \mu\sqrt{\lambda}\left(\sigma^3 + \sigma\eta^2\right) + \frac{1}{4}\left(\sigma^4 + \eta^4 + 2\sigma^2\eta^2\right) - \frac{\mu^4}{4\lambda} \tag{2.26}$$

where there appears a mass term $\mu^2\sigma^2$ for the σ field, but no mass term for the η field, which is known as a *Goldstone* boson. Spontaneous symmetry breaking therefore results in the introduction of one new massive and one new massless field. However, no massless spin 0 (scalar) particles have ever been observed in nature.

2.4.4 The Higgs Mechanism

The technique of spontaneous symmetry breaking can then be extended to create massive vector bosons. In order to ensure local U(1) gauge invariance the partial derivative transforms as

$$\partial_\mu \;\rightarrow\; D_\mu \;=\; \partial_\mu - igA_\mu \tag{2.27}$$

which, including the kinetic term for the propagation of the gauge field A_μ, results in the following Lagrangian density for a Klein-Gordon field:

$$\mathcal{L} \;=\; -\frac{1}{4}F_{\mu\nu}F^{\mu\nu} \;+\; \left(D_\mu\Phi\right)^*\left(D^\mu\Phi\right) \;-\; V(\Phi) \quad . \tag{2.28}$$

[15]The vacuum is *degenerate*.

[16]In other words a theory where the vacuum has less symmetry than the Lagrangian.

Substituting Equation 2.25 into the kinetic term for the Φ field then gives

$$\begin{aligned}
(D_\mu\Phi)^*(D^\mu\Phi) &= \frac{1}{2}\partial_\mu\sigma\partial^\mu\sigma + \frac{1}{2}\partial_\mu\eta\partial^\mu\eta \\
&+ \frac{1}{2}g^2v^2A_\mu A^\mu + gvA^\mu\partial_\mu\eta \\
&- gA^\mu(\eta\partial_\mu\sigma - \sigma\partial_\mu\eta) + \frac{1}{2}g^2A_\mu A^\mu\left(\eta^2+\sigma^2\right) \\
&+ \ldots \qquad (2.29)
\end{aligned}$$

where it can be seen that the gauge boson A_μ has gained a mass term $M_{A_\mu} = gv$. There is also a term $gvA^\mu\partial_\mu\eta$ which is hard to interpret. However, the originally massless gauge boson has only two degrees of freedom, but a massive gauge boson should have three degrees of freedom. If the expansion about the vacuum is rewritten

$$\Phi = \frac{1}{\sqrt{2}}(v+\sigma)e^{i\frac{\eta}{v}}\ , \qquad (2.30)$$

which is valid for any v and small η, σ, then the gauge boson can gain a third degree of freedom by making the transformation

$$A_\mu \rightarrow A_\mu + \frac{1}{gv}\partial_\mu\eta\ . \qquad (2.31)$$

Substituting Equations 2.30 and 2.31 into the kinetic and potential terms for the field Φ results in the following Lagrangian:

$$\begin{aligned}
\mathcal{L} &= -\frac{1}{4}F_{\mu\nu}F^{\mu\nu} + \frac{1}{2}\partial_\mu\sigma\partial^\mu\sigma + \frac{1}{2}g^2v^2A_\mu A^\mu \\
&+ \frac{1}{2}g^2\sigma^2A_\mu A^\mu + g^2v\sigma A_\mu A^\mu + \lambda\left(v^2\sigma^2 + v\sigma^3\right) \\
&+ \ldots \qquad (2.32)
\end{aligned}$$

where it can be seen there is a mass term for the gauge field A_μ, a massive σ field and no η field. Spontaneous symmetry breaking and the Higgs mechanism have therefore generated mass for the gauge field, but at the expense of introducing the additional σ field with spin 0. This of course is the *Higgs* boson. The Goldstone boson η has been absorbed or *eaten* by the now massive gauge field in gaining a third degree of freedom.

The expansion about the minimum in Equation 2.30 and the gauge transformation in Equation 2.31 is the equivalent of choosing a gauge. Choosing $\eta = 0$, so that

$$\Phi = \frac{1}{\sqrt{2}}(v + \sigma) \ , \tag{2.33}$$

is known as the *unitary* gauge. Substituting this into Equation 2.28 results in the Lagrangian of Equation 2.32. The unitary gauge is then used for the Higgs mechanism in electroweak theory.

This example has demonstrated how mass may be generated for a gauge boson. This technique is therefore used not to generate a massive photon, which is assumed massless in the Standard Model, but to generate masses for the three gauge bosons introduced in maintaining local SU(2) gauge invariance.

2.5 Electroweak unification

Glashow-Weinberg-Salam electroweak theory unifies the electromagnetic and weak forces by invoking a weak hypercharge with group symmetry U(1) and weak isospin with group symmetry SU(2). The SU(2) $\otimes$ U(1) electroweak covariant derivative is defined as [13]:

$$D_\mu = \partial_\mu - ig\boldsymbol{T}^a W_\mu^a - ig'\frac{\boldsymbol{Y}}{2}B_\mu \tag{2.34}$$

where $\boldsymbol{T}^a$ ($a = 1, 2, 3$) and $\boldsymbol{Y}$ are respectively the three generators of SU(2) isospin and one generator of U(1) hypercharge. The three isospin gauge bosons and one hypercharge gauge boson are donated by W_μ^a and B_μ which transform as

$$\begin{aligned} W_\mu^a &\rightarrow W_\mu^a + \frac{1}{g}\partial_\mu \alpha^a - \epsilon_{abc}\alpha^b W_\mu^c \\ B_\mu &\rightarrow B_\mu + \frac{1}{g'}\partial_\mu \beta \end{aligned} \tag{2.35}$$

where g, g' are the isospin and hypercharge coupling constants respectively, α^a ($a = 1, 2, 3$) are the three SU(2) phases and β is the U(1) phase.

2.5.1 The electroweak Higgs mechanism

The masses of the gauge bosons are generated via spontaneous symmetry breaking and the Higgs mechanism as outlined in Sections 2.4.3 and 2.4.4. Starting with the Klein-Gordon Lagrangian for a complex scalar doublet [12]:

$$\mathcal{L}_{\text{Higgs}} = (D^\mu \Phi)^\dagger (D_\mu \Phi) - \mu^2 \Phi^\dagger \Phi - \lambda \left(\Phi^\dagger \Phi\right)^2 \ , \tag{2.36}$$

where

$$\Phi = \begin{pmatrix} \phi^+ \\ \phi^0 \end{pmatrix} \tag{2.37}$$

and the vacuum is chosen to be

$$\Phi = \begin{pmatrix} 0 \\ \frac{v}{\sqrt{2}} \end{pmatrix} \tag{2.38}$$

with v having the definition given in Equation 2.24. Expanding about the physical vacuum leads to

$$\Phi = \frac{1}{\sqrt{2}} \begin{pmatrix} \sigma_1 + i\eta_1 \\ v + \sigma_2 + i\eta_2 \end{pmatrix} \tag{2.39}$$

which, when working in the unitary gauge, reduces to

$$\Phi = \frac{1}{\sqrt{2}} \begin{pmatrix} 0 \\ v + H \end{pmatrix} \tag{2.40}$$

where H is the Higgs field. Inserting this into the Higgs Lagrangian of Equation 2.36 results in the following terms:

$$\begin{aligned} \mathcal{L}_{\text{Higgs}} &= \frac{1}{2}\partial_\mu H \partial^\mu H - \mu^2 H^2 \\ &+ \frac{1}{8} g^2 v^2 W^1_\mu W^{\mu 1} + \frac{1}{8} g^2 v^2 W^2_\mu W^{\mu 2} \\ &+ \frac{1}{8} v^2 \left(g W^3_\mu - g' B_\mu\right)\left(g W^{\mu 3} - g' B^\mu\right) + ... \end{aligned} \tag{2.41}$$

where it can be seen that there is a Higgs field with mass $\sqrt{2}\mu$ and $g^2 v^2$ mass terms for the W^1_μ and W^2_μ fields. The physical gauge fields are obtained by rotating the isospin gauge fields

$$W^\pm_\mu = \frac{1}{\sqrt{2}} \left(W^1_\mu \pm i W^2_\mu\right) \tag{2.42}$$

resulting in a mass $M_{W^\pm} = gv/2$. Defining the Weinberg angle, θ_W, by

$$\frac{g'}{g} = \tan\theta_W \ , \tag{2.43}$$

so that

$$\cos\theta_W = \frac{g}{(g^2+g'^2)^{\frac{1}{2}}} \; ; \quad \sin\theta_W = \frac{g'}{(g^2+g'^2)^{\frac{1}{2}}} \; , \tag{2.44}$$

leads to the following definitions for the physical fields

$$\begin{aligned} Z_\mu &= \cos\theta_W W_\mu^3 - \sin\theta_\mu B_\mu \\ A_\mu &= \sin\theta_W W_\mu^3 + \cos\theta_\mu B_\mu \quad . \end{aligned} \tag{2.45}$$

The masses are given by

$$M_{Z_\mu} = \frac{1}{2} v \left(g^2 + g'^2\right)^{\frac{1}{2}} \; ; \quad M_{A_\mu} = 0 \; , \tag{2.46}$$

so that the masses of the $W_\mu^\pm$ and Z_μ are therefore related by

$$\frac{M_{W_\mu^\pm}}{M_{Z_\mu}} = \cos\theta_W \quad . \tag{2.47}$$

The Higgs Lagrangian therefore results in terms for the gauge and Higgs boson couplings and their masses. The Lagrangian for the propagation of the gauge fields is

$$\mathcal{L}_{\text{Gauge}} = -\frac{1}{4} \boldsymbol{W}_{\mu\nu} \boldsymbol{W}^{\mu\nu} - \frac{1}{4} B_{\mu\nu} B^{\mu\nu} \; , \tag{2.48}$$

which is added to the Higgs Lagrangian. Thus the gauge and Higgs sector of the electroweak Lagrangian is given by

$$\mathcal{L}_{EW} = \mathcal{L}_{\text{Higgs}} + \mathcal{L}_{\text{Gauge}} \tag{2.49}$$

in which the kinetic term for the W_μ fields contains gauge boson self-interaction terms resulting from the non-abelian nature of SU(2) transformations.

2.5.2 Fermion dynamics and masses

In the Standard Model parity is *maximally* violated in the weak sector [12]. Weak isospin does not couple to right-handed particles so that left-handed particles transform as doublets and right-handed particles transform as singlets. The grouping of the left-handed doublets and right-handed singlets is shown in Table 2.1. Left and right-handed fermion fields thus transform as:

$$\begin{aligned} \psi_L &\rightarrow \exp\left(ig\boldsymbol{T}^a\alpha^a + ig'\boldsymbol{Y}\beta\right)\psi_L \\ \psi_R &\rightarrow \exp\left(ig'\boldsymbol{Y}\beta\right)\psi_R \end{aligned} \tag{2.50}$$

where α^a and β are the space-time dependent isospin and hypercharge phase angles. A fermion field ψ can be expressed as a sum of its left and right-handed components:

$$\psi = \psi_L + \psi_R \tag{2.51}$$

so that the Dirac Lagrangian for a *massless* fermion,

$$\overline{\psi} i\gamma^\mu \partial_\mu \psi , \tag{2.52}$$

when split into its left and right-handed components becomes

$$\overline{\psi}_L i\gamma^\mu \partial_\mu \psi_L + \overline{\psi}_R i\gamma^\mu \partial_\mu \psi_R \tag{2.53}$$

which, due to the separation of the left and right-handed components, is gauge invariant under the transformations of Equation 2.50 when the partial derivatives are replaced with the covariant derivatives. The Lagrangian for the propagation of massless fermions is therefore

$$\mathcal{L}_f = \overline{\psi}_L i\gamma^\mu D_\mu \psi_L + \overline{\psi}_R i\gamma^\mu D_\mu \psi_R \tag{2.54}$$

where

$$\begin{aligned} D_\mu \psi_L &= \left(\partial_\mu - ig\boldsymbol{T}^a W_\mu^a - ig'\frac{\boldsymbol{Y}}{2}B_\mu\right)\psi_L \\ D_\mu \psi_R &= \left(\partial_\mu - ig'\frac{\boldsymbol{Y}}{2}B_\mu\right)\psi_R \end{aligned} \tag{2.55}$$

which is summed over all quarks and leptons. The total electroweak Lagrangian is therefore given by

$$\mathcal{L}_{EW} = \mathcal{L}_{\text{Higgs}} + \mathcal{L}_{\text{Gauge}} + \mathcal{L}_f , \tag{2.56}$$

which does not yet include any mass terms for the fermions. However, a mass term $m\overline{\psi}\psi$ split into its left and right-handed components becomes

$$m\overline{\psi}\psi = m\left(\overline{\psi}_L\psi_R + \overline{\psi}_R\psi_L\right) , \tag{2.57}$$

which is *not* gauge invariant under the transformations of Equation 2.50 due to the left-right mixing. Thus the Dirac Lagrangian is only gauge invariant for massless fermions. The Higgs mechanism is therefore extended to give masses to the fermions in a gauge invariant manner.

The masses of the fermions are generated by $Yukawa$ couplings [12] to the Higgs field and take the form

$$g_f\left(\overline{\psi}_L\Phi\psi_R+\overline{\psi}_R\Phi^\dagger\psi_L\right) \tag{2.58}$$

where g_f is the Yukawa constant for the coupling of the fermion field ψ to the Higgs field Φ. Breaking the vacuum symmetry, Equation 2.58 is evaluated as

$$g_e\left[(\overline{\nu}_e,\overline{e})_L\left(\begin{array}{c}0\\ v/\sqrt{2}\end{array}\right)e_R+\overline{e}_R\left(0,v/\sqrt{v}\right)\left(\begin{array}{c}\overline{\nu}_e\\ \overline{e}\end{array}\right)_L\right] = \frac{g_e v}{\sqrt{2}}\overline{e}e \tag{2.59}$$

for the first generation lepton doublet and is representative of the electron mass if $g_e = m_e\sqrt{2}/v$. The masses of the fermions are therefore proportional to their Yukawa couplings to the Higgs field. No terms for neutrino masses appear which is not a problem if neutrinos are really massless. However, recent experimental evidence for neutrino mixing suggests that neutrinos do in fact have a small mass [14]. Additionally in the quark sector both members of the doublet are massive so that Equation 2.58 will not generate the appropriate mass terms for both doublet members. Thus this fermion mass generation technique must at least be modified for the quark sector, if not for the lepton sector as well. It can be shown that the conjugate of the Higgs doublet

$$\Phi_c = \left(\begin{array}{c}\overline{\phi}^0\\ -\phi^-\end{array}\right) \rightarrow \left(\begin{array}{c}v/\sqrt{2}\\ 0\end{array}\right) \tag{2.60}$$

is a valid isodoublet which, when substituted into Equation 2.58, produces

$$g_{\nu_e}\left[(\overline{\nu}_e,\overline{e})_L\left(\begin{array}{c}v/\sqrt{2}\\ 0\end{array}\right)\nu_{eR}+\overline{\nu}_{eR}\left(v/\sqrt{v},0\right)\left(\begin{array}{c}\overline{\nu}_e\\ \overline{e}\end{array}\right)_L\right] = \frac{g_{\nu_e} v}{\sqrt{2}}\overline{\nu}_e\nu_e \tag{2.61}$$

for the first generation doublet where a neutrino mass term has now been produced. Equation 2.58 can then be used to generate as many lepton and neutrino mass terms as required. Exactly the same principle is then applied to the quark sector, with terms being added by hand for each doublet generation.

A generalisation of the above mass production can then be used to parameterise generation mixing in charged current interactions. The $W^\pm$ boson does not have to couple to quarks within the same generation and as such the weak force is said to couple to weak eigenstates and not mass eigenstates. The weak and mass eigenstates are related by the *Cabibbo Kobayashi Maskawa* (CKM) [15] mixing matrix $\boldsymbol{V}_{\mathrm{CKM}}$ as follows

$$\begin{pmatrix} d' \\ s' \\ b' \end{pmatrix} = \boldsymbol{V}_{\mathrm{CKM}} \begin{pmatrix} d \\ s \\ b \end{pmatrix} \tag{2.62}$$

where d', s', b' are the weak eigenstates, d, s, b are the mass eigenstates and $\boldsymbol{V}_{\mathrm{CKM}}$ is a 3×3 unitary matrix in which each element donates the relative Yukawa couplings. There is no mixing (at least at tree level) for neutral current processes mediated by the Z^0, which is described by the Glashow-Iliopoulos-Maiani (GIM) Mechanism. The final electroweak Lagrangian is thus given by:

$$\mathcal{L}_{EW} = \mathcal{L}_{\mathrm{Higgs}} + \mathcal{L}_{\mathrm{Gauge}} + \mathcal{L}_f \tag{2.63}$$

where $\mathcal{L}_f$ now contains terms for both fermion dynamics and the fermion masses.

2.6 Quantum Chromodynamics

In addition to the electroweak force the Standard Model also describes the strong force. The gauge theory of the strong force is known as Quantum Chromodynamics (QCD), so called because it describes the interactions of *coloured* fermions. There are three colour charges[17] (plus their anti-colour counterparts) so that QCD describes the strong force in terms of colour triplets with an SU(3) group symmetry. The construction of the Lagrangian is a analogous to the U(1) and SU(2) cases, except that now 8 gauge fields are required to maintain local gauge invariance. These eight gauge fields are called gluons and, due to the non-abelian nature of SU(3), themselves carry colour and therefore self-interact. The QCD Lagrangian is given by [12]:

$$\mathcal{L}_{QCD} = -\frac{1}{4}\sum_{A=1}^{A=8} F^{A\mu\nu}F^{A}_{\mu\nu} + \sum_{j=1}^{j=n_f} \overline{q}_j \left(i\gamma^\mu D_\mu - m_j\right) q_j \tag{2.64}$$

where q_j are the quark fields, n_f is the number of quark flavours and D_μ is the SU(3) covariant derivative. Gluons are massless so no symmetry breaking is required. The

[17] Red, green and blue, with colour singlets being white.

total Standard Model Lagrangian is therefore given by

$$\mathcal{L}_{SM} = \mathcal{L}_{QCD} + \mathcal{L}_{EW} \tag{2.65}$$

where $\mathcal{L}_{EW}$ is defined in Equation 2.63.

2.7 Standard Model Summary

The Standard Model Lagrangian contains terms for the masses, propagation and interactions via the electromagnetic, weak and strong forces for all the fermions, vector gauge bosons and the scalar Higgs boson. However, as discussed in Section 2.2, it is believed the Standard Model is far from being the complete picture. The Standard Model certainly has a predictive power[18], yet currently requires 18 parameters to be input by hand. These are as follows:

- The coupling strengths g', g and α_s of the electromagnetic, weak and strong interactions.
- The mass of the Higgs boson, M_H, and the vacuum expectation value, v.
- The Yukawa couplings for the nine massive fermions.
- The four parameters from which the elements of the CKM matrix are composed.

This large number of free parameters is therefore a strong indication that the Standard Model in its current form is not the final theory. Much effort now is therefore directed at developing theories which can constrain the number of free parameters in the Standard Model.

2.8 Physics beyond the Standard model

The belief that there is physics beyond the Standard Model has many justifications. As discussed in Section 2.7, there are a number of parameters not predicted by the theory which need to be input by hand: it is generally believed that so called

[18]For example the relative masses of the Z^0 and $W^\pm$ gauge bosons.

Theories of Everything (TOEs) should not contain any arbitrary parameters. Additionally the Standard Model is believed to be incomplete for the following main reasons:

- No unification between the strong and electroweak forces.
- No quantum theory of gravity
- No explanation for the three generations of matter.
- Although the Higgs mechanism works, it does so at the expense of introducing an arbitrary extra scalar boson. This may be correct, but there is no explanation as to why it should be.

Apart from the apparent lack of completeness in the Standard Model, there are also other unanswered questions such as:

- What is the connection between quarks and leptons ?
- Are the fermions and/or gauge bosons fundamental particles or are they composites ?
- Is there likely to be any new physics between the currently probed scale of $\sim$100 GeV and the Planck scale of $\sim 10^{19}$ GeV at which all the forces, including gravity, are unified ?

In an attempt to address some of these problems four main approaches to physics beyond the Standard Model are being developed. These are extended gauge theories, supersymmetry, technicolour and composite models.

2.8.1 Extended gauge theories

Currently there is no unification between the electroweak and strong forces as the coupling constants of these interactions appear to be independent. Extended gauge theories attempt to unify the forces by proposing a single gauge group so that all the forces are described by a single coupling constant [11]. In such a theory the Standard Model gauge group $SU(3) \otimes SU(2) \otimes U(1)$ is thus a subgroup of the unifying gauge group. However, a consequence of a single unifying gauge group is the addition of new vector bosons. The group $SU(5)$ for example requires 24 vector bosons, twice as many as are currently observed to exist.

2.8.2 Supersymmetry

Supersymmetry [16] is an attempt to solve the *hierarchy* or *naturalness* problem in the Higgs sector. The fundamental mass scale in physics appears to the Planck mass, $M_{\text{Planck}} \sim 10^{19}$ GeV, where the strengths of all the forces are unified. The Higgs mass is expected to be of the order of the electroweak unification energy which is ~ 100 GeV. However, radiative corrections to the Higgs mass at the Planck scale are approximately 30 orders of magnitude greater than the Higgs mass at the electroweak scale. Supersymmetry describes a new symmetry where all fermions have a bosonic partner and all bosons have a fermionic partner, thus introducing a new set of super-particles or *sparticles*. The radiative corrections to the Higgs mass at the Planck scale from particles are cancelled by the equal and opposite corrections from the sparticles. So although supersymmetry provides a solution to the hierarchy problem and naturally results in a light Higgs, it necessitates the introduction of a whole new set of particles.

2.8.3 Technicolour

Technicolour [17] is a non-abelian gauge theory describing the interactions of massless *technifermions* which proposes an alternative to the Higgs boson mediated electroweak symmetry breaking. Goldstone-like *technipions* comprised of confined technifermions are "eaten" in spontaneous symmetry breaking to give masses to the gauge bosons. The main phenomenological implication of technicolour is that the weak and strong forces are unified at approximately 500 GeV. Although the theory describes symmetry breaking and can unify the weak and strong forces there are several problems. Additional *extended* technicolour interactions have to be introduced to give masses to the fermions and, to date, experimental evidence is in disagreement with technicolour predictions.

2.8.4 Composite models

Composite models are theories where apparently fundamental particles are composed of smaller constituents. Composite theories can essentially be divided into two classes: those where the massive gauge bosons are composite, and those where the fermions are composite. This second class explains the second and third generations of matter as being excited states of the first generation.

2.9 The $e^+e^- \to \overline{q}q$ process.

The analysis presented in this thesis is a measurement of the branching ratio R_b, which is defined as the ratio of the $b\overline{b}$ and $q\overline{q}$ production cross-sections. The motivation for this measurement is to test the integrity of the Standard Model and enable limits to be placed on possible new physics. The $b\overline{b}$ and $q\overline{q}$ cross-sections must therefore be calculated from the Standard Model in order to compare the theory with the experimental results. Cross-section calculations are also used in the generation of simulated data (Monte Carlo), which is used to estimate background contributions to the measured signal.

At LEP2 the production of quark pairs in e^+e^- annihilations is mediated by the exchange of either a photon or a Z^0 boson. *Zeroth order* or *tree level*[19] Feynman diagrams for both processes are shown in Figure 2.1. Each must be included in the calculation of the $q\overline{q}$ or $b\overline{b}$ cross-sections.

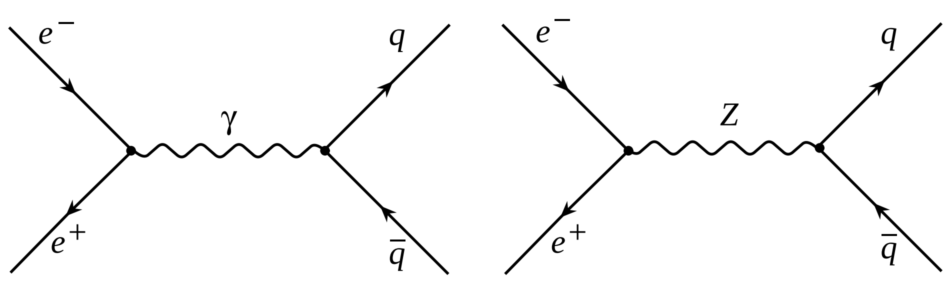

Figure 2.1: Tree level Feynman diagrams for the process $e^+e^- \to q\overline{q}$ at LEP2.

[19]The zeroth order or tree level process refers to the basic production mechanism with no higher order corrections.

2.9.1 The Born level differential cross-section

The generic expression for a scattering process $1 + 2 \to 3 + 4$ is given by [18]:

$$\mathrm{d}\sigma = \frac{(2\pi)\,\delta^4\,(p_i - p_f)\,|\mathcal{M}_{fi}|^2}{4\left[(p_1 \cdot p_2)^2 - (m_1 m_2)^2\right]^{\frac{1}{2}}} \prod_{j=3}^{j=4} \frac{\mathrm{d}^3 p_j}{(2\pi)^3\, 2E_j} \tag{2.66}$$

where p_i and p_f are the total four momenta of the initial electrons and final quarks respectively, m_1 and m_2 are the masses of the incoming electrons and E_j, p_j are the energy and momentum of each final state quark. The *matrix* element $\mathcal{M}_{fi}$ describes the amplitude for the transition from initial to final state which is given by

$$\mathcal{M}_{fi} = \mathcal{M}_\gamma + \mathcal{M}_{\mathrm{NC}} \tag{2.67}$$

where $\mathcal{M}_\gamma$ is the amplitude for the photon mediated transition and $\mathcal{M}_{\mathrm{NC}}$ is the amplitude for the neutral current (Z^0) transition. These matrix elements can then be determined from the Feynman rules (for example see [19]).

The Born level differential cross-section allows the total cross-section for a particular process at tree level to be calculated. However for real world predictions, the higher order corrections must also be included in the calculation. These are included in the *Improved* Born Approximation (IBA). Higher order corrections are described in the following section.

2.9.2 Higher order corrections

The diagrams discussed in the previous section represent only the tree level or *Born* level contributions to the $e^+e^- \to \overline{q}q$ process. In reality there are additional *higher order* corrections which also contribute. These may be divided into electroweak corrections and radiative corrections.

Electroweak corrections

Electroweak corrections may be further divided into propagator or *vacuum polarisation* corrections, vertex corrections and box corrections.

- **Vacuum polarisation corrections**

  These corrections refer to loops of virtual[20] particles in the propagator. The size of the correction depends on the mass of the particles in the loop. Figure 2.2 a) shows examples of first order propagator corrections. All vacuum polarisation corrections are independent of experimental cuts.

- **Vertex corrections**

  These corrections refer to additional contributions to the vertices. They are independent of experimental cuts, but not independent of the flavour of the initial or final state fermions. Examples of first order vertex corrections are shown in Figure 2.2 b).

- **Box corrections**

  These corrections refer to contributions in which more than one Z^0 or $W^{\pm}$ is exchanged. Before the Z^0Z^0 or $W^{\pm}W^{\pm}$ production thresholds their contribution is negligible. However at LEP2 energies their significance increases up to approximately 2-3%. These corrections are also independent of experimental cuts. Examples of box corrections are shown in Figure 2.2 c).

The examples shown in Figure 2.2 only show first order corrections. However these corrections contribute $ad\ infinitum$, with each additional vertex contributing a factor of the coupling constant α less. As α is fairly small, accurate calculations can be achieved by considering just first and second order corrections.

Radiative corrections

Radiative corrections are QED corrections corresponding to the emission of real photons from the incoming and outgoing fermions. Also included in this class of corrections are vertex and box corrections corresponding to the exchange of virtual photons. Examples of first order radiative corrections are shown in Figure 2.3.

Including first and second order electroweak and radiative corrections allows accurate predictions for $e^+e^- \rightarrow q\overline{q}$ cross-sections to be calculated. These predictions

[20] A virtual particle is defined as being off the mass shell, in other words does not carry the same mass as a free or "real" particle.

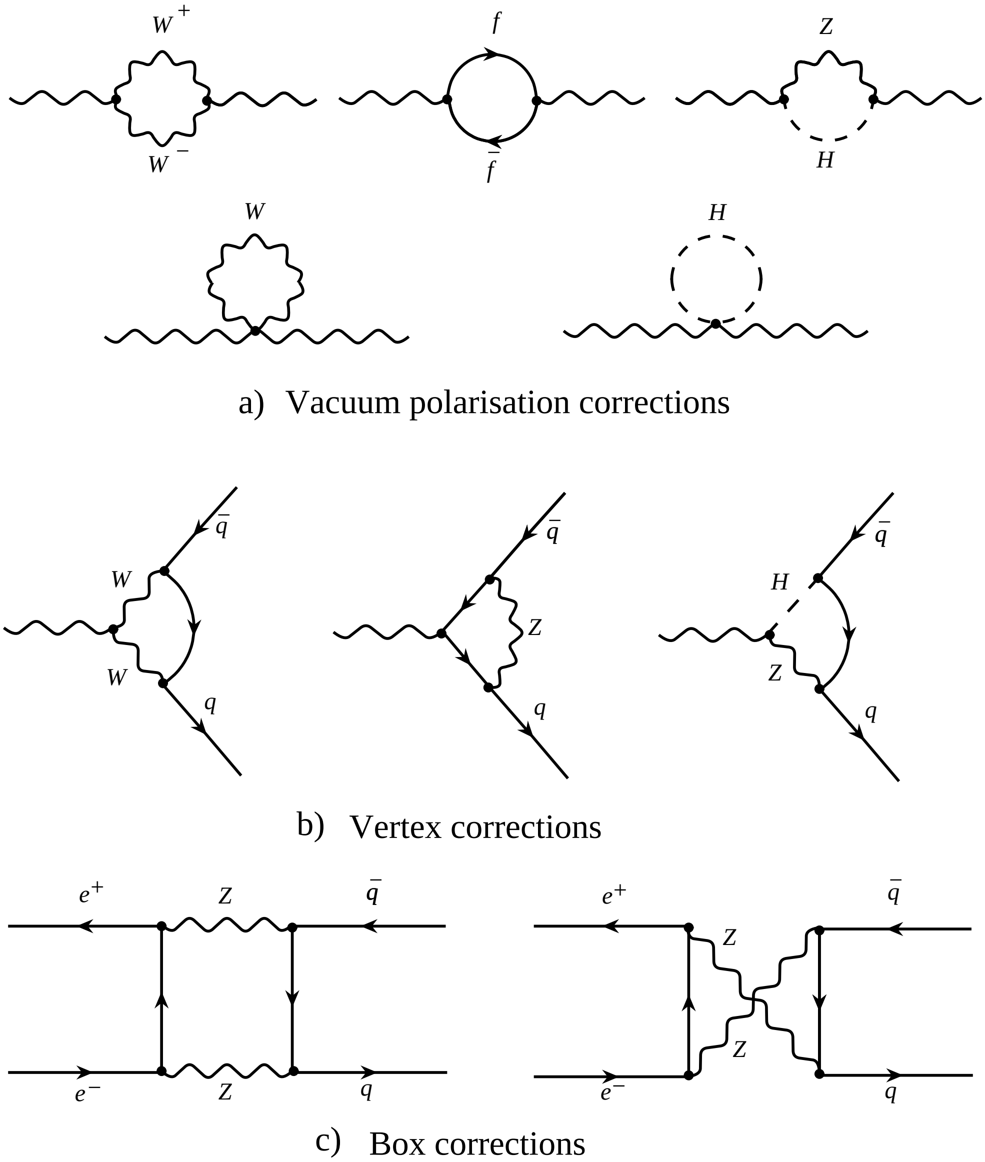

Figure 2.2: Examples of vacuum polarisation, vertex and box weak corrections to the process $\mathrm{e^+e^-} \to q\overline{q}$ at LEP2.

can be compared to the experimentally determined values, which may then be used to place limits on new physics.

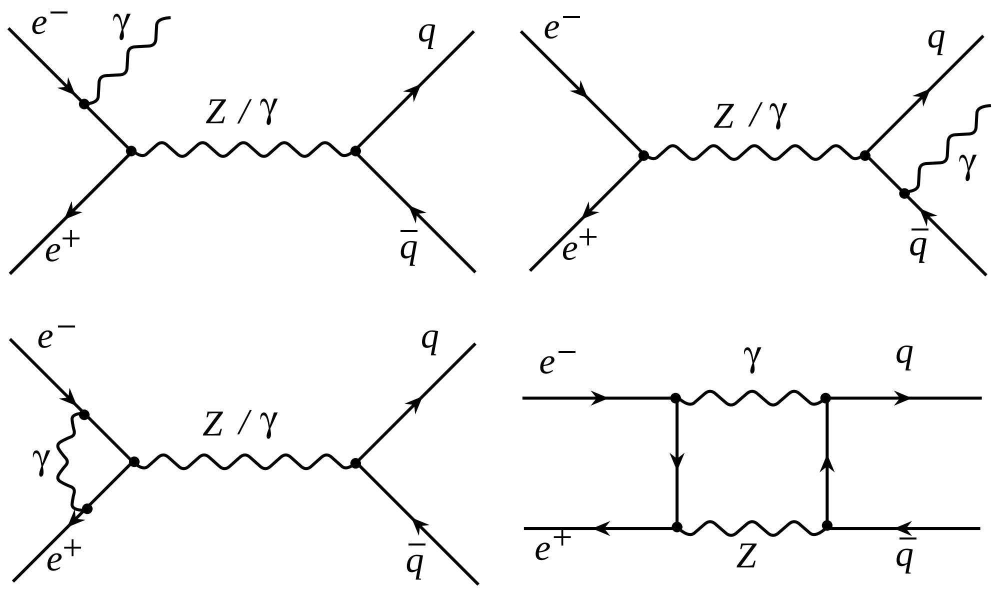

Figure 2.3: Examples of radiative corrections to the process $e^+e^- \to q\bar{q}$ at LEP2.

2.10 The Electroweak fit

Searches for new physics may essentially be divided into two classes. Direct searches look for the actual particles hypothesised by the various extensions to the Standard Model. However, in order for these searches to be successful there must be enough energy with which to produce the new particles. Indirect searches look for inconsistencies between the Standard Model predictions and their experimental measurements.

The Standard Model may be used to predict values for a variety of experimental observables. However, the theoretical predictions are subject to error because of the 18 input parameters listed in Section 2.7, values for which must be taken from experimental measurement. Nevertheless accurate tree level predictions may be calculated solely in terms of the three most precisely known parameters: the electromagnetic coupling constant, the weak coupling constant and the mass of the Z^0 boson.

Beyond tree level it is necessary to account for the masses of the Higgs boson and the fermions in order to include their contribution to higher order corrections. Due to the relatively weak force of the electroweak interaction, accurate higher order corrections may be calculated using perturbation theory. The majority of measurements at LEP have been precise enough to necessitate the inclusion of higher order corrections in the theoretical predictions. By making fits to experimental results, constraints can be placed on parameters in the theory such as the Higgs or top quark masses. In addition, the mutual consistency of observed results gives an indication of the validity of the predictions.

Any new physics would show up as a discrepancy between the experimental result and theoretical prediction. An experimental result which can not be accommodated by the electroweak fit might therefore be evidence of new physics. Such a discrepancy could be the result of a particle, too massive to be produced directly at LEP, being exchanged in additional higher order or tree-level processes. It is therefore possible to probe for new physics at energy scales much higher than the energy of LEP interactions.

The observables typically measured at LEP include the total and partial widths of the Z^0 gauge boson, the polarisation of the Z^0 decay products, left-right[21] fermion asymmetries, forward-backward[22] fermion asymmetries and fermion production cross-sections. In this thesis, a measurement of the cross-section ratio R_b is presented, which may also be included in the electroweak fit and thus used to probe for physics beyond the Standard Model.

[21] The left-right asymmetry is defined as the difference in the cross-section of initial left and right-handed electrons.

[22] The forward-backward asymmetry is defined as the difference in the angular distributions of outgoing fermions and anti-fermions.

2.11 R_b and limits on new physics

The branching ratio R_b is a cross-section ratio. Many of the higher order corrections (such as propagator corrections) are independent of the final state quark flavour and thus cancel out. However vertex corrections are flavour dependent. Due to its large mass, a heavy exchange particle involved in a higher order process will preferentially couple to the b quark, rather than the lighter quarks. By proposing heavy particles within a particular framework for new physics, such as those discussed in Section 2.8, new predictions for R_b may be calculated.

A significant disagreement between the Standard Model prediction and the measured value of R_b would be indicative of new physics. Hypothesising new exchange particles contributing to additional higher order corrections or tree-level processes can therefore provide an indication of the validity of particular new physics. However if the experimental result agrees with the Standard Model prediction then confidence limits may still be placed on the energy scale at which new physics might be realised.

The new physics that R_b has, to date, been used to place limits on are four-fermion contact interactions and supersymmetry. Contact interactions are expected to occur if fermions are composite and are mediated by some heavy particle being exchanged between the incoming and outgoing fermion pairs. Supersymmetry supposes a set of sparticles which could contribute to higher order corrections. Limits on physics beyond the Standard Model are usually parameterised by an energy scale Λ, which can be interpreted as the mass of a new particle, and a coupling strength g for the strength of the interaction. By varying the energy scale and coupling strength in the theory, a lower limit on the mass of a new particle can be obtained from a χ^2 fit of data to theory.

2.12 Summary

This Chapter has presented an outline of the Standard Model theory and its possible extensions. By making measurements of observables predicted by the Standard Model, limits on the energy scale of new physics may be derived. In this thesis a measurement of R_b is presented, which may therefore be used to further constrain the limits on new physics obtained from previous R_b measurements [20].

Chapter 3

Experimental Apparatus

3.1 Introduction

The ALEPH detector [21] was one of four general purpose particle detectors for the Large Electron Positron (LEP) collider [22] at the European Organisation for Particle Physics (CERN). Until the decommissioning of LEP in 2000 to make way for the construction of the Large Hadron Collider (LHC) [23], it was the world's largest particle accelerator. The main purpose of LEP was to study the electroweak sector of the Standard Model and the W and Z massive vector bosons.

This chapter presents an overview of the LEP accelerator system and the ALEPH detector. The online Data Acquisition (DAQ), event reconstruction, event simulation and offline computing environment for analysis are also discussed.

3.2 The LEP collider

The LEP machine was an e^+e^- storage ring, situated in a 26.67 km circumference tunnel at a depth of 70 to 150 m below the surface. The beam pipe was constructed from eight straight sections, linked together by eight curved sections, to form a nearly circular loop straddling the Swiss-French border near Geneva. Due to geological reasons, the plane of the ring was at a slight tilt of 1.42 %. The large scale of LEP was necessary due to the effect of synchrotron radiation. A relativistic charged particle with energy E and mass m moving along an arc of radius R will radiate energy proportional to E^4/m^4R. A large radius was therefore necessary to help compensate for the small electron mass. For a 100 GeV electron at LEP synchrotron radiation resulted in an energy loss of $\sim$3 GeV per orbit, which is $\sim 10^{13}$ times the energy loss for a proton of the same energy.

Electron and positron bunches were accelerated in opposite directions around the beam pipe at a rate of $\sim$11 KHz, under a vacuum pressure of $\sim 10^{-9}$ Torr. The bunches crossed every 22 μs at eight interaction points (IPs), situated in the middle of the straight sections to reduce background from synchrotron radiation. At four of these interaction points were situated the LEP detectors ALEPH, OPAL [24], DELPHI [25] and L3 [26]. The bunches were accelerated along the straight sections by means of radio frequency superconducting cavities at potentials of up to 2,300 MV, and guided around the curved sections by a total of 3,400 dipole bending magnets. A further 1,900 quadrupole, sextupole and corrector magnets ensured the beam was contained within the beam pipe, which was elliptical in cross-section and constructed from aluminium to prevent field distortions. The pipe narrowed at the interaction points where the beam was focused by superconducting quadrupoles to ensure a high luminosity (interaction rate). Figure 3.1 shows a schematic view of the LEP system.

LEP itself was the final stage of a series of particle production and accelerating machinery. Electrons were initially produced by a pulsed electron gun and accelerated to an energy of 200 MeV by a linear accelerator (LINAC). Positrons were then produced by colliding some of these electrons with a fixed tungsten target, after which the LINAC accelerated both the electrons and positrons to 600 MeV. The particles were then injected into the Electron Positron Accumulator (EPA) where they were separated into bunches. The bunches remained in the EPA until sufficient quantities were present for normal luminosity, after which they were injected into the Proton Synchrotron (PS) and then into the Super Proton Synchrotron (SPS) at which energies of 20 GeV were achieved. Finally the particles were injected into the main LEP ring where they were accelerated to normal physics energies. The bunches then remained stored in the ring, with a typical beam lifetime of up to

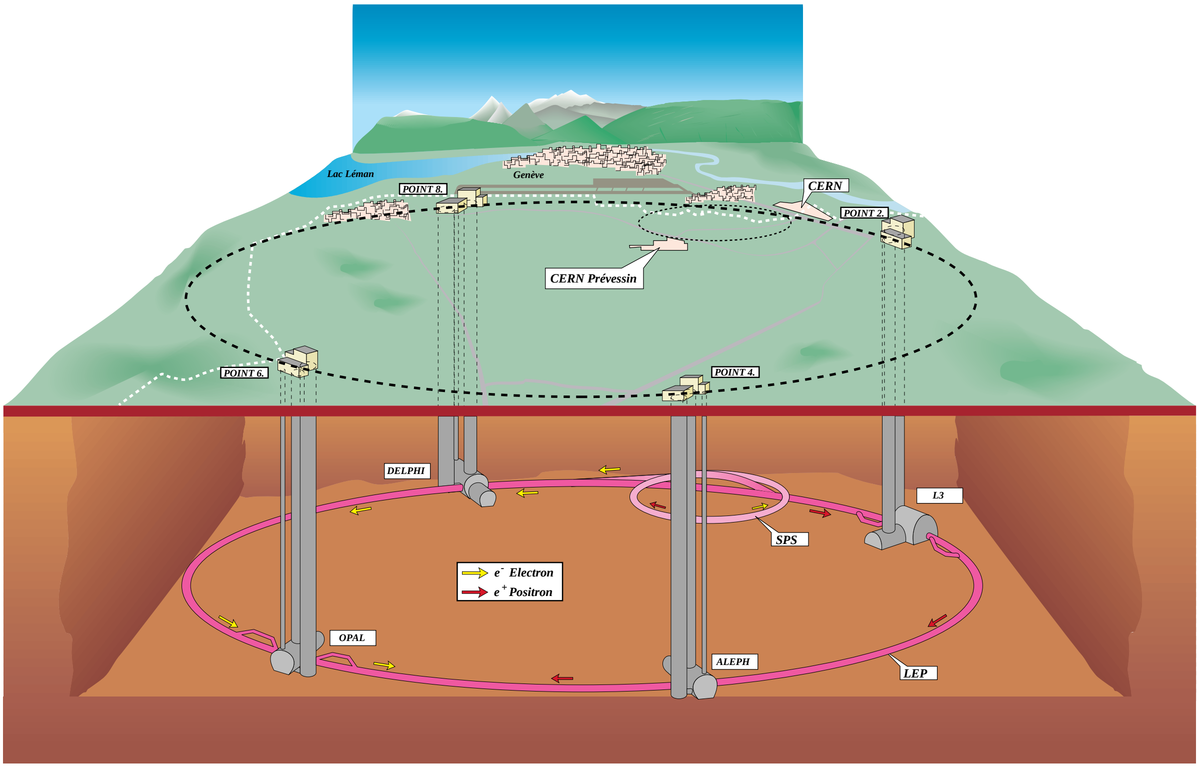

Figure 3.1: An overview of the LEP accelerator.

several hours. A schematic of the LEP injection system is shown in Figure 3.2.

During the LEP1 period from 1989 to 1995, the collider was run at centre of mass energies around 91.2 GeV, corresponding to the Z boson production peak. Over four million Z decays were recorded by ALEPH, which allowed rigorous examination of the Standard Model. The LEP2 period from 1996 saw the collider run at energies beyond the Z peak up to a centre of mass energy of 209 GeV in 2000, the last year of operation. Much of the LEP2 phase was concerned with W-pair production physics and the search for the Standard Model Higgs Boson. Typical LEP2 luminosities were $\sim 10^{32}$ cm^{-2}s^{-1}, resulting in a total integrated luminosity $\mathcal{L}$ for all LEP2 data taken by ALEPH of 719.8 pb^{-1}. For detector and physics calibration purposes, approximately one week of data was also taken each year at the Z peak prior to running at normal LEP2 energies. The data used in this analysis is shown in Table 3.1.

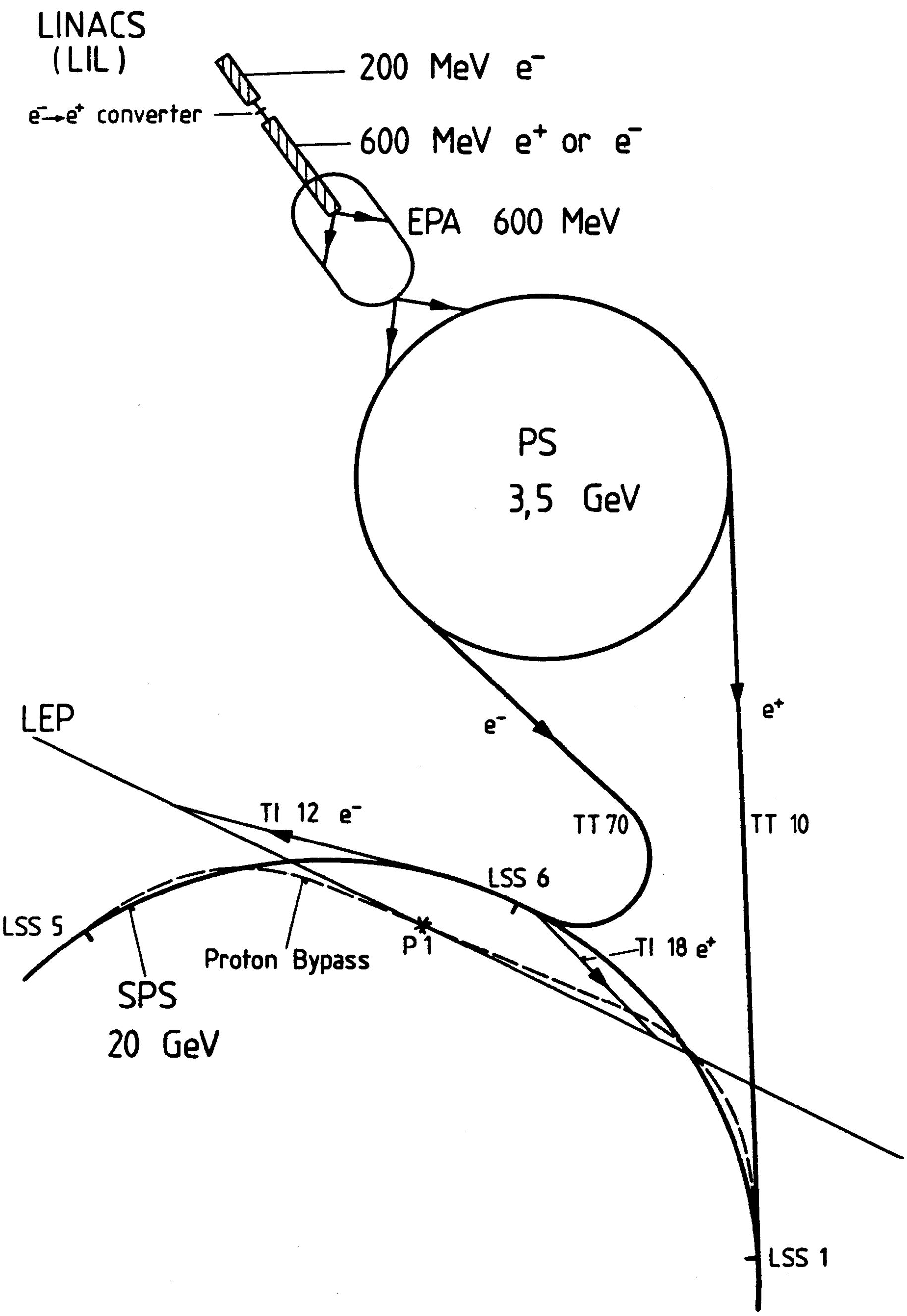

Figure 3.2: The LEP injection system.

Year	Mean Energy (GeV)	Data delivered by LEP (pb^{-1})	Data recorded by ALEPH (pb^{-1})	Data used in this analysis (pb^{-1})
2000	206.5	142.3	136.7	133.7
	204.9	84.2	81.7	81.6
	91.2	4.5	4.2	3.8
1999	201.6	44.0	42.1	41.9
	199.5	91.1	87.8	86.3
	195.5	88.1	82.6	79.9
	191.6	30.7	29.0	28.9
	91.2	4.2	3.9	3.5
1998	188.6	192.7	177.2	174.2
	91.2	3.3	3.1	3.0

Table 3.1: ALEPH integrated luminosities by energy.

3.3 The ALEPH detector

The ALEPH (Apparatus for LEP Physics) detector was situated at Point 4 on the LEP ring near the village of Echenevex in France. The Point 4 cavern was 143 m below ground and contained the whole ALEPH detector, centred around the interaction point. ALEPH had a length of ~12 m, a similar diameter, an overall mass of approximately 4,000 tonnes and 700,000 readout channels.

ALEPH was designed to be a general purpose detector, capable of studying all areas of physics accessible with LEP energies without restricting searches for new physics. It therefore covered as much of 4π solid angle as possible and consisted of a series of specialised subdetectors arranged in an onion-like structure, as shown in Figure 3.3.

The inner 3 subdetectors were the charged particle tracking components consisting of a Silicon Vertex Detector (VDET), the Inner Tracking Chamber (ITC), and the Time Projection Chamber (TPC). These were encased in a 1.5 Tesla superconducting solenoid magnet to allow momentum measurements of charged particles based on the curvature of their trajectories. Energy measurements were provided by a highly granular Electromagnetic Calorimeter (ECAL) and an iron Hadronic

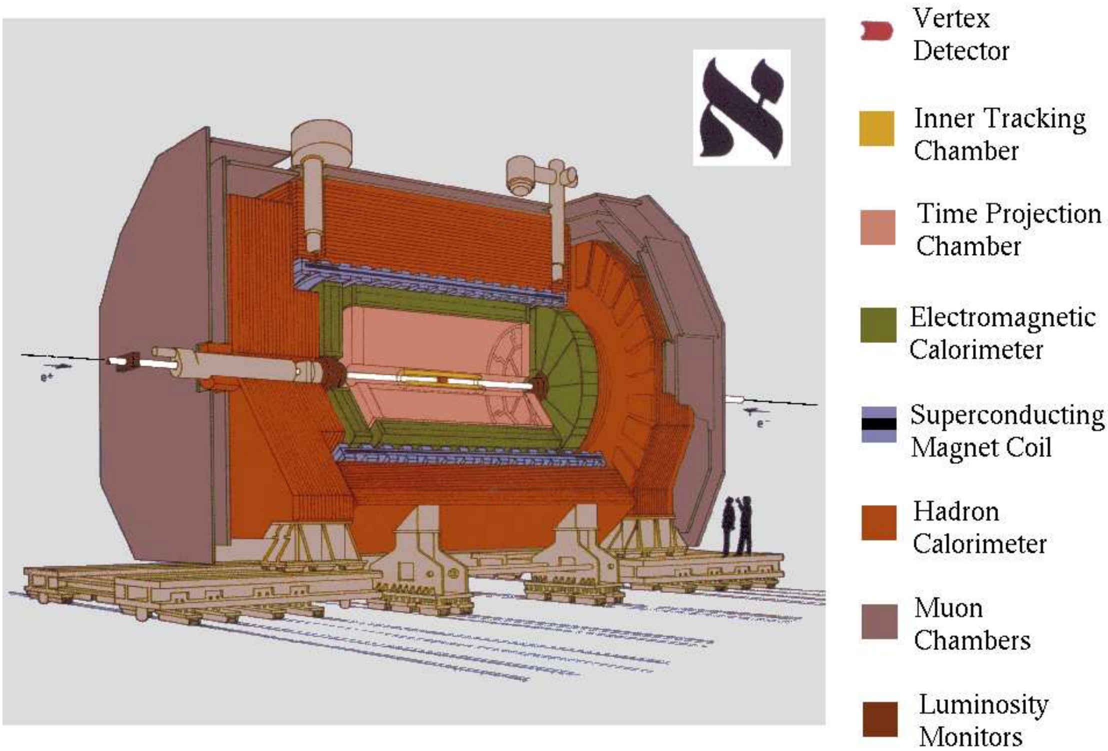

Figure 3.3: The ALEPH detector.

Calorimeter (HCAL), which doubled as a return yolk for the magnet. Finally, the outer layer was concerned with muon detection. With the exception of neutrinos, muons were usually the only particles to penetrate this far through the detector. Neutrinos being very weakly interacting would normally completely escape the whole detector.

Luminosity measurements were provided by an additional 3 subdetectors (SICAL, LCAL and BCAL) located close to the beam pipe. A complete description of the ALEPH detector may be found in [21, 27] and its performance is detailed in [28].

3.3.1 The ALEPH coordinate system

The ALEPH z-axis points along the e^- beam direction and due to the slight tilt of LEP makes an angle of 3.59 mrad with respect to the horizontal. The x-axis is horizontal and points towards the centre of LEP. The y-axis is orthogonal to the z-x plane and therefore points upwards at an angle of 3.59 mrad with respect to the vertical. The coordinate system is illustrated in Figure 3.4. When discussing track or jet directions within ALEPH cylindrical coordinates are mainly used, which are defined as follows:

$$\begin{aligned} x &= r\cos\phi \\ y &= r\sin\phi \\ z &= z \end{aligned} \tag{3.1}$$

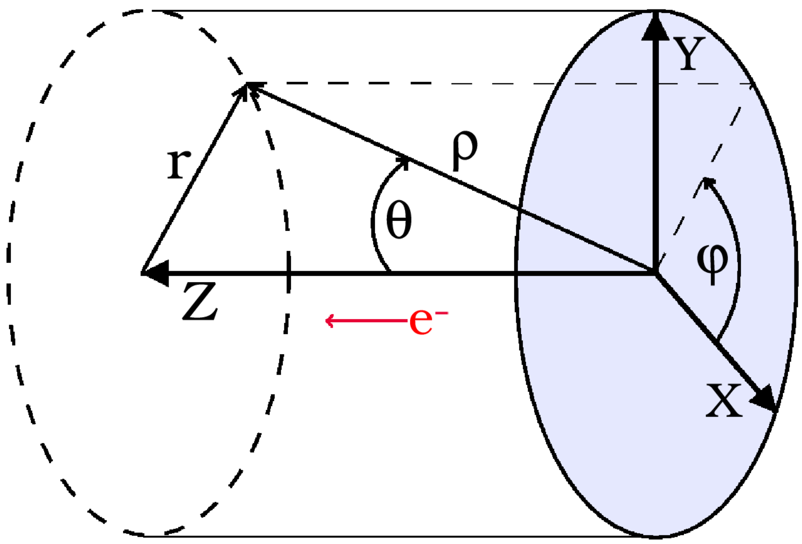

Figure 3.4: The ALEPH coordinate system.

3.3.2 The Silicon Vertex Detector

The VDET [29] was a silicon microstrip device designed to allow the high resolution reconstruction of particle trajectories close to the interaction point. It therefore played a crucial role in the identification of b and c quark hadrons which, due to their long lifetimes, may be tagged by the displaced secondary vertices of their decay products. The VDET was upgraded for LEP2 to increase angular coverage and to improve radiation tolerance. This was primarily to aid the search for the Higgs Boson, which is predicted to predominantly decay to b quarks if produced at LEP2.

The VDET extended radially from 6 to 11 cm, constrained by the beam pipe and the ITC. It consisted of two coaxial layers of double sided silicon wafers, with microstrips parallel and perpendicular to the beam direction for tracking in both the r-ϕ and z directions respectively. An angular coverage of 95 % was achieved for tracks required to have one VDET hit, and spatial resolutions of 10 to 16 μm were achieved for tracks with normal incidence to the detector. An illustration of the VDET is shown in Figure 3.5.

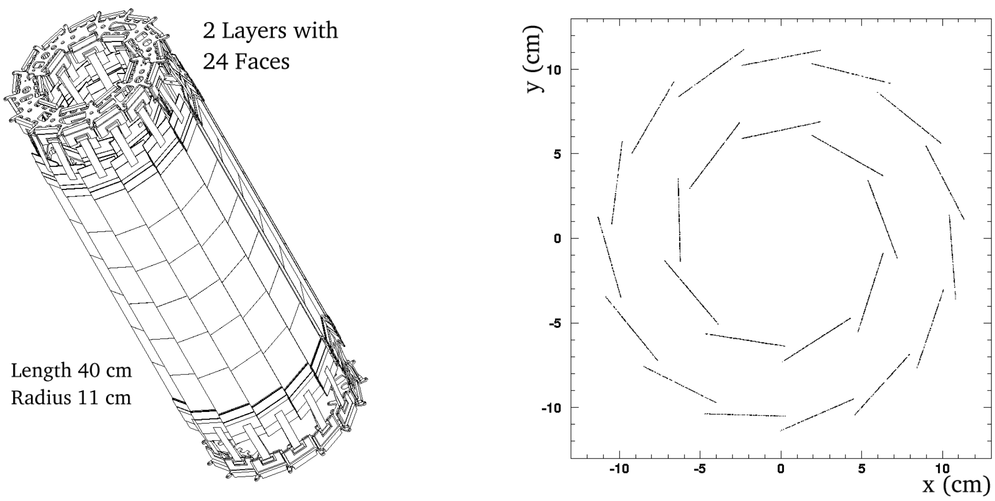

Figure 3.5: a) Full view of VDET and b) End view showing position of the faces.

3.3.3 The Inner Tracking Chamber

Surrounding the VDET was the ITC [30], a cylindrical drift chamber 2 m long extending radially out to 29 cm. It consisted of eight concentric layers of drift cells, 960 in total, providing up to eight hit coordinates per track. The hexagonal drift cells were defined by six field wires held at ground potential, through the middle of which was strung an anode sense wire (Figure 3.6). A resolution in the r-ϕ direction of 100 to 150 μm was achieved for each drift cell by measuring the time taken for ionising electrons produced by the charged track to drift to the sense wires. A z coordinate was also provided by measuring the time difference in the arrival of signals at each end of the sense wires. However the z resolution was low, of the order of a few centimeters, so the ITC z coordinate was therefore not used in track reconstruction.

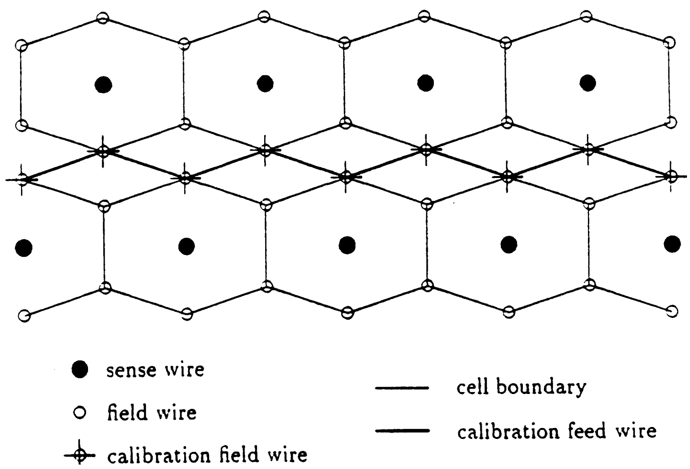

Figure 3.6: The ITC drift cell structure.

The ITC also supplied the only tracking information used in the first level trigger. As the ITC readout time was fast, 2 dimensional r-ϕ tracking information was available to the trigger system within 1 μs of a bunch crossing, and 3 dimensional information available within 2 μs.

3.3.4 The Time Projection Chamber

The TPC [31] was the main tracking chamber providing up to 21 three-dimensional hit coordinates per track. It was cylindrical, extending out to 1.8 m radially and consisted of a central high-voltage membrane perpendicular to the beam direction with grounded end-plates. A schematic of the TPC is shown in Figure 3.7.

Ionisation electrons produced by the passage of a charged track through the detector drifted towards the end plates where their positions and arrival times were detected by 18 multi-wire chambers. Each chamber consisted of cathode pads on which a signal was induced by anode sense wires. The pads were arranged in 21 concentric circles and each measured 6.2 x 30 mm in the ϕ and r directions respectively. The z coordinate was obtained from the measured drift time in conjunction with the known drift velocity. The resulting spatial resolutions were 180 μm in the

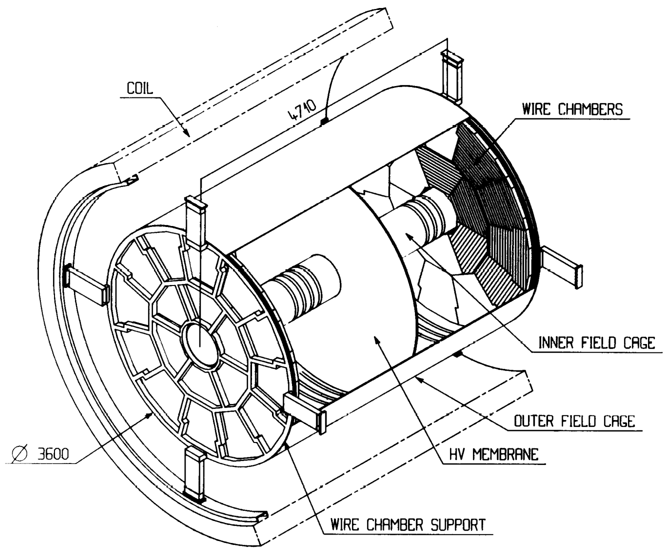

Figure 3.7: The Time Projection Chamber.

r-ϕ direction and 1 mm in the z direction.

Due to the presence of the 1.5 Tesla magnetic field, charged particles followed a helical trajectory through the TPC. This path projected on to the end-plates formed an arc from which the track transverse momentum could be derived. Using TPC information only, the resulting total momentum resolution measured for 45 GeV muons was

$$\frac{\Delta p}{p} = 1.2 \times 10^{-3} \ \ (\mathrm{GeV/c})^{-1} \tag{3.2}$$

The magnitude of the sense wire signals was proportional to the energy lost by ionisation. This energy loss dE/dx is dependent on the velocity, which in conjunction with the momentum measurement allowed the particle mass to be derived. The TPC therefore also acted as a particle identification system. Figure 3.8 shows the measured dE/dx for 40,000 tracks in hadronic Z^0 decays and the resulting separation between different particle types

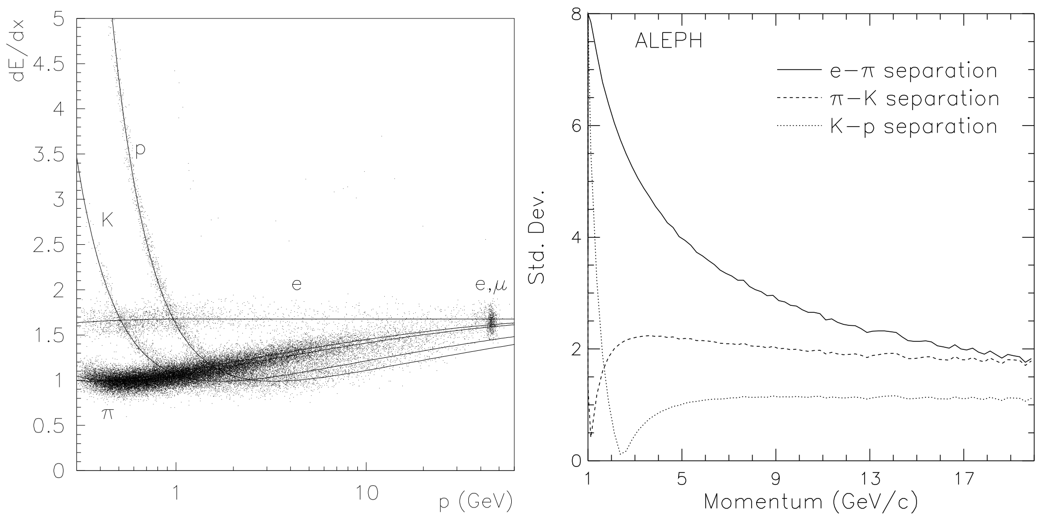

Figure 3.8: The measured dE/dx for 40,000 tracks in hadronic Z^0 decays (left) and the resulting particle identification separations (right). Taken from Reference [28].

3.3.5 The Electromagnetic Calorimeter

The purpose of the ECAL was to measure energy deposits from both charged and neutral particles. The 4.8 m long barrel and end-caps consisted of 45 layers of interleaved lead sheets and wire chambers, corresponding to 22 radiation lengths X_0. A lead-wire layer is illustrated in Figure 3.9.

Particles penetrating a lead layer produced a shower of electron-positron pairs, causing the anode wires to induce a signal in the cathode pads. The cathode pads were read out in groups, called towers, shaped so that they projected back to the nominal interaction point. Each of the 74,000 towers had an angular size of 0.9° x 0.9° providing a high spatial separation between showers for particle identification. Additionally the towers were segmented into three storeys or stacks, corresponding to $4X_0$, $9X_0$ and $9X_0$. This allowed the shower profiles to be studied, further aiding particle identification. The energy resolution of ECAL was measured as

$$\frac{\Delta E}{E} = \frac{0.18}{\sqrt{E}} + 0.009 \tag{3.3}$$

with an angular resolution of

$$\Delta_{\theta,\phi} = \frac{2.5}{\sqrt{E}} + 0.25 \text{ mrad} \tag{3.4}$$

where E is in GeV.

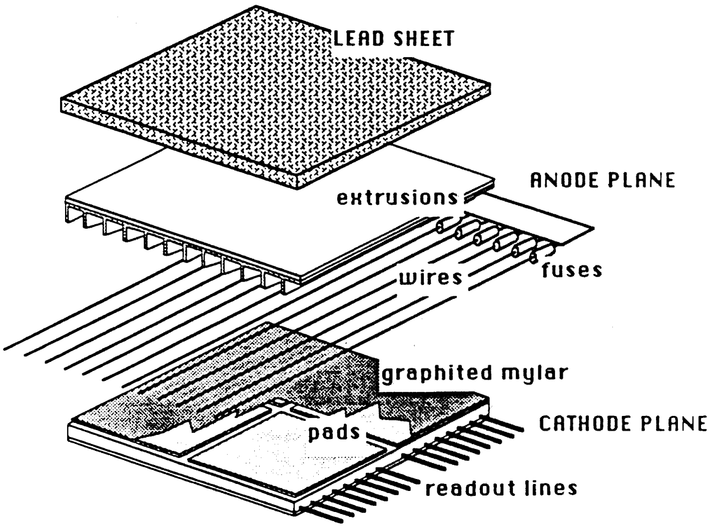

Figure 3.9: Detail of an ECAL layer.

3.3.6 The Hadron Calorimeter and Muon Chambers

The HCAL measured the energy deposited by hadrons and the trajectories of muons. It extended radially out to 5 m and consisted of 23 iron layers separated by plastic streamer tubes. The streamer tubes were coated in graphite and contained eight wire counter cells of size 9 x 9 mm. Showering in the iron layers caused the anode wires to induce a signal on cathode pads in the cells which, like the ECAL, were read out in towers projected back to the interaction point. The energy resolution measured with pions at normal incidence was

$$\frac{\Delta E}{E} = \frac{0.84}{\sqrt{E}} \tag{3.5}$$

with E in GeV. Additionally, the HCAL also acted as the return yolk for the magnet and provided mechanical support for the whole of ALEPH.

The muon chambers consisted of a further two layers of streamer tubes outside of the HCAL. Muons left a characteristic signal in both Calorimeters, a single trail of hits with no showering. The two streamer tube layers were separated by 50 cm and allowed muon exit angles from the detector to be measured with a resolution of 10 - 15 mrad.

3.3.7 The Luminosity Monitors

The instantaneous luminosity is defined as the ratio of the rate of $e^+e^- \to e^+e^-$ events (Bhabha scattering) to the precisely known theoretical cross-section for this process. The integrated luminosity refers to the ratio of the total number of these events to the cross-section over a period of time. In this analysis, the integrated luminosity is used for estimating background contributions.

The Bhabha scattering process is highly dependent on the polar angle with a cross-section $\sigma \sim \frac{1}{\theta^4}$. As the cross-section is therefore strongly peaked close to the beam pipe, this was where the three pairs of ALEPH luminosity monitors were placed. The Luminosity Calorimeter (LCAL) was the main luminosity monitor extending radially from 10 to 52 cm at $\pm$2.62 m from the interaction point, resulting in a sensitivity down to $\sim$2.6° from the beam direction. The LCAL was a lead-wire calorimeter of similar construction to the ECAL and Bhabha events were counted according to characteristic back-to-back energy deposits. The Solid State Luminosity Calorimeter (SICAL) was positioned at $\pm$2.5 m from the IP, extended coverage down to $\sim$1.4° and consisted of 12 tungsten sheets inter-spaced with silicon detectors. Together the LCAL and SICAL were used to provide integrated luminosity measurements. However, the event rate for these two monitors was not sufficient to provide instantaneous luminosity measurements. The Bhabha calorimeter (BCAL) was situated $\pm$7.7 m from the interaction point and consisted of alternating layers of tungsten and plastic scintillator, and allowed coverage from $\sim$0.3° to $\sim$0.5°. In this position the event rate was high enough for the BCAL to provide instantaneous luminosity measurements. However the position of the BCAL was close to LEP quadrupole focusing magnets making it unsuitable for integrated measurements.

3.4 The Trigger system and Data Acquisition

With bunch crossings every 22 μs it was not possible to readout every event. Attempting to do so would have resulted in considerable dead time (the time lost to new events whilst reading out an earlier event) in the detector and posed serious data storage problems. Additionally, many events were not the result of e^+e^- interactions but beam interactions with gas in the beam pipe or with collimators close to the interaction point. The ALEPH solution to filtering out these background events and minimising dead time was a 3 stage trigger system.

The Level 1 trigger was the first and fastest stage. The decision time was 5 μs, which therefore did not introduce any dead time into the system. This stage made a *yes* or *no* decision based on hit patterns in the ITC and energy deposition in the Calorimeters. If the event passed the Level 1 trigger, the Level 2 trigger was then initiated, which used information from the TPC. The Level 2 decision took $\sim$50 μs and reduced the event rate to $\sim$10 Hz. If the event passed the Level 2 decision, the full data acquisition (DAQ) process was initiated and the event checked with the Level 3 trigger. Unlike the hardware based Level 1 and 2 triggers, this stage was software based and used all the raw digitised data in the event. This final trigger reduced the event rate to a manageable 1 Hz. The number of background events (i.e not the result of an e^+e^- interaction) passing the trigger was negligible, with $\sim$5 % of e^+e^- events lost to dead time and trigger inefficiencies.

Each subdetector took data independently and the DAQ system was responsible for synchronising these data and building the full event. The Main Trigger Supervisor (MTS) synchronised the readout electronics of each subdetector with the appropriate bunch crossing. If the Level 2 trigger was passed, the MTS then initiated readout from the subdetector front end electronics. These data were then passed to the subdetector Event Builder (EB), and then onto the Main Event Builder (MEB) where the data from all the subdetectors were combined. The event was then passed to the online Main Host computer, where the event was checked by the Level 3 trigger. Events were then stored on a local disk for the duration of the run[1]. After the run, all the recorded events were reconstructed and then written to tape for permanent storage.

[1] A run was defined by either the lifetime of the beam or a maximum 600 MB of data.

3.5 Event reconstruction

Immediately after a run had been completed, the events were fully reconstructed using the Facility for ALEPH Computing and Networking (`FALCON`). This was a dedicated computing resource running the `JULIA` [32] (Job to Understand LEP Interactions at ALEPH) software package, which reconstructed all the raw data in the event into meaningful parameters useful to physics analysis.

3.5.1 Track reconstruction

Track reconstruction began with the TPC data where radially neighbouring hits were joined together to form track segments. Track segments were then connected together according to a helix hypothesis. The TPC track was then extrapolated into the ITC and VDET where hits consistent with the extrapolated track were added to form the final complete track. The final track fit was based on the Kalman filter [33], which takes into account hit coordinate errors, scattering and energy loss as particles pass through the detector. Studies using simulated data (Monte Carlo) indicated that tracks with at least 4 hits in the TPC were reconstructed with a 98.6 % efficiency. The small inefficiency was due largely to track overlaps and cracks in the detector, and was reproduced in the Monte Carlo to better than 0.1 %. With all the information from the VDET, ITC and TPC, the overall track momentum resolution was measured as

$$\frac{\Delta p}{p} = 0.6 \times 10^{-3} \ \ (\mathrm{GeV/c})^{-1} \tag{3.6}$$

for 45 GeV muons.

3.5.2 Energy Flow

The purpose of the Energy Flow algorithm was to reconstruct charged and neutral particles in an event, known as "energy flow" objects. Additionally, the overall event energy resolution was improved by combining all available tracking and calorimetry information. This algorithm only used tracks which had at least 4 TPC hits, and originated from within a cylinder 20 cm long and of 2 cm radius, centred on the interaction point. This rejected tracks from secondary decays or interactions, such as the V^0 vertex $\gamma \rightarrow e^+e^-$, with an absence of hits in the ITC providing a secondary vertex cross-check.

A cleaning procedure was first applied to identify fake energy deposits in the calorimeters from noisy channels. Charged tracks were then extrapolated into the calorimeters and associated with energy deposits to form charged calorimeter objects. Electrons, muons, pions, kaons and protons were identified from TPC dE/dx measurements, the ECAL shower shape and energy deposits in the HCAL. Any unidentified charged objects were treated as pions. The energy of these charged objects was then calculated from their mass and momenta, which was subtracted from the calorimeter energy deposits. The remaining energy was then assumed to be from neutral particles, with the shower shapes being used to identify photons and neutral pions, and everything else being taken to be neutral hadrons. Any neutrino energy was inferred from missing energy in the event.

The energy flow algorithm resulted in an object energy resolution parameterised as

$$\frac{\Delta E}{E} = \left[\frac{0.6}{\sqrt{E}} + \frac{0.6}{E}\right]\left(1 + \cos^2\theta\right) \tag{3.7}$$

where E is in GeV and θ is the object polar angle, with an overall event energy resolution of $\sim$7 %. A complete list of all the reconstructed energy flow objects was made available for subsequent physics analysis.

3.6 Event simulation

Critical to many particle physics analyses is the use of simulated data, which is known as Monte Carlo. Monte Carlo events are used to estimate a variety of parameters in data, such as background components, detector acceptances and selection efficiencies, as well as allowing for checks and optimisations to be made at all stages of an analysis. As Monte Carlo therefore often plays a central role in an analysis, it is crucial that the simulated events reproduce the real data to a high degree of accuracy.

The simulation of events for ALEPH was a three stage process. First an event generator simulated e^+e^- interactions according to Standard Model production and decay processes. The second stage then modelled the interaction of the resulting particles with the detector. Finally, the event was reconstructed in exactly the same way as real data events. The only difference between Monte Carlo and data events was that the Monte Carlo contained all the "truth" information regarding the underlying physics processes.

3.6.1 Event generators

Event generation is typically performed in two stages. First, the e^+e^- interaction and production of the final state partons or bosons is simulated. This stage can be modelled very accurately using electroweak theory and includes any initial or final state radiation effects. The second stage is then concerned with the hadronisation of the event. Parton showering is modelled relatively accurately using perturbative QCD calculations. However, the fragmentation of coloured partons into colour singlet hadrons is a non-perturbative process and so cannot be calculated. A phenomenological approach is therefore used, with all the Monte Carlos discussed here simulating fragmentation according to the Lund model [34]. The output of the hadronisation program is a set of long lived particles which may be seen in the detector. Any particle decays (secondary vertices) are generally not modelled by the event generators, but by the detector interaction stage. The Monte Carlo samples used for this analysis were as follows:

- `KK2F` was used for $e^+e^- \rightarrow q\overline{q}$ events. This Monte Carlo used the `KK` [35] generator for simulating di-quark production, which was interfaced with the new `PYTHIA` [2] [36] program to perform the hadronisation. `KK2F` offers several improvements over the `KORALZ` [37] Monte Carlo used for earlier measurements, the most important being the inclusion of initial-final state QED interference.

- `KRLW03` was used for $e^+e^- \rightarrow W^+W^-$ events. This Monte Carlo used the `KORALW` [38] generator to simulate both the W^+W^- production and event

[2] The new `PYTHIA` program (version 6.1) is a merged version of the `PYTHIA` v 5.7 [34] generator and the hadronisation program `JETSET` v 7.4. [34]

hadronisation for the three charged current (CC03) production processes. Feynman diagrams for the CC03 processes are shown in Figure 3.10.

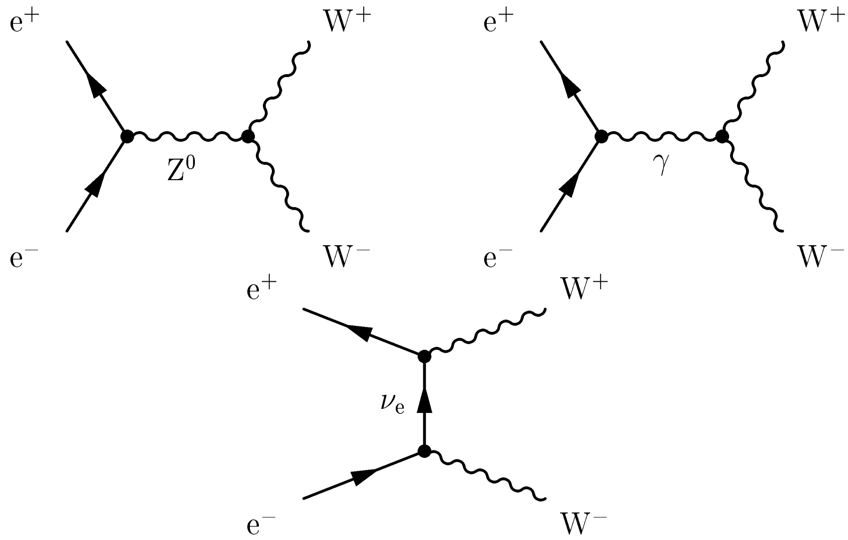

Figure 3.10: The CC03 diagrams of WW production. The top two diagrams are the annihilation diagrams while the third is the exchange diagram.

- PYTH05 was used for $\mathrm{e}^+\mathrm{e}^- \to Z^0Z^0$ events. This Monte Carlo used the PYTHIA generator to simulate both the Z^0Z^0 production and event hadronisation.

- HVFL05 was used for calibration studies at the Z^0 peak. This Monte Carlo used the DYMU2 [39] generator to simulate $\mathrm{e}^+\mathrm{e}^- \to q\overline{q}$ interactions and PYTHIA to model the event hadronisation.

Separate Monte Carlo samples were used for each energy point, with the sample sizes for each energy listed in Table 3.2. The Monte Carlo samples used for Z^0 calibration studies are shown in Table 3.3.

3.6.2 Detector interaction and event reconstruction

The interaction of a Monte Carlo event with the detector was performed using the ALEPH program GALEPH [40]. This used GEANT3 [41] to simulate the interaction of the particles with the matter of the detector, and then modelled the response of the detector to those interactions. The output was raw hit information which was then reconstructed in exactly the same way as real data events using the JULIA program,

Energy	Number of events (x 10^3)		
	KRLW03	PYTH05	KK2F
189 GeV	500	200	2,000
192 GeV	100	200	2,000
196 GeV	100	200	2,000
200 GeV	300	200	2,000
202 GeV	100	200	2,000
205 GeV	100	200	2,000
207 GeV	500	200	2,000

Table 3.2: The Monte Carlo sample sizes used for each energy

Year	Number of HVFL05 events (x 10^3)
1998	150
1999	500
2000	150

Table 3.3: HVFL05 sample sizes by year.

as discussed in Section 3.5. The resulting Monte Carlo events were then written to tape for use in physics analyses. In order to minimise statistical uncertainties in the Monte Carlo, the quantity of Monte Carlo used in an analysis is as large as possible. For the analysis presented in this thesis approximately 10^2 - 10^3 times the number of data events were used for Monte Carlo studies.

3.7 Offline analysis framework

The ALEPH Physics Analysis (ALPHA) [42] program was a software framework designed to facilitate the writing of analysis code in FORTRAN77. The analysis code for processing events was written within the ALPHA framework, which provided the following functionality:

- Interface to data and Monte Carlo events stored on tape.
- Simple access to reconstructed event variables, such as track momentum and vertices, as well as all the truth information for Monte Carlo events.
- A comprehensive set of utility subroutines commonly required for physics analyses, such as event shape and jet clustering algorithms.

- A histogramming package for outputting results.

`ALPHA` therefore provided an excellent environment for analysis at ALEPH, and was used extensively for the analysis presented in this thesis.

Chapter 4

Event selection and the evaluation of R_b

4.1 Introduction

This measurement of R_b was based on a two stage event selection process. First $e^+e^- \rightarrow q\overline{q}$ (hadronic) events were selected from all available data at a given LEP2 energy. The resulting event sample is referred to in this analysis as the event *preselection*. From this preselection the $e^+e^- \rightarrow b\overline{b}$ content was then identified, a process known as b-tagging. The resulting event sample is referred to as the event *selection*. The preselection and selection samples, in conjunction with backgrounds estimated from Monte Carlo, are then used to calculate a value for R_b.

This chapter presents a detailed description of the hadronic preselection and the b-tagging. The calculation of R_b from both event (single) and hemisphere (double) tagging, including the estimation of backgrounds from the Monte Carlo, is then discussed. First however jet clustering and primary vertex finding are described as they are important for both the event preselection and selection.

4.2 Jet clustering and Primary Vertex finding

The primary purpose of jet clustering is to reproduce the directions and energies of the final state partons in an event. The clustering procedure begins by considering each charged track and neutral energy deposit to be a *pseudo-jet*. These are then combined in pairs until a specified threshold is reached. This analysis used the JADE [43] clustering algorithm, which for a pair of pseudo-jets i and j defines the test variable y_{ij} as:

$$y_{ij} = \frac{2E_i E_j \left(1 - \cos\left(\theta_{\mathrm{ij}}\right)\right)}{E_{\mathrm{vis}}^2} \tag{4.1}$$

where E_i is the energy of pseudo-jet i, E_{vis} is the visible energy for the event, and θ_{ij} is the angle subtended between i and j, with the numerator being the invariant mass squared of the two objects. This test variable is then calculated for all possible pair combinations. If the lowest y_{ij} value does not exceed the specified threshold value y_{cut}, that pair is combined by summing their 4-momenta to create a new pseudo-jet. The process is then repeated, discarding the pairs used to create new pseudo-jets, until the lowest y_{ij} value exceeds y_{cut}. The remaining pseudo-jets are then declared as jets. The value of y_{cut} therefore determines the number of jets clustered, with a low value resulting in a high number of jets, and a high value a low number of jets. By not having a fixed y_{cut} value, it is also possible to cluster events into a specified number of jets.

For accuracy, the primary vertex is calculated separately for each event. The ALEPH primary vertex finder uses both jets and individual track information, in conjunction with the beam spot from LEP. A detailed description of the method may be found in [44].

4.3 Data Quality

The performance of the ALEPH detector and subdetectors was not uniform for all data taking, and as a result not all the data recorded by ALEPH during 1998 - 2000 is used in this analysis. The data taken in each run were assigned quality flags defined as follows:

- `LX` - Integrated and instantaneous luminosity measurement.
- `TR` - Tracking resolution, momentum and charge measurement.
- `EF` - Energy measurement.

- `DX` - Particle identification.

The value of these flags was determined manually for each run depending on the performance of the associated subdetectors. If there were no observed faults in the hardware or data acquisition, the flags were assigned a "`PERFECT`" value. If however there was a problem during a run that might have had an effect on physics analyses, the appropriate flags were set to "`MAYBE`". Occasionally a major problem in a run would result in bad or unreliable data, for which the flags were set to "`DUCK`". The use of data in runs with `MAYBE` flags depended on what the problems were during that run and whether it would have an effect on a particular analysis. The majority of runs were assigned `PERFECT` flags.

For consistency with the rest of the ALEPH collaboration, so that the data used in all analyses was the same, this analysis used data that conformed to the W^+W^- physics group data selection criteria [45]. This was simply defined as runs where all the flags were `MAYBE` or `PERFECT`, which resulted in the rejection of approximately 1 - 2 % of the available data as shown in Table 3.1.

4.4 Selection methodology

Events that you wish to select are known as *signal* events, whilst any non-signal events are known as *background* events. Events were therefore selected according to various predefined criteria designed to select signal events whilst suppressing background events. These criteria are known as selection *cuts*, each of which was defined as the value of some event parameter. Each selection cut was applied in turn, with events failing the cut removed from the sample.

As the value of a particular event parameter is usually distributed over some range for all events, the choice of value for a selection cut is necessarily a trade off between the efficiency of signal selection and the amount of background selected (purity). In order to retain a reasonable number of signal events and thus maximise statistics, it was therefore necessary to account for background passing the selection cuts. All background components in both the data preselection and data selection were estimated from the Monte Carlo. The calculation of the background contributions in the selected data samples is discussed in Section 4.6.5.

4.5 The hadronic preselection

The first stage in the measurement of R_b was obtaining the hadronic preselection. At the LEP2 energies from 189 - 207 GeV there are various non-hadronic backgrounds to suppress. This included $e^+e^- \to l\bar{l}$ (leptonic) events, where the leptons maybe electrons, muons or taus, and W-pair (W^+W^-) and Z-pair (Z^0Z^0) production events. An additional source of background at energies above the Z^0 peak is radiative events, where the interaction energy is at a lower energy than the centre of mass energy due to initial state radiation. Checks must also be made on the event quality to ensure that the event has been reconstructed accurately. The cuts made to suppress these background events are as follows:

- The first selection cut is to suppress radiative return events. The cross-section for the production of a real Z^0 as propagator in e^+e^- annihilation is large compared to the production of a virtual Z^0 or γ^* propagator at higher energies. Thus one or both of the interacting leptons may radiate a hard photon such that the interaction energy tends towards that of the Z^0 mass. According to Monte Carlo, these initial state radiation (ISR) events account for ~75 % of all hadronic events at 189 - 207 GeV. In order to suppress radiative events, this analysis uses an *exclusive* selection. This is defined as events which satisfy the cut $\sqrt{s'/s} > 0.9$, where s is the square of the centre of mass energy, and s' is the square of the mass of the Z^0/γ^* propagator. Events passing this cut are referred to as *non-radiative* events. When only one ISR photon is present, a good approximation to s' is [3]

$$s'_m = \frac{\sin\theta_1 + \sin\theta_2 - |\sin(\theta_1 + \theta_2)|}{\sin\theta_1 + \sin\theta_2 + |\sin(\theta_1 + \theta_2)|} \times s \tag{4.2}$$

  where θ_1 and θ_2 are the angles of the final state fermions measured with respect to the incoming e^-, or with respect to the direction of an ISR photon if seen in the detector. An ISR photon in the detector may be identified by the presence of a large amount of isolated electromagnetic energy. However, the ISR photon often passes undetected down the beam pipe. In order to determine the directions of the outgoing fermions, the event (minus any identified ISR photons) is clustered into two jets. The jet axes are then taken to approximate the directions of the final-state fermions.

- Events must fulfil the "`CLASS16`" criteria. This classification was originally developed to select hadronic events at LEP1, but is equally valid for energies beyond the Z^0 peak. Events must have at least seven good charged tracks, with the total energy of all charged tracks at least 10 % of the centre of mass energy. A good track is defined as having a minimum 4 hits in the TPC, a polar angle θ satisfying $|\cos\theta| < 0.95$, originating from within a cylinder of radius 2 cm and length 10 cm centred on the interaction point. These requirements will remove any leptonic events and events not the result of an e^+e^- interaction. The latter includes cosmic ray events and interactions with gas in the beam pipe or the beam pipe itself. Additionally, a hardware and DAQ error check is performed, as the total integrated data luminosity does not include any events where errors of this nature were flagged.

- As a further precaution against including any radiative events, the visible mass of the event must be at least 70 % of the centre of mass energy. The visible mass is defined as the invariant mass of all observed energy objects in the event which is given by:

$$M_{\text{vis}} = \left(E^2 - \mathbf{p}^2\right)^{\frac{1}{2}} \tag{4.3}$$

  where E and $\mathbf{p}$ are the total energy and total 3-momentum respectively for all observed energy objects in the event.

- An additional source of background in this analysis are W-pair and Z-pair production events. However these events may be efficiently suppressed by requiring the event thrust $T > 0.85$. The thrust is defined as the sum of the lengths of the longitudinal momenta of the energy objects in the event relative to the axis $\mathbf{n}$ which minimises this sum:

$$T = \frac{\sum_{i=1}^{N} |\mathbf{n}.\mathbf{p}_i|}{\sum_{i=1}^{N} |\mathbf{p}_i|} \tag{4.4}$$

where N is the number of energy flow objects and $\mathbf{p}_i$ is the momentum of energy flow object i. T will lie between 0.5 and 1., with $T \sim 0.5$ for an isotropic event and $T \sim 1.0$ for a dijet event. Thus W^+W^- and Z^0Z^0 events are expected to generally have lower thrust values than $q\overline{q}$ events.

From Monte Carlo, this cut of $T > 0.85$ rejects ~78 % of W^+W^- and Z^0Z^0 events, whilst rejecting only ~8 % of hadronic events. The thrust distributions for hadronic, W-pair and Z-pair events in Monte Carlo and for all data at 189 GeV are shown in Figure 4.1.

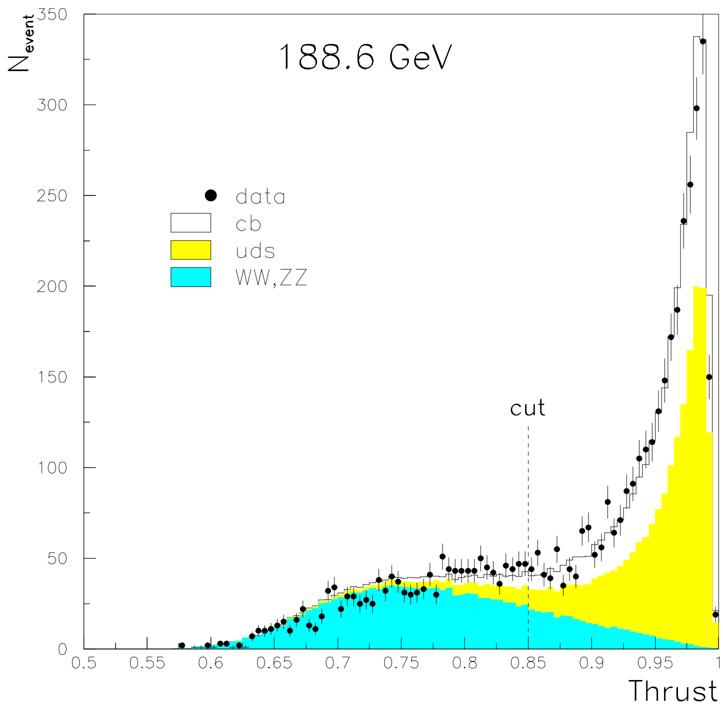

Figure 4.1: Thrust distributions for hadronic, W-pair and Z-pair events in Monte Carlo and for all data at 189 GeV, showing the selection cut used in this analysis.

- A final cut is made on the directions of the two jets clustered for estimating the final-state parton directions. In order to ensure that the event is adequately contained within the VDET acceptance, any events where the polar direction θ of one or both of the jets satisfies $|\cos\theta| > 0.9$ is discarded. This is important as this analysis relies heavily on the track resolution afforded by the VDET.

All remaining events after these cuts constitute the preselection. Monte Carlo indicates that the preselection samples obtained in this analysis are ~89 % non-radiative hadronic, ~3 % radiative hadronic, with the remaining events being W^+W^- and Z^0Z^0 background.

4.6 The b-tag

Having obtained the hadronic preselection, the $e^+e^- \rightarrow b\bar{b}$ content (B events) must then be identified. There are many ways of identifying B events, which fall into the following general categories:

- High lepton transverse momentum. This was the first b-tag used at LEP, based on identifying electrons or muons from the semi-leptonic decays of B hadrons [46]. However the branching ratio for the B hadron decay to leptons is low at ~20 %, resulting in a low selection efficiency and consequently a poor statistical resolution.

- Event shape variables. Due to the large b quark mass and hard fragmentation, $b\bar{b}$ events may be selected according to event shapes such as thrust or sphericity [47]. However the discriminating power of these tags is low such that they are usually only used in conjunction with other tags in neural networks. A heavy reliance on Monte Carlo also results in systematic effects which can be hard to quantify.

- The long lifetime of B hadrons. These tags are the most powerful discriminants and either rely on the dedicated reconstruction of secondary vertices, or simply on the impact parameters[1] of charged tracks. ALEPH is particularly suited to these tags as the VDET provides a very high tracking resolution close to the primary vertex. An additional advantage of lifetime tags is that in principle all $b\bar{b}$ events may be tagged, and hence the sample size maximised.

In order to maximise statistics and fully take advantage of the ALEPH tracking resolution, this analysis used a single tag based on the large impact parameters of

[1]The impact parameter is defined in Section 4.6.1.

tracks from secondary vertices [48]. A combined tag or neural network was not used as the increase in tagging performance is small and not justified with respect to the low data statistics available.

4.6.1 The signed impact parameter significance

If charged tracks in ALEPH were straight then the 3 dimensional impact parameter would simply be defined as the distance of closest approach between the the track and the primary vertex. However because of the magnetic field in ALEPH charged tracks are helical in nature, resulting in a more complex definition. Referring to Figure 4.2, the point S_2 refers to the distance of closest approach D between the track and the jet axis. A tangent to the helix at this point is then calculated, and the impact parameter δ taken to be the distance of closest approach between the tangent and the primary vertex.

This impact parameter may then be *signed* positive or negative, according to the orientation of the impact parameter with respect to the jet axis. For each jet, the event is divided into two hemispheres by a plane which passes through the interaction point perpendicular to the jet axis. An impact parameter which falls within the same hemisphere as the jet and is thus orientated in the same direction as the jet axis is signed positive. Impact parameters falling in the opposite hemisphere are signed negative. Tracks with positive impact parameters are said to pass *upstream* of the primary vertex, and those with negative impact parameters *downstream* of the primary vertex. If the jet axis accurately reproduces the direction of the original B hadron, then all tracks from a secondary (decay) vertex will pass upstream of the primary vertex, as the decay point of the B hadron must lie along its flight path. All tracks from secondary vertices will therefore be positively signed.

Impact parameters however suffer from a statistical uncertainty due to the errors in the track fitting and primary vertex reconstruction. This uncertainty is dependent on track momentum, track direction and the number of hits in the tracking system. In order that impact parameter information for all tracks in an event may be treated

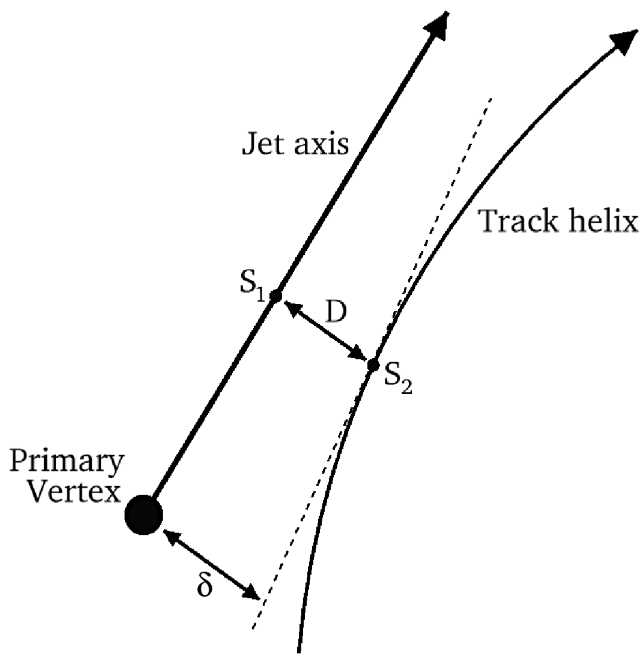

Figure 4.2: Graphical illustration of the impact parameter.

uniformly, the impact parameter significance is defined as

$$S = \frac{\delta}{\sigma_\delta} \tag{4.5}$$

where σ_δ is the statistical error on the impact parameter magnitude δ.

For events containing no secondary vertices, the errors introduced in the track and primary vertex reconstruction result in an equally distributed number of positive and negative impact parameter significances. As lifetime contributes only to the number of positive impact parameter significances, a fit $I\left(|S|\right)$ to the negative half of the distribution thus provides a measure of the impact parameter resolution of ALEPH. This function comprises a central Gaussian component and an exponential component to fit the tail of the distribution [48]. The effect of the presence of lifetime on the impact parameter distributions is shown in Figure 4.3.

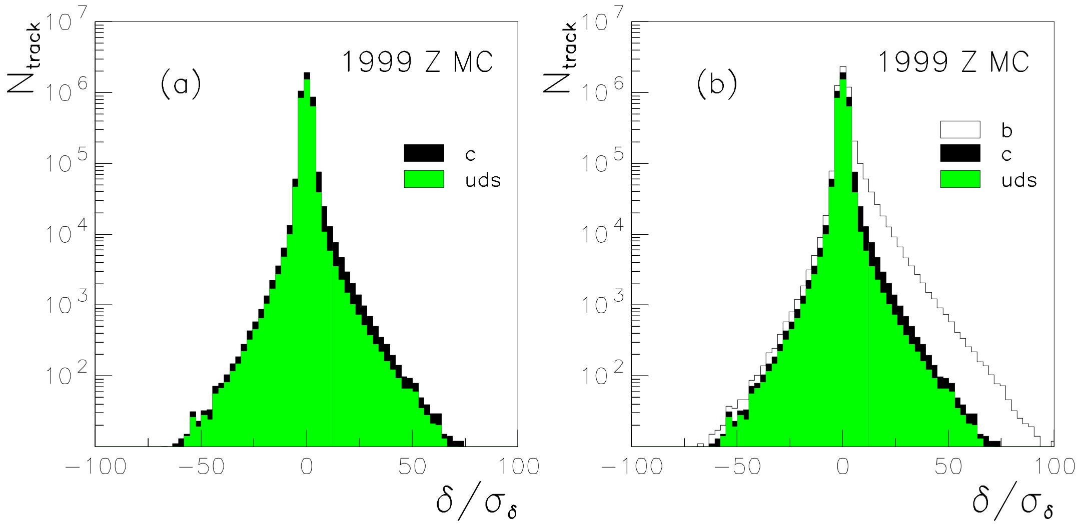

Figure 4.3: Impact parameter significance distributions for 1999 Z Monte Carlo. Plot b) includes tracks from b events, whilst plot a) does not.

4.6.2 The impact parameter b-tag

With the ALEPH impact parameter resolution function $I(|S|)$, the confidence level P_T that a track originated from the primary vertex is defined as [1]

$$P_T = \int_S^\infty 2I(|S|)dS \tag{4.6}$$

Hemispheres are defined by dividing an event into two halves by a plane perpendicular to the thrust axis passing through the primary vertex. A confidence level $P_{J,H,E}$ that a jet, hemisphere or event with N tracks has lifetime is then given by

$$P_{J,H,E} = \prod_{k=1}^{N} P_{T_k} \times \sum_{j=0}^{N-1} \left((-ln \prod_{k=1}^{N} P_{T_k})^j / j! \right) \tag{4.7}$$

where P_{T_k} is the confidence level for track k from the total N tracks. This results in a flat distribution for jets, hemispheres or events containing no long-lived particles, but as shown in Figure 4.4 is strongly peaked near zero for those containing lifetime. Defining the b-tag as the negative logarithm of this probability, jets, hemispheres or events containing lifetime may then be selected by cutting on some value of the b-tag. The choice of value to cut on (the selection cut) is discussed in Section 4.7. Jets, hemispheres or events remaining after the cut on the b-tag are referred to as having been *tagged* and constitute the jet, hemisphere or event selections. Figure 4.5 shows the number of events selected (tagged) as a function of the event tag for 1999 Z Monte Carlo. The corresponding B selection efficiencies and purities are shown in Figure 4.6.

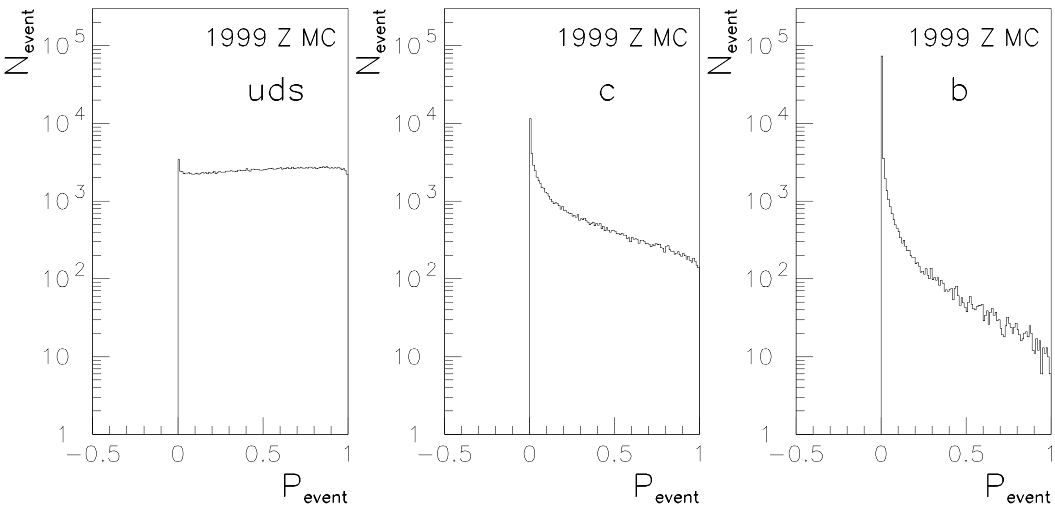

Figure 4.4: Event probability distributions for 1999 Z Monte Carlo. Note the presence of the high peak for event probabilities near zero for the beauty (b) quarks compared to the light (uds) and charm (c) quarks.

4.6.3 The b-tag algorithm

The calculation of jet, hemisphere and event probabilities was performed using the ALEPH algorithm `QIPBTAG` [48]. The algorithm begins with jet clustering. The standard ALEPH clustering threshold of $y_{\mathrm{cut}} = 0.01$ was used in this analysis, resulting in two to four jets for the majority of events. The jets are then momentum ordered, with the highest momentum ordered first. If no jets are clustered the event is discarded. However this very rarely happens and in fact never occurred in this analysis.

The event thrust axis and primary vertex were then calculated in order to divide the event into hemispheres. This is followed by track selection, as `QIPBTAG` only uses well reconstructed tracks. Each charged track is assigned an ALEPH track type from 1 - 9, as defined in Table 4.1. Tracks not fulfilling any of these criteria are

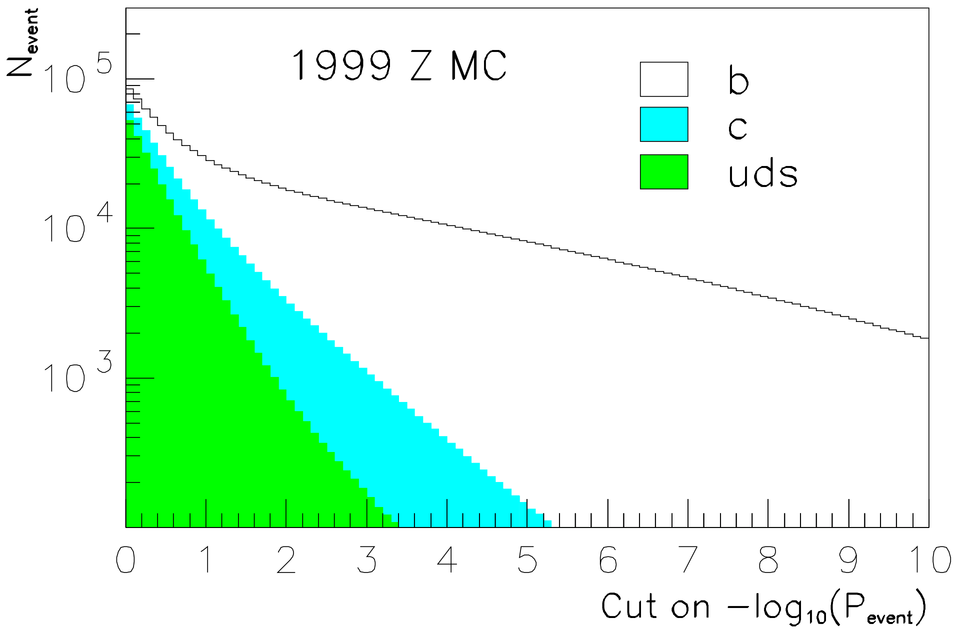

Figure 4.5: The number of events remaining (tagged) as a function of the cut on the negative logarithm of the event probability for 1999 Z Monte Carlo. The separate contributions from the light (uds), charm (c) and beauty (b) quarks are shown.

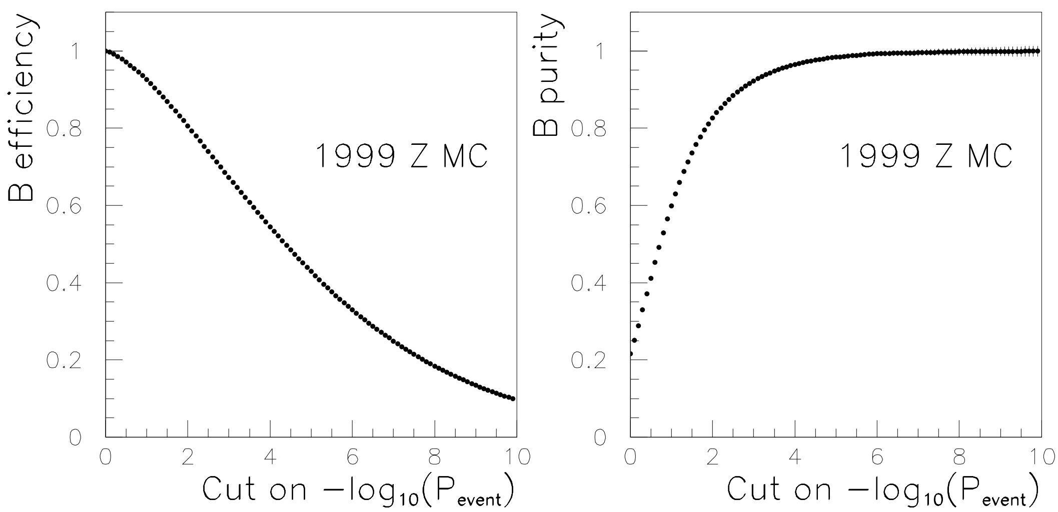

Figure 4.6: The B efficiency and B purity as function of the event b-tag in 1999 Z Monte Carlo. Due to the high Monte Carlo statistics available the statistical errors are negligible.

Track type	**Definition**
Type 1	2 VDET space point hits
Type 2	1 VDET space point hit, expect only 1
Type 3	V0 track
Type 4	1 VDET space point hit, expect 2
Type 5	Lots of ITC hits, no VDET hits, expect 0 VDET hits
Type 6	Lots of ITC hits, no VDET hits, expect some VDET hits
Type 7	1 r-ϕ or z hit in the ITC, expect 1
Type 8	1 r-ϕ or z hit, in the ITC, expect 2
Type 9	2 r-ϕ or z hits in the VDET

Table 4.1: The ALEPH track type definitions.

defined as type 0 and along with type 3 tracks are discarded from the calculation. Selected tracks are then assigned to their jets, with tracks in 5^{th} ordered jets or below also being discarded. Finally the jet, hemisphere and event probabilities are calculated as described in the Section 4.6.2.

4.6.4 The calculation of R_b using an event tag

Taking into account backgrounds, R_b at LEP2 using an event tag is defined as

$$R_b = \frac{N_{\rm sel} - B_{\rm sel}}{N_{\rm pre} - B_{\rm pre}} \times \frac{1.}{\epsilon_b} \tag{4.8}$$

where $N_{\rm sel}$ is the number of events selected (tagged) in data and $N_{\rm pre}$ is the number of events in the data preselection. The number of background events in the data selection and preselection are given by $B_{\rm sel}$ and $B_{\rm pre}$ respectively, which are both estimated from the Monte Carlo. The B selection efficiency ϵ_b is also taken from the Monte Carlo.

The selection background is defined as all non-B content plus any radiative hadronic events passing the selection cut:

$$B_{\rm sel} = B^{\rm sel}_{\rm udsc} + B^{\rm sel}_{\rm w} + B^{\rm sel}_{\rm z} + B^{\rm sel}_{\rm udscb\ rad} \tag{4.9}$$

where $B^{\rm sel}_{\rm udsc}$ is the number of non-radiative $udsc$ events, $B^{\rm sel}_{\rm w}$ and $B^{\rm sel}_{\rm z}$ are the number of W^+W^- and Z^0Z^0 events respectively, and $B^{\rm sel}_{\rm udscb\ rad}$ is the number of radiative hadronic events, all of which are estimated from the Monte Carlo.

The preselection background is defined as any non-hadronic and radiative events in the preselection:

$$B_{\mathrm{pre}} = B_{\mathrm{w}}^{\mathrm{pre}} + B_{\mathrm{z}}^{\mathrm{pre}} + B_{\mathrm{udscb\ rad}}^{\mathrm{pre}} \tag{4.10}$$

where $B_{\mathrm{w}}^{\mathrm{pre}}$, $B_{\mathrm{z}}^{\mathrm{pre}}$ and $B_{\mathrm{udscb\ rad}}^{\mathrm{pre}}$ are the number of W^+W^-, Z^0Z^0 and radiative hadronic events respectively in the data preselection, estimated from Monte Carlo.

The B event selection efficiency is also estimated from Monte Carlo and is defined as:

$$\epsilon_b = \frac{N_{\mathrm{b}}^{\mathrm{sel}}}{N_{\mathrm{b}}^{\mathrm{pre}}} \tag{4.11}$$

where $N_{\mathrm{b}}^{\mathrm{sel}}$ is he number of non-radiative B events passing the selection cut, and $N_{\mathrm{b}}^{\mathrm{pre}}$ is the number of non-radiative B events in the preselection.

4.6.5 Calculation of backgrounds

The estimated luminosity normalised number of non-radiative background events present in the data preselection or selection for a background component B is calculated according to:

$$B = \mathcal{L} \times \sigma \times \epsilon^{\mathrm{pre}}\epsilon^{\mathrm{sel}} \tag{4.12}$$

where $\mathcal{L}$ is the total data integrated luminosity and σ is the Standard Model cross-section for the background B. Taken from Monte Carlo are the preselection efficiency ϵ^{pre} and the selection efficiency ϵ^{sel}. In the case of estimating a preselection background, the selection efficiency $\epsilon^{\mathrm{sel}} = 1$.

The non-radiative preselection efficiency for a background B is given by:

$$\epsilon^{\mathrm{pre}} = \frac{B^{\mathrm{pre}}}{B^{\mathrm{orig}}} \tag{4.13}$$

where B^{pre} is the number of non-radiative preselected events after all preselection cuts and B^{orig} is the original number of non-radiative Monte Carlo events. This latter number was found by first removing all events $B^{s'<0.9}$ with $s' < 0.9$ according to the Monte Carlo truth information, leaving a sample of purely non-radiative events. A value for s' was then calculated for these non-radiative events as described in Section 4.5. Events with reconstructed $s' < 0.9$ were then removed from the sample so that $B^{\rm orig}$ events remained. The rest of the preselection cuts described in Section 4.5 were then applied in turn, resulting in the preselection sample $B^{\rm pre}$.

The non-radiative selection efficiency $\epsilon^{\rm sel}$ is defined as:

$$\epsilon^{\rm sel} = \frac{B^{\rm sel}}{B^{\rm pre}} \tag{4.14}$$

where $B^{\rm sel}$ is the number of tagged events from the preselection $B^{\rm pre}$.

The number of background radiative hadronic events was approximated as:

$$B_{\rm rad} = B \times \frac{B^{\rm pre}_{\rm rad}}{B^{\rm pre}} \tag{4.15}$$

where $B^{\rm pre}_{\rm rad}$ is the number of radiative hadronic events in the preselection. This was found by taking the sample of events $B^{s'<0.9}$ and treating them in exactly the same way as the non-radiative events. A value for s' was calculated for each event, and events with reconstructed $s' < 0.9$ removed from the radiative sample. The rest of the preselection cuts were then applied, resulting in a radiative preselection sample $B^{\rm pre}_{\rm rad}$.

4.6.6 The calculation of R_b using a hemisphere tag

For the double tag method exactly the same preselected event sample is used as for the event tag. Each event in the preselected sample is divided into two hemispheres by the plane passing through the primary vertex orthogonal to the thrust axis. The b-tag is then calculated for each hemisphere as described in Section 4.6.2. For a given selection cut on the b-tag the number of individual hemispheres selected in data, $f_{\rm s}$, is given by:

$$f_{\rm s} = \frac{R_b\epsilon_b + R_c\epsilon_{\rm c} + (1 - R_b - R_c)\,\epsilon_{\rm uds}}{(N/N_{\rm q})} + \frac{N_{\rm w}\epsilon_{\rm w} + N_{\rm z}\epsilon_{\rm z} + N_{\rm q\,rad}\epsilon_{\rm q\,rad}}{N} \tag{4.16}$$

where N is the number of hemispheres in the data preselection. $N_{\rm w}$, $N_{\rm z}$ and $N_{\rm q\,rad}$ are the number of W^+W^-, Z^0Z^0 and radiative hadronic hemispheres respectively in the data preselection, which are estimated from Monte Carlo. The uds, c, W^+W^-, Z^0Z^0 and radiative hadronic hemisphere selection efficiencies ϵ_{uds}, ϵ_{c}, ϵ_{w}, ϵ_{z} and $\epsilon_{\mathrm{q\,rad}}$ are also estimated from Monte Carlo. The charm branching ratio value R_c is taken as the Standard Model prediction. The number of non-radiative hadronic hemispheres N_{q} in the preselection is defined as:

$$N_{\mathrm{q}} \;=\; N - N_{\mathrm{w}} - N_{\mathrm{z}} - N_{\mathrm{q\,rad}} \quad . \tag{4.17}$$

The number of preselected hemispheres is simply twice the number of events in the preselection. The hemisphere selection efficiency for a component X is defined as

$$\epsilon_X \;=\; \frac{N_X^{\mathrm{sel}}}{N_X^{\mathrm{pre}}} \tag{4.18}$$

where N_X^{sel} is the number of hemispheres tagged and N_X^{pre} the number of preselected hemispheres.

The fraction of events in data with *both* hemispheres tagged, f_{d}, is given by

$$f_{\mathrm{d}} = \frac{R_b\epsilon_b^2\left(1+\rho_b\right) + R_c\epsilon_{\mathrm{c}}^2 + \left(1 - R_b - R_c\right)\epsilon_{\mathrm{uds}}^2}{\left(N^{\mathrm{e}}/N_{\mathrm{q}}^{\mathrm{e}}\right)} + \frac{N_{\mathrm{w}}^{\mathrm{e}}\epsilon_{\mathrm{w}}^2 + N_{\mathrm{z}}^{\mathrm{e}}\epsilon_{\mathrm{z}}^2 + N_{\mathrm{q\,rad}}^{\mathrm{e}}\epsilon_{\mathrm{q\,rad}}^2}{N^{\mathrm{e}}} \tag{4.19}$$

where N^{e} is the number of preselected events in data. $N_{\mathrm{w}}^{\mathrm{e}}$, $N_{\mathrm{z}}^{\mathrm{e}}$ and $N_{\mathrm{q\,rad}}^{\mathrm{e}}$ are obtained from Monte Carlo and are the estimated number of W^+W^-, Z^0Z^0 and radiative hadronic events respectively in the data preselection. Due to correlations in the B hemisphere tagging efficiency, the probability of tagging both hemispheres in a B event is not exactly ϵ_b^2. This is taken into account by the factor ρ_b, which is defined as

$$\rho_b = \frac{\epsilon_{\mathrm{b}}^{\mathrm{d}} - \epsilon_{\mathrm{b}}^2}{\epsilon_{\mathrm{b}}^2} \tag{4.20}$$

where ϵ_{b} is the B hemisphere tagging efficiency and $\epsilon_{\mathrm{b}}^{\mathrm{d}}$ is the efficiency for tagging both hemispheres in a B event, both of which are estimated from the Monte Carlo. Reasons for this correlation in the B hemisphere tagging efficiency are discussed in Section 4.6.7. The number of non-radiative hadronic events N_{q} in the preselection is defined as:

$$N_{\mathrm{q}}^{\mathrm{e}} \;=\; N^{\mathrm{e}} - N_{\mathrm{w}}^{\mathrm{e}} - N_{\mathrm{z}}^{\mathrm{e}} - N_{\mathrm{q\,rad}}^{\mathrm{e}} \quad . \tag{4.21}$$

The derivation of Equations 4.16 and 4.19 is given in Appendix A. These equations may then be solved simultaneously for ϵ_b and R_b, which is also shown in Appendix A.

4.6.7 Hemisphere correlations

Due to correlations in the efficiency of tagging both hemispheres in an event, the probability of tagging both hemispheres in a B event is not exactly ϵ_b^2. This is due to the following reasons:

- The geometrical acceptance of ALEPH. Due to the conservation of momentum, the majority of B jets are back-to-back. Thus if one jet falls in a region of poor detector acceptance, then it is likely that the other will as well. Since the b-tagging probability is therefore reduced in both hemispheres, a positive correlation in the tagging efficiencies between the two hemispheres is introduced.

- The effect of hard and soft gluon radiation. The radiation of a soft gluon will reduce the momentum of B jets, resulting in greater multiple scattering of tracks. This results in lower track resolutions and therefore a positive correlation. Conversely, in about 2 % of events, a hard gluon is emitted, which may result in both B jets being in the same hemisphere. The event is therefore very likely to tag in one hemisphere, and not in the other, introducing a negative correlation.

- A shared primary vertex between hemispheres. If tracks from both hemispheres are used in the reconstruction of the primary vertex, then tracks from a long lived B hadron in one hemisphere will increase the reconstruction error. This will result in decreased impact parameter significances in the other hemisphere, thus reducing the tagging probability and introducing a negative correlation.

In principle this tagging correlation also applies to the non-B content. However due to the suppression of the non-B content by the tag, such corrections were found to be negligible.

4.6.8 Event and hemisphere tag comparison

The principle difference between the two tagging methods is that the hemisphere tag allows the B efficiency ϵ_b to be measured from data, whilst the event tag relies on an estimation from Monte Carlo. The hemisphere tag is therefore a more reliable method, although it suffers from a poorer statistical resolution as both R_b and ϵ_b are being measured from the data. However, in using Monte Carlo to estimate ϵ_b, the event tag suffers from an additional source of systematic error.

The measurement of R_b at LEP1 [1] where very high statistics were available (nearly four million hadronic events) was therefore made with a hemisphere tag. Even with the poorer statistical resolution, systematic errors dominated. However, previous measurements at LEP2 have all been made with an event tag [20], as typically only a few hundred hadronic events were available at each energy point.

The total statistics available at 189 - 207 GeV made the use of the hemisphere tag plausible. In this analysis both the event and hemisphere tags were therefore used to measure R_b. As described in Section **??** and Chapter 8 the hemisphere tag was used to calibrate the event tag, thus utilising the reliability of the hemisphere tag whilst capitalising on the higher statistical resolution afforded by the event tag.

4.7 The selection cut

Due to low statistics, earlier measurements of R_b at lower LEP2 energies have only ever been made using an event tag. For these measurements, the selection cut was chosen to be the point at which the statistical significance of the signal ($b\bar{b}$ events) was maximised, according to Monte Carlo.

The statistical significance of a signal is defined as the number of sigma (standard deviations) the signal is away from the background. For any data count N with background B the signal, S, is $N - B$. The error on B is $\sqrt{B}$, so that the statistical significance σ_s of the signal S is given by:

$$\sigma_s = \frac{N - B}{\sqrt{B}} = \frac{S}{\sqrt{B}} \quad . \tag{4.22}$$

Figure 4.7 shows $S/\sqrt{B}$ as a function of the event b-tag for 200 GeV Monte Carlo.

In principle this method may also be used for selecting a hemisphere cut value. However, measurements of R_b using a hemisphere tag at LEP2 suffer from a larger statistical uncertainty than the event tag method. It was therefore decided to adopt a policy of error minimisation when choosing the selection cut, for both the event tag and hemisphere tag methods. The selection cut chosen for each method is then the cut value at which the total *fractional* error on R_b is minimised. This is also the method by which the selection cut was chosen for the LEP1 measurement.

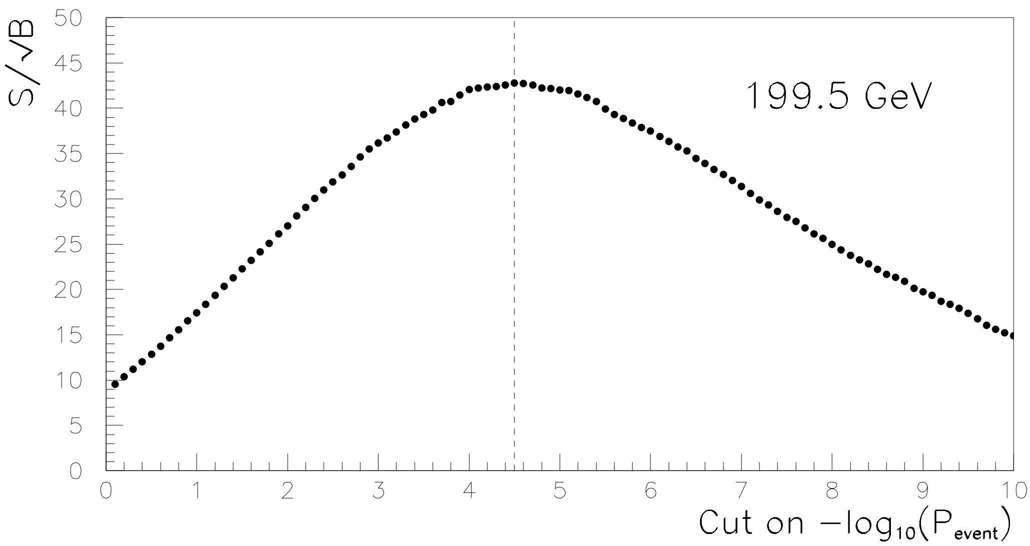

Figure 4.7: Signal statistical significance as a function of the b-tag from Monte Carlo, showing a maximum at a cut of 4.5.

4.8 The hadronic preselection efficiency correction

As events or hemispheres were selected from a preselected sample of hadronic events, the quantity actually being measured is given by

$$R_b^{\mathrm{pre}} = \frac{N_{\mathrm{b}}^{\mathrm{pre}}}{N_{\mathrm{q}}^{\mathrm{pre}}} \tag{4.23}$$

where $N_{\mathrm{b}}^{\mathrm{pre}}$ is the number of B events or hemispheres in the non-radiative hadronic preselection $N_{\mathrm{q}}^{\mathrm{pre}}$. As described in Section 4.3 the preselection cuts remove ~8 % of hadronic events. Taking into account hadronic preselection efficiencies, R_b is given by

$$R_b = \frac{\epsilon_{\mathrm{q}}^{\mathrm{pre}}}{\epsilon_{\mathrm{b}}^{\mathrm{pre}}} \times \frac{N_{\mathrm{b}}^{\mathrm{pre}}}{N_{\mathrm{q}}^{\mathrm{pre}}} = \frac{\epsilon_{\mathrm{q}}^{\mathrm{pre}}}{\epsilon_{\mathrm{b}}^{\mathrm{pre}}} \times R_b^{\mathrm{pre}} \tag{4.24}$$

where $\epsilon_{\mathrm{b}}^{\mathrm{pre}}$ and $\epsilon_{\mathrm{q}}^{\mathrm{pre}}$ are the B preselection efficiency and overall hadronic preselection efficiency respectively. This correction for the preselection efficiencies results in an adjustment to R_b^{pre} of $\sim$0.5 %, which is small compared to the uncertainty due to statistics for both the event and hemisphere tags.

4.9 Evaluation of statistical errors

The evaluation of R_b involves the selection of events (hemispheres) from some original event (hemisphere) sample. As such the errors on R_b are described by binomial statistics. If N_{sel} events (hemispheres) are selected from a preselection sample of N_{pre} events (hemispheres) then the statistical error $\sigma_{N_{\mathrm{sel}}}$ on N_{sel} is given by:

$$\sigma_{N_{\mathrm{sel}}} = \left[N_{\mathrm{sel}}\left(1 - \frac{N_{\mathrm{sel}}}{N_{\mathrm{pre}}}\right)\right]^{\frac{1}{2}} \tag{4.25}$$

for which a proof may be found in reference [49]. Likewise the statistical error $\sigma_{N_{\mathrm{pre}}}$ on the number of events (hemispheres) in the preselection sample is given by:

$$\sigma_{N_{\mathrm{pre}}} = \left[N_{\mathrm{pre}}\left(1 - \frac{N_{\mathrm{pre}}}{N_{\mathrm{orig}}}\right)\right]^{\frac{1}{2}} \tag{4.26}$$

where N_{orig} is the number of exclusive events (hemispheres) in data before any preselection cuts. The resulting statistical error on R_b was then calculated according to standard error propagation.

Chapter 5

Performance of the b-tag

5.1 Introduction

As previously discussed, the measurement of R_b using an event tag relies on Monte Carlo to estimate the B selection efficiency. It was therefore important to validate the B physics modelling in the Monte Carlo and the performance of the b-tag.

This chapter describes how the b-tagging performance was evaluated using Z^0 calibration data and semi-leptonic W^+W^- LEP2 data. Measurements of R_b and impact parameter significance distributions at the Z^0 peak motivated an investigation into tracking differences between data and Monte Carlo. The B selection efficiency modelling in Monte Carlo was then investigated by comparing the hemisphere selection efficiencies in data and Monte Carlo. Finally the tagging of $udsc$ background was checked using hadronic jets in semi-leptonic W^+W^- events.

5.2 Evaluation of the b-tag using Z^0 data

Impact parameters are a function of transverse momentum and interaction energy. The collimation of jet tracks increases with energy, reducing the impact parameters of tracks from secondary vertices. However, this is effectively balanced by the longer decay lengths of the primary particles, so that impact parameters have only a small dependence on the interaction energy. Impact parameters are the raw information used in the b-tag in this analysis, and thus the b-tag performance is, to first order,

Flavour	Cross-section (nb^{-1})
$u\overline{u}$	4.86
$d\overline{d}$	6.19
$s\overline{s}$	6.19
$c\overline{c}$	4.86
$b\overline{b}$	6.08

Table 5.1: Standard Model cross-sections at the Z^0 peak.

independent of the interaction energy. As the World Average (WA) value for R_b at the Z^0 peak is well known [8] and in close agreement with the Standard Model prediction, data taken at this energy provided a convenient method of evaluating the b-tag performance at higher LEP2 energies.

Each year, prior to running at normal LEP2 energies, LEP was run for approximately one week at the Z^0 peak for detector calibration purposes. Due to the high cross section for $\mathrm{e^+e^-} \rightarrow Z^0$ interactions at this energy, approximately 100k events were recorded by ALEPH during each year's calibration run. The data recorded by ALEPH in 1998, 1999 and 2000 are shown in Table 3.1. These data were therefore used for the b-tag performance studies.

5.3 Measurement of R_b at Z^0 peak

The performance of the event tag was first evaluated by measuring R_b at the Z^0 peak for a range of selection cuts. The methodology was the same as that described in chapter 4 for the LEP2 measurements. However, the preselection was simplified as there were no W-pair, Z-pair or radiative return background events to suppress. The only preselection cuts applied therefore were the `CLASS16` and VDET acceptance cuts. The resulting hadronic preselections for the years 1998, 1999 and 2000 were 78,845, 90,001 and 98,365 events respectively. The $q\overline{q}$ cross-sections used in the estimation of the selection backgrounds were calculated using the program `ZFITTER` version 6.35 [50] and are shown in Table 5.1.

R_b as a function of the event tag for 1998, 1999, 2000 and for all three years combined is shown in Figure 5.1. The results for 1998 are seen to be very high

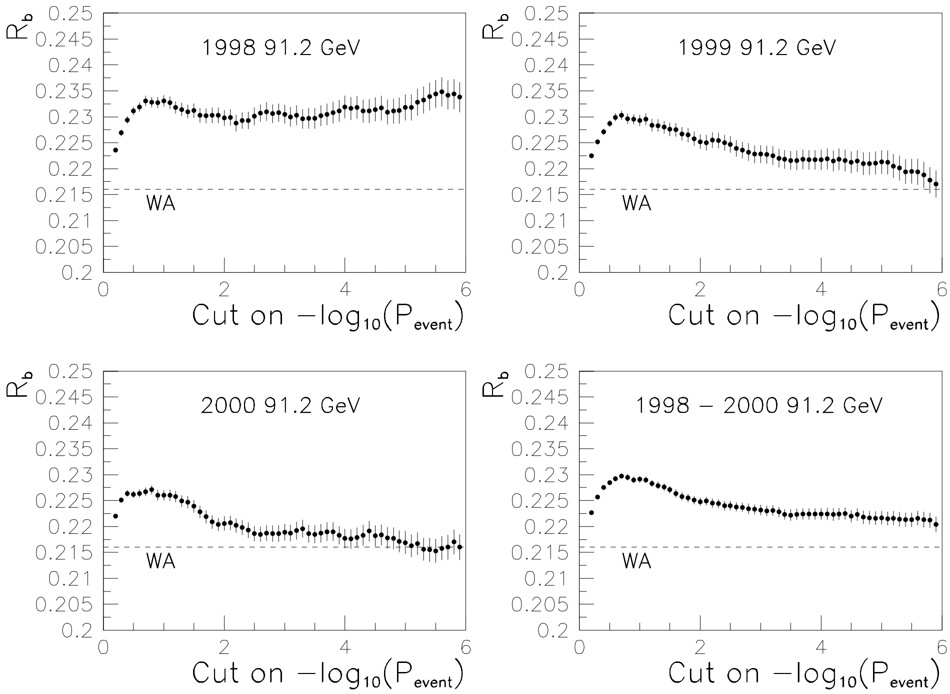

Figure 5.1: R_b as a function of the event tag at the Z^0 peak for the three years 1998 - 2000 and all data combined. The errors are the statistical errors only.

compared to the the world average. Additionally, there is an obvious peak in R_b at low cut values for 1999, 2000 and all the data combined. From Equation 4.8 it can be seen that a high value for R_b would be obtained if either the selection backgrounds or the B event selection efficiency are underestimated[1]. These results were therefore an indication of a discrepancy between the tagging behaviour in data and Monte Carlo. A further check on the tagging was performed by measuring R_b as a function of the event thrust angle for four different selection cuts. The behaviour for each of the three years was similar, with results for the combined data set shown in Figure 5.2.

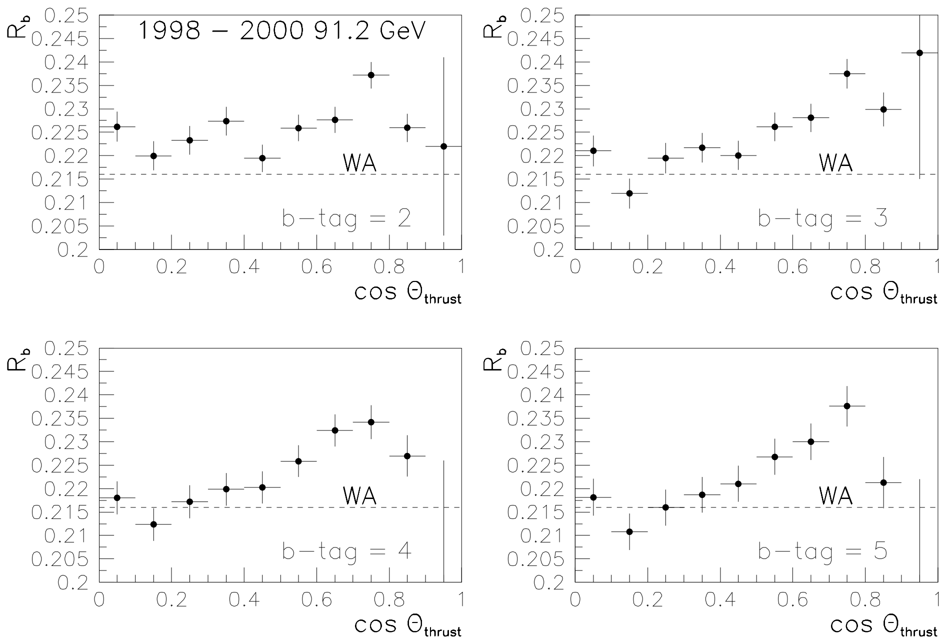

Figure 5.2: R_b as a function of thrust angle for four selection cuts for 1998 - 2000 Z^0 data. The errors shown are the statistical errors only.

R_b is seen to exhibit a clear dependence on the thrust angle, which is particularly well defined for the higher cut values. As R_b should be flat for all thrust angles, this is further evidence of a discrepancy in the tagging behaviour. Additionally, the effect is seen to be more prominent in regions of high B purity as it increases with

[1]At the Z^0 peak the preselection background is negligible.

the selection cut.

As the b-tag is calculated from impact parameter significances, these results were indicative of differences between the impact parameter significance distributions in data and Monte Carlo. The impact parameter significance distributions for the whole hadronic preselection in data and Monte Carlo were therefore compared, as shown in Figure 5.3. The distributions on the positive side agree well. However it can be clearly seen that the Monte Carlo distribution is low compared to the data on the negative side. As the impact parameter significance resolution of ALEPH is taken from the fit $I(|S|)$ to the negative side of this distribution, it is important that it is well reproduced in the Monte Carlo. This, therefore, was the motivation for investigating the performance of impact parameter significance smearing routines, which aim to improve the agreement between the data and Monte Carlo tracking.

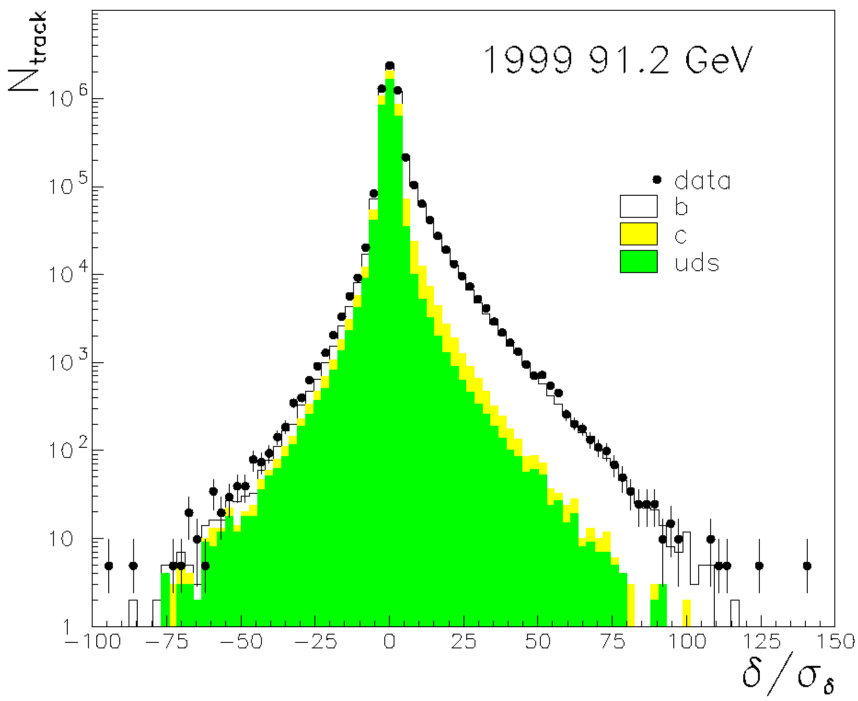

Figure 5.3: Track impact parameter significance distributions in 1999 Z^0 peak data and Monte Carlo. The light (uds), charm (c) and beauty (b) hadronic contributions to the Monte Carlo are also shown.

5.4 The ALPHA smearing routine QSMEAR

From Figure 5.3 it was observed that the impact parameter resolution is over-optimistic in the Monte Carlo. The ALPHA routine QSMEAR was written specifically for use in conjunction with QIPBTAG. QSMEAR reduces the Monte Carlo resolution by smearing the impact parameter uncertainty σ_δ in order to improve the agreement with data.

The smearing of the impact parameter uncertainties is performed according to a set of *smearing parameters*. These are generated by comparing exponential fits to the negative impact parameter significances in data and Monte Carlo for the whole data set. The smearing parameters are defined as the fraction of impact parameters A that have to be shifted by an amount k in order to maximise the impact parameter significance distribution agreement between data and Monte Carlo. The negative distributions are in fact best described by fitting two independent exponentials, one to describe the dominant central region and one to describe the distribution tail. The smearing parameters A_1, k_1 for the central region and A_2, k_2 for the tail were thus determined by finding the values which minimised the χ^2 between the corrected impact parameter significances in Monte Carlo and those in the data. These parameters were then used to randomly smear the impact parameters in Monte Carlo.

As the tracking resolution in ALEPH was heavily dependent on the number of VDET and ITC hits, smearing parameters were calculated separately for each of the ALEPH track types as defined in Table 4.1. Additionally, as the tracking resolution also had a momentum and polar angle dependence, it was also possible to calculate separate sets of parameters for tracks in three bins of momentum and/or in three bins of polar angle. There are therefore five possible smearing options:

- No smearing (Smearing = 0)
- Global smearing (Smearing = N)
- Smearing in bins of momentum (Smearing = P)

Track Type	k_1	A_1	k_2	A_2	A_3
Type 1	0.594	0.1237	5.355	0.0027	0.046
Type 2	1.055	0.1079	8.526	0.0125	-0.030
Type 3	0.296	0.6203	6.952	0.0103	0.062
Type 4	0.543	0.1079	25.306	0.0093	-0.039
Type 5	2.442	0.1646	6.508	0.0074	-0.136
Type 6	1.000	0.0000	5.000	0.0000	0.000
Type 7	0.170	0.3524	47.473	0.0347	-0.501
Type 8	1.000	0.0000	5.000	0.0000	0.000
Type 9	1.000	0.0000	5.000	0.0000	0.000

Table 5.2: Global smearing and deletion parameters for 1999 Z^0 Monte Carlo.

- Smearing in bins of thrust angle (Smearing = T)
- Smearing in bins of thrust angle and momentum (Smearing = B)

`QSMEAR` also provides a track deletion facility in order to compensate for an observed excess of `QIPBTAG` selected tracks in Monte Carlo compared to data, as shown in Figure 5.5(a). The track deletion randomly discards a certain fraction A_3 of each track type so that the number of `QIPBTAG` selected tracks in Monte Carlo matches that in data. The binning options for deletion are the same as those for the smearing, leading to a total of $5 \times 5 = 25$ smearing and deletion options. Global track deletion and smearing parameters for 1999 Z^0 Monte Carlo are shown in Table 5.2. Note that for some track types an excess is observed in the data, as the fraction of tracks to be removed is *negative*. As it is not possible to realistically add tracks to the Monte Carlo, this represents a limitation of the track deletion.

5.4.1 `QSMEAR` smearing performance

The performance of each of the smearing options was evaluated by comparing the corrected Monte Carlo impact parameter significance distributions with those in the data. The effect of global smearing with no track deletion is shown in Figure 5.4. The Monte Carlo impact parameter significance resolution has been decreased resulting in an improved agreement with the data. The results for the other binning options were very similar to the global smearing. This indicated that the tracking discrepancies between data and Monte Carlo with respect to the impact parameter measurements were not a function of track momentum or direction. Although the binning has negligible effect, it can be concluded that the application of smearing does result in an improved agreement with the data impact parameter significance resolution.

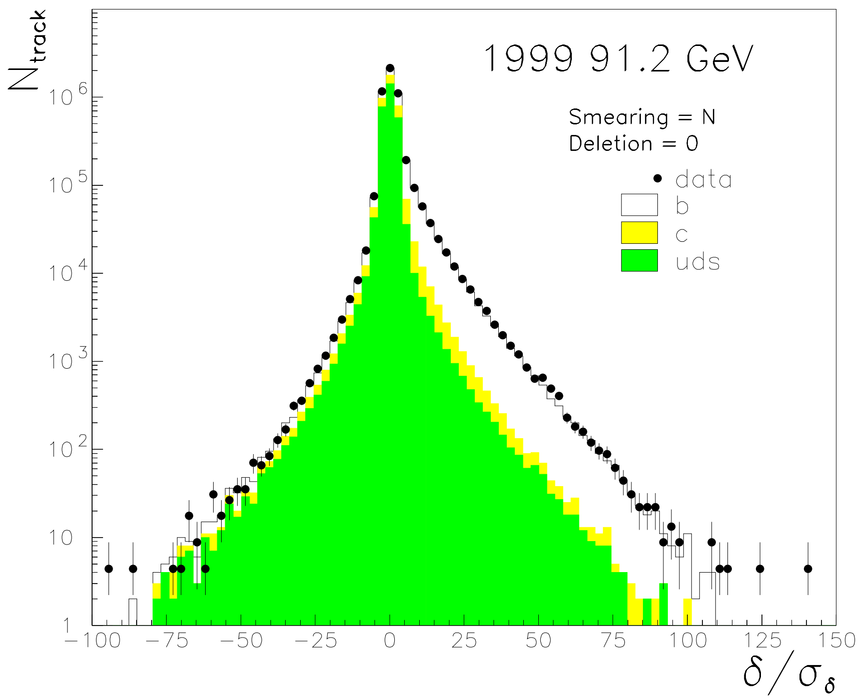

Figure 5.4: Track impact parameter significance distributions with global smearing and no track deletion for 1999 Z peak data and Monte Carlo. The light (uds), charm (c) and beauty (b) hadronic contributions to the Monte Carlo are also shown.

5.4.2 QSMEAR deletion performance

The performance of each of the track deletion options was evaluated by comparing the corrected QIPBTAG selected track multiplicities in Monte Carlo with data. Figure 5.5 shows both the original multiplicity distribution in Monte Carlo and the corrected distribution with global track deletion. A clear improvement is seen in the agreement with data for the track deleted distribution. However there is now a slight excess in the data track multiplicities. This is to be expected as the deletion option allows for the removal of tracks, but not the addition of tracks in the Monte Carlo. Again, the difference in performance with the other binning options was negligible. So even though the deletion does not allow for tracks to be added, the use of track deletion is seen to improve the agreement with data. The effect of deletion on the impact parameter significance distributions was negligible. This was expected as deletion does not alter the actual impact parameters. Likewise, smearing had no effect on the multiplicity distributions.

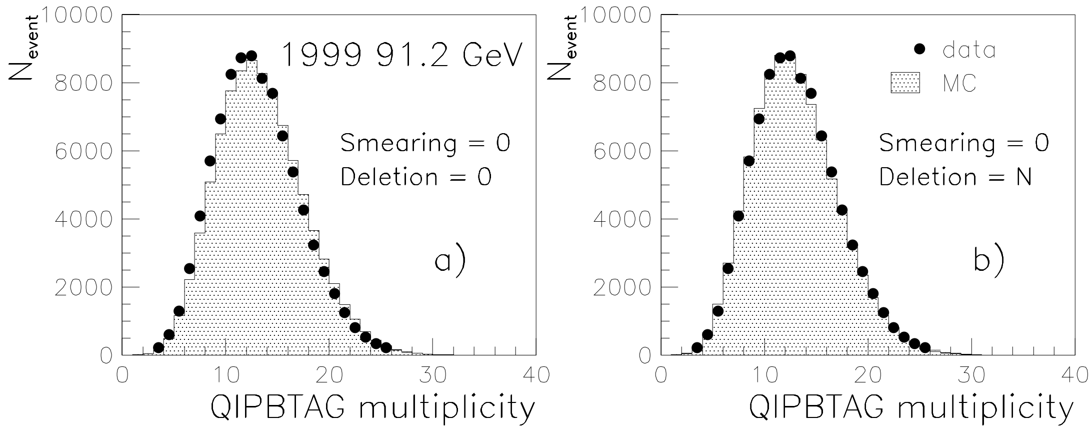

Figure 5.5: QIPBTAG selected track multiplicities for 1999 Z data and Monte Carlo with a) no track deletion and no smearing and b) global track deletion and no smearing.

5.5 The effect of track smearing on the b-tag

Having ascertained that `QSMEAR` smearing improves the Monte Carlo tracking agreement with data, the effect of smearing on the performance of the b-tag was then investigated. Measurements of R_b as a function of the event b-tag and as a function of the thrust angle were made for all three years Z^0 data with all smearing options and no track deletion.

From Figure 5.6 it can be seen that global smearing with no deletion significantly reduces the peak in measured R_b at low selection cut values and results in a much flatter distribution. Nevertheless, with the exception of the year 2000 results, statistically R_b is still significantly higher than the world average value. However the systematic error for these measurements is $\sim$3 %. With the exception of the year 1998 results, the largest discrepancies between R_b and the world average value are ∼2 %, so that these measured values for R_b are generally within one sigma of the world average value. The difference in performance between each of the binning options was negligible.

It was also hoped that the track smearing would reduce the observed dependence of R_b on the thrust angle. However, although tracks could be smeared as a function of the thrust angle, the differences between the performance of each of the binning options was again negligible. Figure 5.7 shows R_b as a function of the thrust angle with and without global smearing and no deletion. As expected the agreement with the world average value is improved, but the dependence on the thrust angle is still well defined for the higher selection cuts. The smearing therefore did not result in a reduced thrust angle dependence.

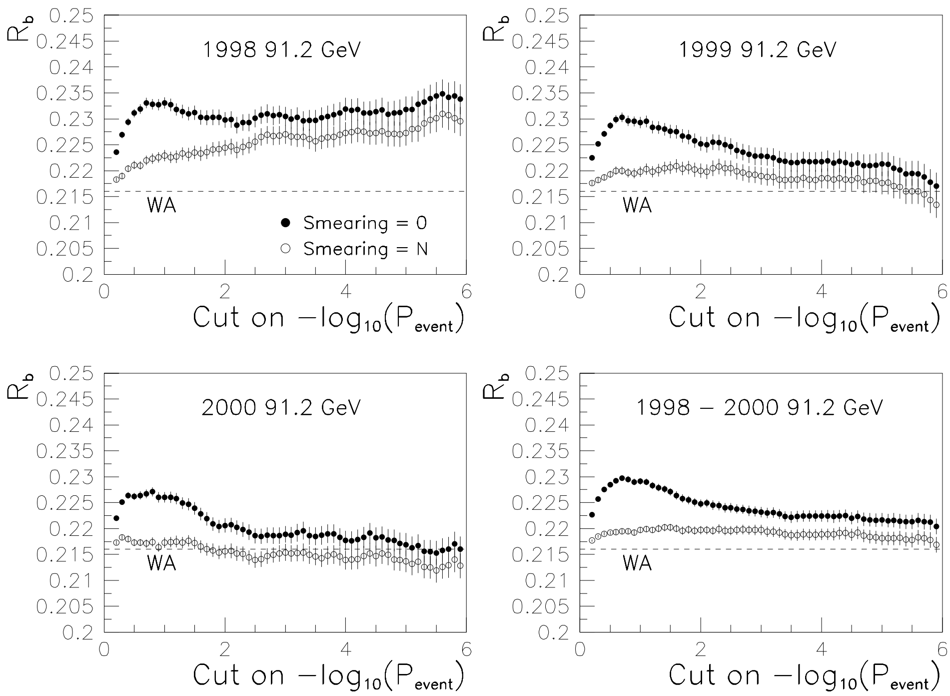

Figure 5.6: R_b as a function of the event tag at the Z^0 peak for the three years 1998 - 2000 and all data combined with and without smearing and no deletion. The errors are the statistical errors only.

The measurements of R_b with Monte Carlo track smearing with 1998 - 2000 Z^0 calibration data were seen to agree well with the Standard Model prediction and

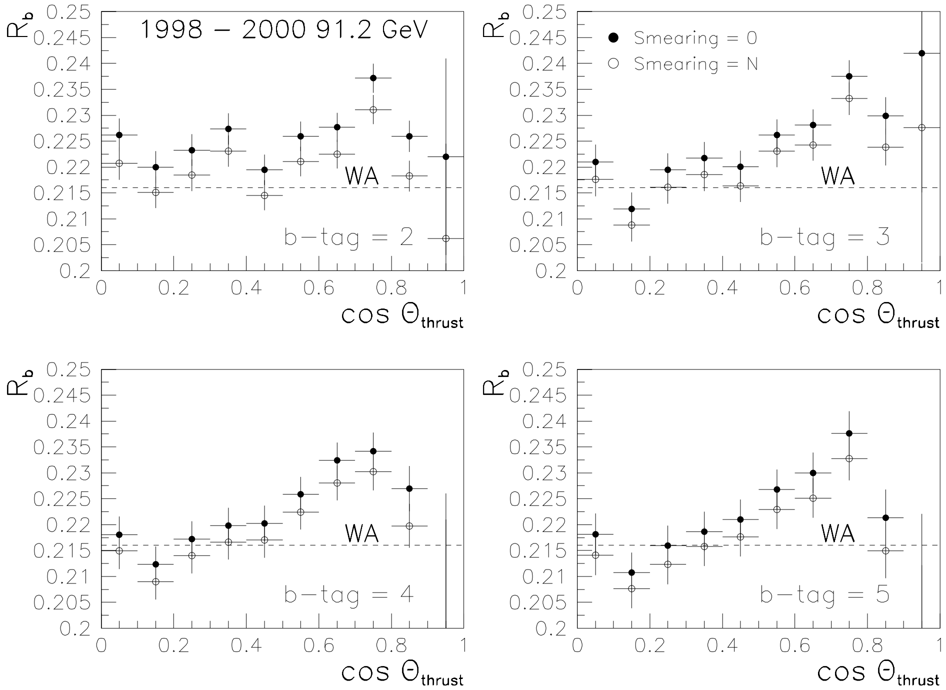

Figure 5.7: R_b as a function of thrust angle for four selection cuts for all 1998 - 2000 Z^0 peak data with and without smearing and no deletion. The errors are the statistical errors only.

the world average value. This therefore was evidence of a good b-tag performance at the Z^0 peak. However this does not guarantee that the B event selection modelling in the Monte Carlo is accurate. An increasing dependence on the thrust angle with the B selection purity is observed, and discrepancies between the B event selection efficiencies in data and Monte Carlo could be compensated for by discrepancies in the selection backgrounds. As the backgrounds at LEP2 energies were not the same as those at the Z^0 peak, it was important to check the B efficiency modelling in Monte Carlo.

As it is not possible to measure the B event selection efficiency from data, the B hemisphere selection efficiencies in data and Monte Carlo were compared. The B event and B hemisphere selection efficiencies are both based on the same data, so that the accuracy of the B hemisphere selection efficiency in Monte Carlo will provide a reasonable guide to the accuracy of the B event selection efficiency in Monte Carlo.

Figure 5.8 shows R_b as a function of the hemisphere tag with and without smearing, and the corresponding ratios of the B hemisphere selection efficiencies in data and Monte Carlo. As with the event tag, the smearing has dramatically reduced the peak in measured R_b at low tag values. However a well defined peak is still evident, indicating that the hemisphere tag is more sensitive to discrepancies in the tracking. The agreement between the data and Monte Carlo B hemisphere selection efficiencies is also improved with smearing. For the range $1.0 < b\text{-tag} < 3.0$ the efficiencies in data and Monte Carlo agree well, to within $\sim$0.5 % and one sigma on the statistical error. It is also seen that the better the agreement between the data and Monte Carlo efficiencies, the closer the value of R_b is to the world average. As the B efficiency seems well modelled for this range of cuts, it is reasonable to assume that the discrepancies for tag cuts above 3.0 are a result of low statistics. The discrepancy for tag cuts less than 1.0 is due in part to low statistics and additionally to tracking differences in data and Monte Carlo which have not been fully compensated for by the smearing. The difference between the performance of the other binning options was negligible.

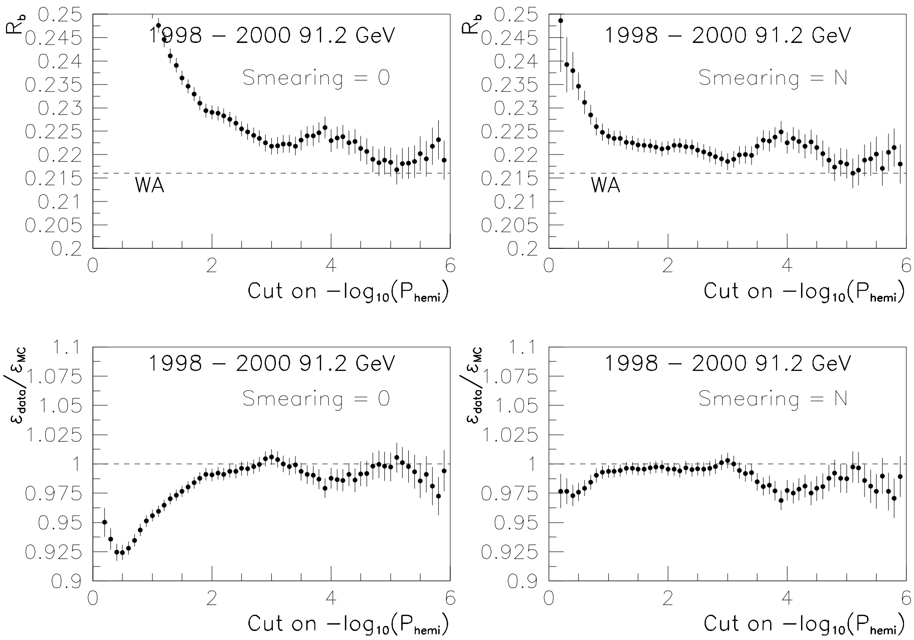

Figure 5.8: R_b (top) and the data over Monte Carlo B hemisphere selection efficiency ratios (bottom) as a function of the hemisphere tag for all 1998 - 2000 Z^0 peak data with no smearing (left) and global smearing (right). The errors are statistical errors only.

5.6 The effect of track deletion on the b-tag

The effect of deletion on the b-tag was then investigated. Measurements of R_b as a function of the event b-tag and as a function of the thrust angle were made for all three years Z^0 data with all deletion options and no track smearing.

Figure 5.9 shows the ratio of the B hemisphere selection efficiencies in data and Monte Carlo with global smearing and global deletion, and R_b as a function of the event tag with global smearing and global deletion. The agreement between the efficiencies is decreased with track deletion, and R_b is now seen to increase with the event tag. This deletion behaviour was the same for all binning options, and independent of the smearing. So although track deletion resulted in an improved agreement in the QIPBTAG selected track multiplicities, the performance of the b-tag was degraded.

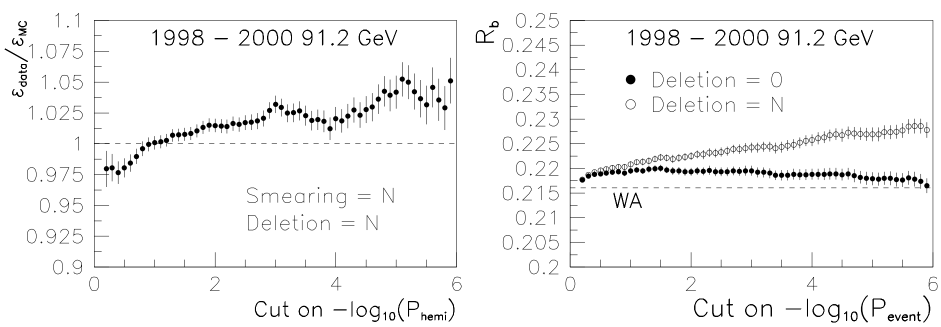

Figure 5.9: The data over Monte Carlo B hemisphere selection efficiency ratio with global track deletion and global smearing (left) and R_b as a function of the event tag for both global smearing with no track deletion and global smearing with global track deletion (right) for all 1998 - 2000 Z^0 peak data. The errors are the statistical errors only.

5.7 Smearing and deletion at LEP2

The use of QSMEAR smearing is seen to improve the agreement between the impact parameter significance distributions and the B hemisphere selection efficiencies in data and Monte Carlo. Additionally the smearing improves the results for measured R_b with both the event and hemisphere tags as a function of the selection cut, which agree with the world average and standard model values to within one sigma of the total error. For the region where the statistics are maximised the B hemisphere selection efficiencies in data and Monte Carlo agree statistically to within one sigma, indicating that the B event selection efficiency is also reasonably well modelled in the Monte Carlo. Discrepancies with the world average were therefore mostly due to other systematic uncertainties, including the background *udsc* modelling.

The use of `QSMEAR` smearing thus results in a good b-tag performance. However the results for measured R_b with the hemisphere tag are slightly higher than those measured with the event tag. As can be seen from Figure 5.8, this is probably due to the small discrepancies between the B selection efficiencies in data and Monte Carlo. However the use of `QSMEAR` track deletion is seen to degrade the tagging performance. It is likely that this effect is due to the inability to add tracks in regions of a track deficit in the Monte Carlo. It was therefore decided that track deletion should not be used for the measurement of R_b at LEP2.

As the differences between each of the smearing binning options was negligible, it was decided that the LEP2 measurements should use `QSMEAR` smearing with no binning (global smearing). This minimises the statistical uncertainty on the smearing parameters and is consistent with the smearing used in previous measurements [51]. The smearing parameters calculated using Z^0 data for each year 1998 - 2000 were therefore used to smear the impact parameters for LEP2 data taken during the same years.

5.8 B event selection efficiency correction

Previous measurements have taken the observed thrust angle dependence and the discrepancies between measured R_b and the world average value as evidence of a deficiency in the B event selection efficiency modelling in Monte Carlo. However, the studies presented here have demonstrated that the B efficiency modelling in the Monte Carlo appears reasonable and that the differences with the world average measurement are mostly due to other systematic effects. The B selection efficiency dependence on the thrust angle was checked by measuring the B efficiencies in data and Monte Carlo for two bins of thrust angle θ, $0. < \cos\theta < 0.5$ and $0.5 < \cos\theta < 0.9$. The agreement between data and Monte Carlo was found to be very similar to the global agreement. So although there is an observed thrust angle dependence at the Z^0 peak, it does not seem to be a result of inaccurate B physics modelling, and nor does it impact significantly on measured R_b. Therefore no thrust angle correction to the B event selection efficiency was applied.

5.9 W^+W^- physics study

As discussed earlier the tagging of *udsc* events may be responsible for discrepancies between R_b measured with 1998 - 2000 Z^0 calibration data and the world average value. In semi-leptonic W^+W^- events one W decays to a lepton and neutrino, whilst the other W decays hadronically to a quark and anti-quark. Due to the small mixing angles V_{ub} and V_{cb} from the Cabibbo-Kobayashi-Maskawa (CKM) [8] matrix, the hadronic decay $W^+ \to \overline{b} + c$ or u and its charge conjugate is rarely seen[2]. Semi-leptonic W^+W^- events at LEP2 therefore contain few B jets and thus provide a convenient method of checking the *udsc* tagging.

5.9.1 Event preselection

In W^+W^- production the two bosons are back-to-back in the centre of mass frame. Due to the large mass and charge of the W a leptonic decay therefore results in a single and usually isolated high energy (hard) lepton in the event. The neutrino being very weakly interacting and carrying no charge is invisible. The selection of semi-leptonic W^+W^- events was therefore based on identifying events with hadronic content and a single hard, isolated lepton.

This study used 189 GeV LEP2 data, from which the semi-leptonic W^+W^- preselection was obtained as follows. First purely leptonic events were suppressed by requiring that there be at least seven charged tracks in the event. This removes

[2] There was insufficient energy at LEP2 for top production to allow the decay channel $W^+ \to \overline{b}+t$ and its charge conjugate, for which the mixing angle is near unity.

$e^+e^- \to l\bar{l}$ lepton production events and W^+W^- or Z^0Z^0 production events where both the bosons decay leptonically. Leptons in the remaining events were identified using the `ALPHA` lepton identification routine `QSELEP` [42]. Isolated hard leptons were identified by clustering the event as described in Section 4.2 using a y_{cut} value of 0.002. This ensures a loose clustering of the event so that a lepton from one boson decay is not clustered with the hadronic jet from the second boson decay. A lepton was then defined as being hard and isolated if its energy was greater than 10 GeV and at least 90 % of the total jet energy to which it was clustered. Requiring only one single isolated hard lepton in the event thus suppressed $e^+e^- \to q\bar{q}$ events and fully hadronic Z^0Z^0 decays. Additionally this constraint suppressed any semi-leptonic Z^0Z^0 decays in which two hard isolated leptons are generally seen in the event[3]. Events satisfying these criteria therefore constituted the semi-leptonic W^+W^- preselection. According to Monte Carlo the Z^0Z^0, $q\bar{q}$ and fully hadronic W^+W^- background was $\sim$4 %.

5.9.2 Jet tagging

Each event (minus the identified hard lepton) in the preselection was then clustered into two jets, and each jet tagged as described in Section 4.6.2. A second purer sample of uds jets was also prepared by suppressing c jets. Due to the spin polarisation of the W, the forward-backward asymmetries of the W decay partons do not cancel. Therefore the production of each $udsc$ quark flavour is not isotropic in the W rest frame. A clear asymmetry is seen in Figure 5.10 which shows the number of uds and c jets in 189 GeV Monte Carlo as a function of the jet axis angle $\cos\theta$ in the W rest frame. By selecting forward jets with $\cos\theta > 0.$ in the W rest frame a purer sample of uds jets may thus be obtained.

The number of jets selected as a function of the b-tag in 189 GeV data and Monte Carlo for both the original jet sample and the purer uds sample, are shown in Figures 5.11(a) and (b). For both samples the Monte Carlo is seen to agree well with the data. The selection efficiencies for both samples as a function of the b-tag

[3]Of course a lepton may pass down the beam pipe and therefore not be detected.

are shown in Figures 5.11(c) and (d). Again a good agreement between data and Monte Carlo is seen. The disagreement for b-tag values > 3.0 is due to low statistics as it is not possible to have fractional events in data!

Although it was not possible to derive a quantitative conclusion from this study due to the difficulties of converting jet tags to hemisphere or event tags, the results were encouraging. In the regions of sufficient statistics data and Monte Carlo were seen to agree well and thus greatly increased confidence in the Monte Carlo *udsc* modelling.

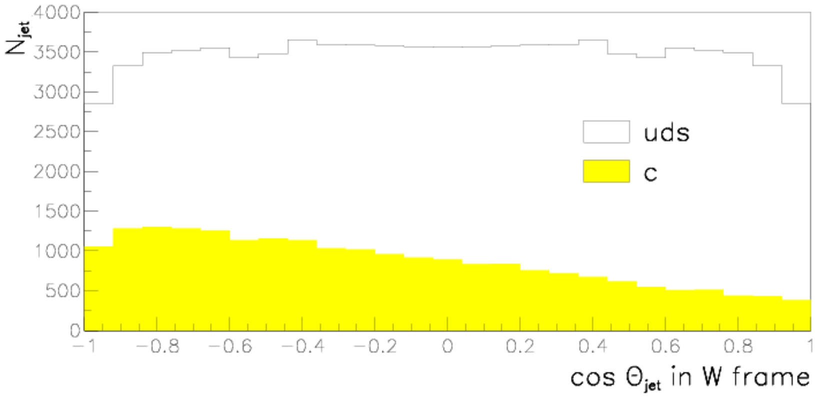

Figure 5.10: The angular distribution in the W rest frame of hadronic jets in 189 GeV semi-leptonic W^+W^- Monte Carlo. The separate *uds* and c contributions are shown, demonstrating a well defined asymmetry.

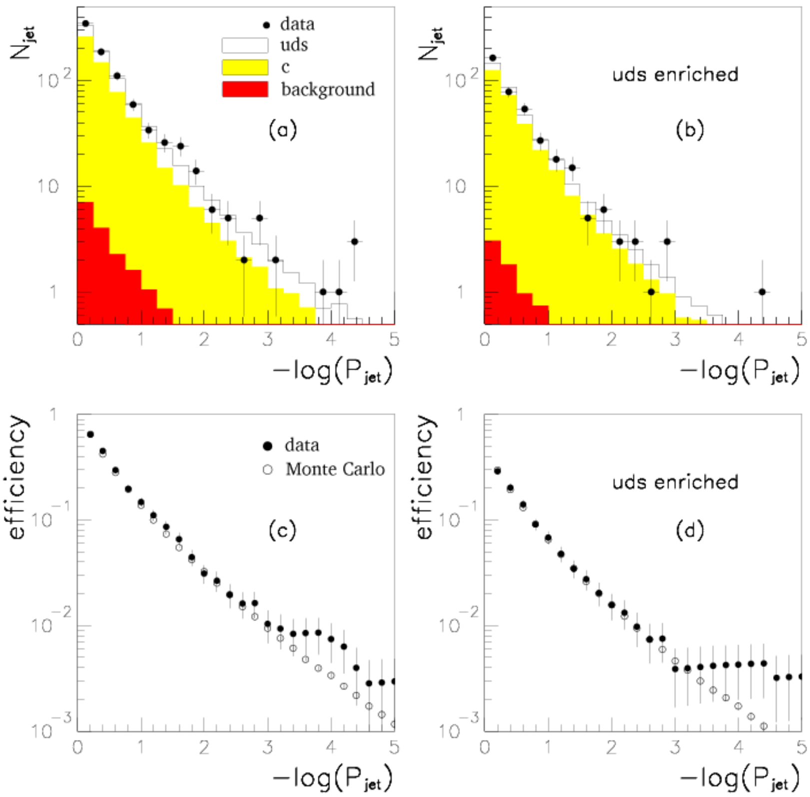

Figure 5.11: The number of jets selected (top) and the selection efficiencies (bottom) as a function of the b-tag for both the original semi-leptonic W^+W^- jet sample (left) and the purer uds sample (right) in 189 GeV data and Monte Carlo. The separate light (uds), charm (c) and background contributions to the Monte Carlo are also shown.

Chapter 6

R_b at 189 - 207 GeV using an event and hemisphere tag

6.1 Introduction

Having ascertained the b-tag performance at the Z^0 peak measurements of R_b were then made at the LEP2 energies of 189 - 207 GeV. The effect of track smearing was checked and a selection cut chosen for each tag based on the minimisation of the total errors. The chosen selection cuts for each tag were then used to extract the final values of R_b at each energy.

This chapter first presents a brief review of the analysis method. This is followed by a discussion on the extrapolation of the effects seen at LEP1 energies to LEP2 energies and a review of the smearing performance at LEP2 using Z^0 calibrated smearing parameters. The error analysis and the choice of selection cut is then described. The values of R_b obtained with each tag for all energies at 189 - 207 GeV, with the chosen selection cuts, are then presented.

6.2 Method

Hadronic events were selected from data recorded by the ALEPH detector during the three years 1998 - 2000 at each LEP2 energy point of 189, 192, 196, 200, 202, 205 and 207 GeV as described in Section 4.5. All Monte Carlo tracks were then globally smeared using the smearing parameters calculated from the appropriate year's Z^0

calibration data as described in Section 5.4. Next each event and hemisphere in the resulting preselection samples was tagged as described in Section 4.6.2. Values for R_b were then calculated for a range of selection cuts with both the event and hemisphere tags as described in Sections 4.6.4 and 4.6.6. Values for the statistical errors and all the systematic uncertainties considered were also calculated for both tags at each selection cut. This allowed the selection cut used to extract the final values of R_b at each energy point to be chosen according to the minimisation of the total fractional error. All the systematic uncertainties considered in this analysis and their evaluation are described in Chapter 7. Results for the whole 189 - 207 GeV data set were obtained by summing the data and normalised Monte Carlo event or hemisphere samples at each energy. For example:

$$N^{\rm all}_{\rm pre} = \sum_{\rm i=1}^{\rm i=7} N^{\rm i}_{\rm pre} \; ; \quad N^{\rm all}_{\rm sel} = \sum_{\rm i=1}^{\rm i=7} N^{\rm i}_{\rm sel} \tag{6.1}$$

where $N^{\rm all}_{\rm pre}$ and $N^{\rm all}_{\rm sel}$ are the total number of preselected and selected events or hemispheres respectively for the whole 189 - 207 GeV data set, with $N^{\rm i}_{\rm pre}$ and $N^{\rm i}_{\rm sel}$ the number of preselected and selected events or hemispheres respectively for energy i.

The number of data events and the estimated background content from Monte Carlo in each preselection sample for energies between 189 and 207 GeV are shown in Table 6.1. The Standard Model cross-sections used to calculate the number of events or hemispheres in the preselection and selection backgrounds at each energy are shown in Table 6.2.

6.3 Extrapolation of LEP1 effects to high energy

Although impact parameter significance magnitudes may be considered reasonably independent of the interaction energy as argued in Section 5.2, it was not clear how well effects measured with Z^0 data would actually transport to LEP2 energies. The main possible reasons for differences in the b-tag behaviour at LEP2 energies are:

- Impact parameter significance magnitudes having some dependence on the interaction energy.

Energy (GeV)	**Preselection Sample**	
	Data Events	**Background**
189	2952	315
192	485	52
196	1256	137
200	1279	140
202	611	63
205	1136	121
207	1831	198
Total	9550	1027

Table 6.1: The number of events in the data preselection samples for each energy between 189 and 207 GeV and the Monte Carlo estimated background contributions (to the nearest integer).

Energy (GeV)	**Standard Model cross-sections (nb^{-1})**						
	$u\overline{u}$	$d\overline{d}$	$s\overline{s}$	$c\overline{c}$	$b\overline{b}$	W^+W^-	Z^0Z^0
189	0.004896	0.003205	0.003205	0.004896	0.003227	0.016560	0.002759
192	0.004712	0.003064	0.003064	0.004713	0.003086	0.016899	0.002823
196	0.004479	0.002886	0.002886	0.004480	0.002909	0.017185	0.002855
200	0.004264	0.002724	0.002724	0.004264	0.002748	0.017383	0.002847
202	0.004156	0.002644	0.002644	0.004157	0.002668	0.017442	0.002847
205	0.003999	0.002529	0.002529	0.004000	0.002553	0.017523	0.002830
207	0.003926	0.002475	0.002475	0.003927	0.002500	0.017537	0.002810

Table 6.2: The Standard Model cross-sections at 189 - 207 GeV used to estimate the preselection and selection backgrounds.

- Greater fragmentation at LEP2 energies resulting in higher track multiplicities. Additionally as the B decay multiplicity is independent of energy, the fraction of tracks from secondary vertices is reduced.

- Additional contributions to the background. Energies of 189 GeV and above exceed the threshold for W-pair and Z-pair production. Initial state radiation also results in hadronic radiative return background.

Due to insufficient statistics the smearing parameters used for the LEP2 measurements were calculated from Z^0 calibration data. It was therefore necessary to check the effect of smearing 189 - 207 GeV Monte Carlo with Z^0 calibrated smearing parameters.

6.3.1 Smearing performance at 189 - 207 GeV

Measurements of R_b as a function of the event tag were made for all 189 - 207 GeV data both with and without global smearing using the smearing parameters calculated from Z^0 calibration data. Figure 6.1(a) shows R_b as a function of the event tag for all 189 - 207 GeV data combined with no smearing. Similarly to the Z^0 results a well defined peak is seen for low selection cut values. From Figure 6.1(b) global smearing is seen to reduce this peak resulting in a flatter distribution. However a peak still remains indicating that although the b-tag performance has been improved, the smearing does not fully correct for tracking discrepancies between data and Monte Carlo at low selection cut values.

Measurements of R_b were then made as a function of the hemisphere tag for all 189 - 207 GeV data both with and without global smearing. The B hemisphere selection efficiencies in data and Monte Carlo were also compared. From Figure 6.2 the smearing is again seen to improve the b-tag performance with a reduction in the peak. Additionally from Figure 6.2 the smearing is also seen to result in a closer agreement between the data and Monte Carlo B hemisphere selection efficiencies at low selection cut values.

Measurements of R_b at 189 - 207 GeV were also made with all the other smearing and deletion options. The difference in performance between the different smearing options was again negligible. The use of track deletion was seen to have a negligible effect on the results, independent of any smearing. It was therefore concluded that global smearing with no deletion should be used for the LEP2 analysis.

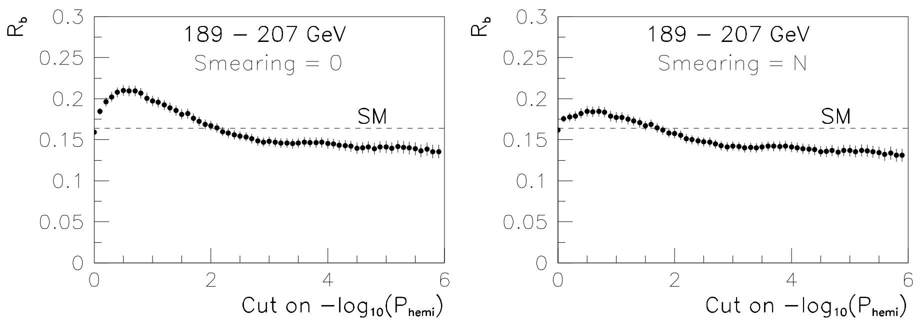

Figure 6.1: R_b as a function of the event tag with no smearing (left) and global smearing (right) for all 189 - 207 GeV data combined.

6.4 Optimum selection cut

The optimum selection cut for both the event and hemisphere tags was taken to be the point where the total fractional error on R_b was minimised. Figure 6.3 shows the statistical, systematic and total fractional errors on R_b with both the event and hemisphere tags for all 189 - 207 GeV data combined. The optimum selection cut for each tag was found by fitting a polynomial to the total error points and solving for the minimum point. A good fit for both the event and hemisphere tags was achieved using a third order polynomial:

$$y = ax^3 + bx^2 + cx + d \tag{6.2}$$

with the coefficients shown in Table 6.3. The minimum point is where $\partial y/\partial x = 0$, which gives a cut value of 2.8 for the event tag and 2.4 for the hemisphere tag. Combining the statistics from all energies allowed the most accurate determination of the optimum selection cut. These cut values were therefore also used for the measurements at each individual energy point. The resulting selection samples obtained with both the event and hemisphere tags are shown in Table 6.4.

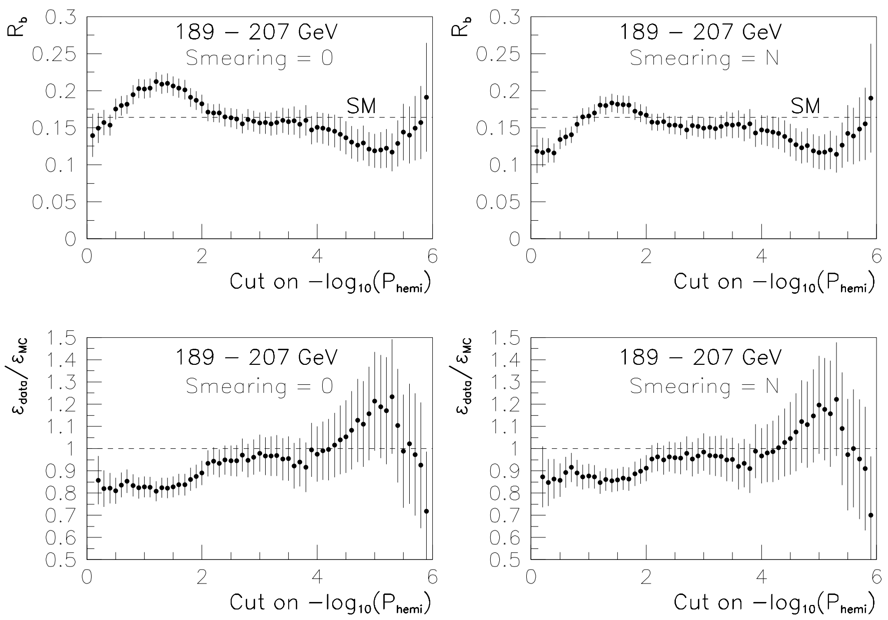

Figure 6.2: R_b (top) and the data over Monte Carlo B hemisphere selection efficiency ratios (bottom) as a function of the hemisphere tag for all 189 - 207 GeV data with no smearing (left) and global smearing (right). The errors are statistical errors only.

Tag	a	b	c	d
Hemisphere	-0.00055	0.02366	-0.10571	0.21220
Event	-0.00444	0.04685	-0.15571	0.22018

Table 6.3: The four coefficients used in the total fractional error third order polynomial fit for both the event and hemisphere tags.

Energy	**Event Selection**		**Hemisphere Selection**	
(GeV)	**Data**	**Background**	**Data**	**Background**
189	354	68	545	151
192	53	11	84	25
196	144	30	231	66
200	163	30	250	66
202	58	13	91	30
205	115	25	175	56
207	205	40	329	90
Total	1902	217	1705	483

Table 6.4: The number of events and hemispheres selected in data and the Monte Carlo estimated backgrounds (to the nearest integer).

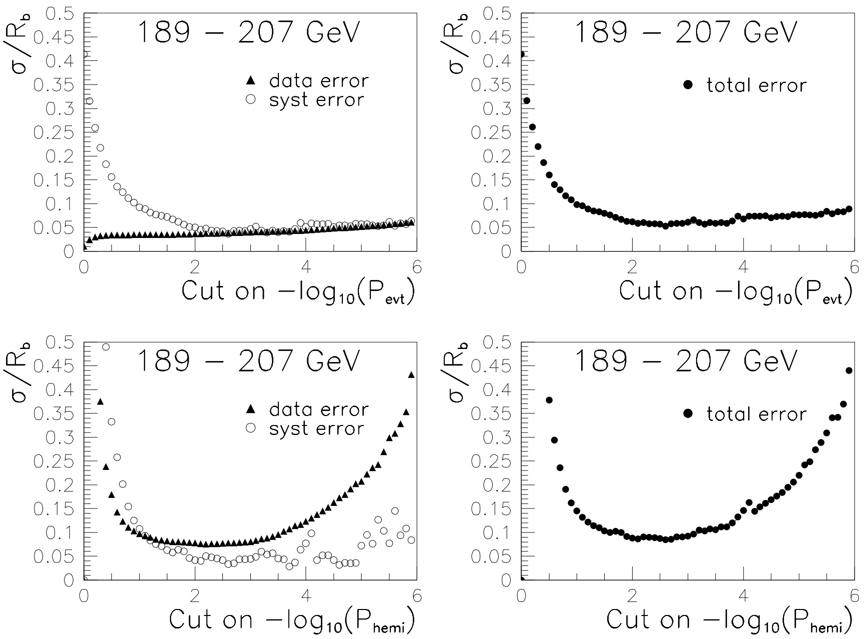

Figure 6.3: The statistical and systematic fractional errors (left) and the total fractional error (right) on R_b for all 189 - 207 GeV data combined as a function of the event tag (top) and the hemisphere tag (bottom).

6.5 The event and hemisphere tag results

R_b as a function of the event and hemisphere tags for all 189 - 207 GeV data combined is shown in Figure 6.4. Table 6.5 shows the results for R_b at each LEP2 energy point between 189 and 207 GeV, and for all the data combined, measured with the event tag and a selection cut of 2.8. The results for R_b using the hemisphere tag and a selection cut of 2.4 are shown in Table 6.6. All the systematic errors considered in this analysis are described in Chapter 7. The individual systematic errors evaluated for the event tag are shown in Table 7.21 and for the hemisphere tag in Table 7.22. The statistical errors were evaluated as described in Section 4.9. The event tag results and the hemisphere tag results as a function of energy, together with the previously published ALEPH results for R_b, are shown in Figures 6.5 and 6.6 respectively.

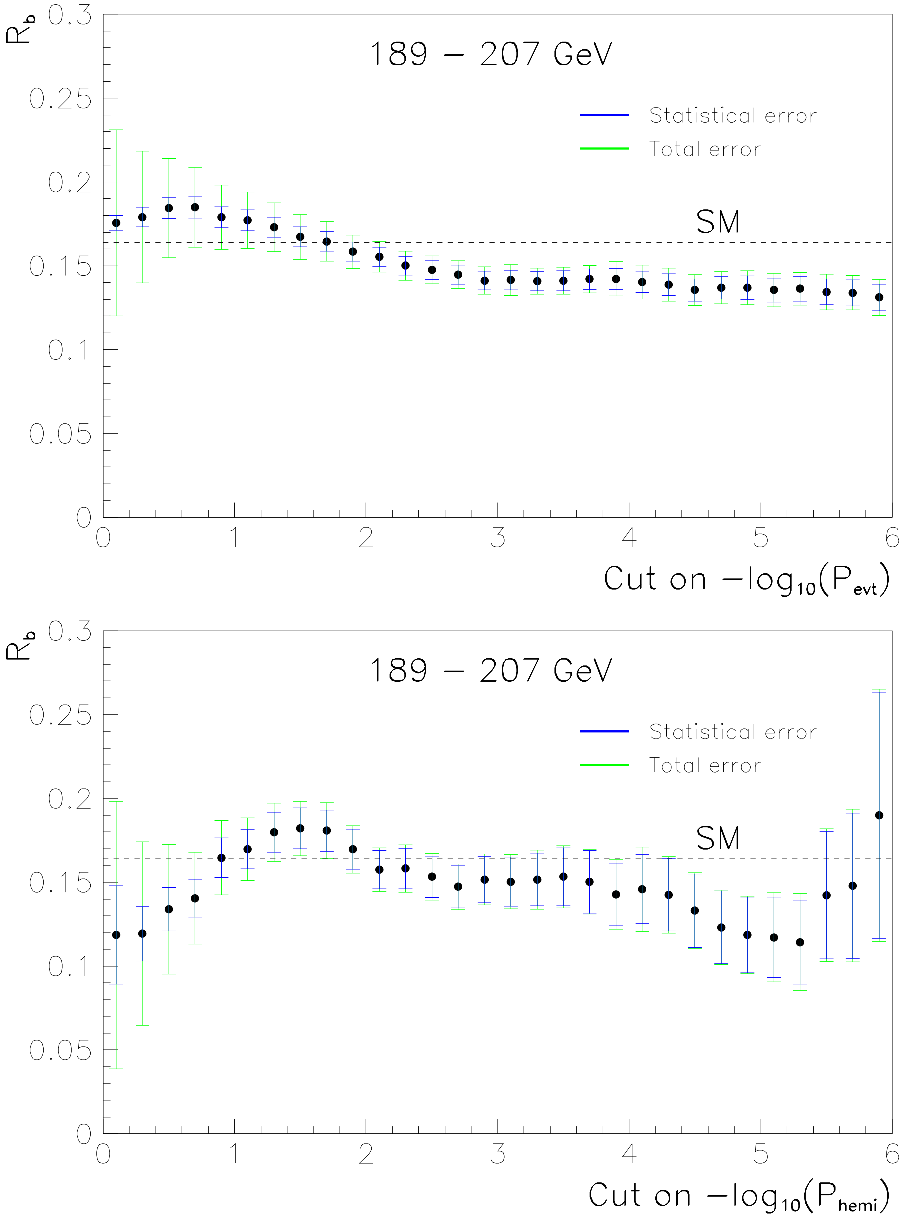

Figure 6.4: R_b as a function of the event tag (top) and the hemisphere tag (bottom) for all 189 - 207 GeV data combined. The Standard model prediction for R_b, the statistical errors and total errors are also shown.

Energy (GeV)	**Event tag results**			
	R_b	σ_{stat}	σ_{syst}	σ_{total}
189	0.15008	0.01033	0.00624	0.01207
192	0.13609	0.02430	0.00739	0.02540
196	0.14001	0.01540	0.00523	0.01626
200	0.16309	0.01624	0.00806	0.01813
202	0.12106	0.02079	0.01118	0.02361
205	0.12770	0.01570	0.00986	0.01854
207	0.13781	0.01280	0.00838	0.01530
189 - 207	0.14236	0.00564	0.00611	0.00832

Table 6.5: The event tag results for each LEP2 energy point between 189 and 207 GeV and all data combined. The statistical, systematic and total errors are also shown.

Energy (GeV)	**Hemisphere tag results**			
	R_b	σ_{stat}	σ_{syst}	σ_{total}
189	0.15054	0.02004	0.00690	0.02120
192	0.21387	0.08910	0.02866	0.09359
196	0.14702	0.03039	0.01011	0.03203
200	0.17667	0.03522	0.00923	0.03641
202	0.10347	0.03666	0.01729	0.04053
205	0.13314	0.03497	0.01163	0.03685
207	0.17622	0.03259	0.00802	0.03356
189 - 207	0.15138	0.01200	0.00692	0.01385

Table 6.6: The hemisphere tag results for each LEP2 energy point between 189 and 207 GeV and all data combined. The statistical, systematic and total errors are also shown.

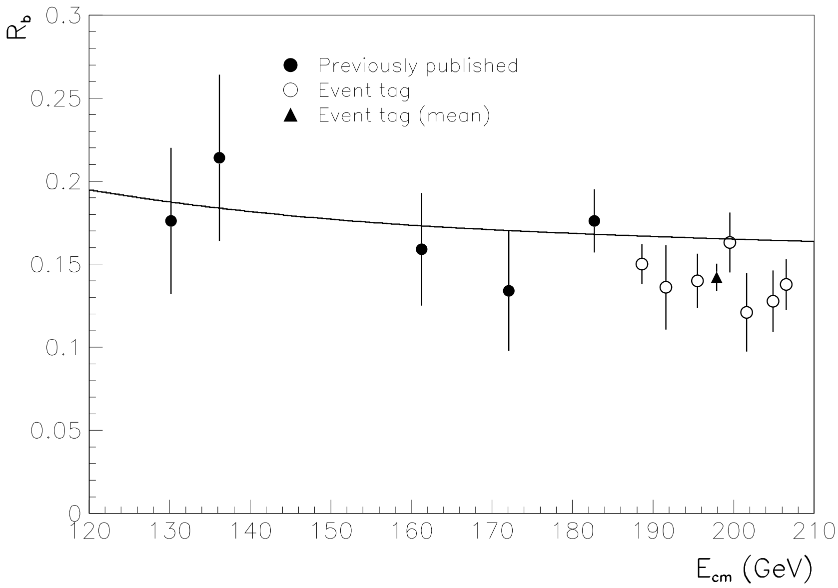

Figure 6.5: R_b at each energy and all data combined (189 - 207 GeV) measured with the event tag, plus the results previously published by ALEPH [3]. The Standard Model prediction for R_b as a function of energy is also shown.

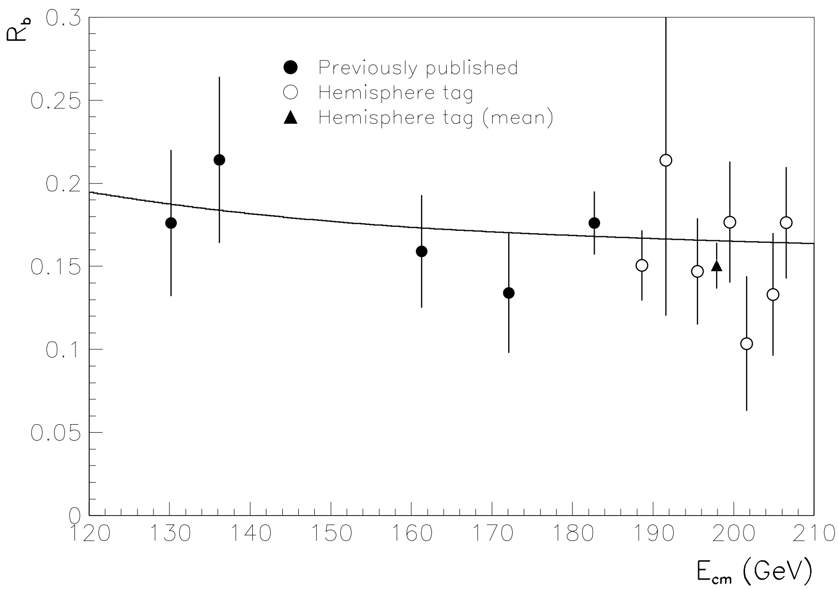

Figure 6.6: R_b at each energy and all data combined (189 - 207 GeV) measured with the hemisphere tag, plus the results previously published by ALEPH [3]. The Standard Model prediction for R_b as a function of energy is also shown.

Chapter 7

Systematic errors

7.1 Introduction

Due to the low statistics of LEP2 data the dominant error in the measurement of R_b is the statistical error. Therefore very precise evaluations of the systematic errors are not necessary. For example no detailed studies of charm physics were made in this analysis. The uncertainties evaluated were thus more general estimations of the main contributions to the systematic error on R_b.

This chapter discusses the treatment and evaluation of all the systematic effects considered in this analysis. The resulting errors are presented for each energy with both the event and hemisphere tag methods. The calibration of the event tag with the hemisphere tag and the calculation of the final errors is discussed in Chapter 8.

7.2 Evaluation of systematic errors

Systematic errors on R_b were evaluated by weighting events, changing cuts or adjusting theoretical parameters as described in the following sections. The resulting error on R_b was calculated according to standard error propagation. If $R_b = R_b(x, y, ..)$ where x and y are parameters from data or Monte Carlo then

$$\sigma_{R_b}^2 = \left(\frac{\partial x}{\partial R_b}\right)^2 \sigma_x^2 + \left(\frac{\partial y}{\partial R_b}\right)^2 \sigma_y^2 + ... \tag{7.1}$$

where the values for σ_x, σ_y etc. were taken as the difference in the values of x and y obtained when applying the systematic effect. Each parameter was assumed to be independent.

Energy (GeV)	σ_{R_b} ($y_{\rm cut} \pm 50$ %)	
	Event tag	**Hemi tag**
189	0.00366	0.00424
192	0.00523	0.02212
196	0.00155	0.00434
200	0.00666	0.00633
202	0.00853	0.01216
205	0.00840	0.00840
207	0.00450	0.00654
189 - 207	0.00319	0.00289

Table 7.1: The systematic errors σ_{R_b} for each energy due to $y_{\rm cut}$.

7.3 The $y_{\rm cut}$ jet clustering parameter

The `ALPHA` b-tagging routine `QIPBTAG` uses jet axes in determining the interaction point. The way that tracks are clustered will therefore affect the calculated primary vertex position and thus the measured impact parameters. The clustering also determines what tracks are used in the tagging calculation as tracks in fifth ordered jets and below are discarded. Additionally if a jet axis is redefined such that an impact parameter falls in the opposite hemisphere, then that impact parameter will change sign. The way that jets are clustered may therefore lead to differences in the tracks selected, the impact parameters of those tracks and their sign. The standard ALEPH $y_{\rm cut}$ value is 0.01. In order to estimate the uncertainty on R_b due to the choice of $y_{\rm cut}$, this value was varied by ± 50 % in data, Monte Carlo and in the calculation of the smearing parameters. The two error values σ_{R_b} obtained for $y_{\rm cut}$ $+50$ % and $y_{\rm cut}$ -50 % were averaged to obtain the systematic uncertainty for each energy due to $y_{\rm cut}$, which are shown in Table 7.1.

7.4 `QIPBTAG` track selection

Track impact parameters are the raw input for the b-tag and therefore the `QIPBTAG` track selection was looked at in some detail. Figure 7.1 shows the distribution of ALEPH "good" [1] track multiplicities before `QIPBTAG` track selection and the track multiplicities for the tracks remaining after `QIPBTAG` track selection in data and

[1] Definition later in the section.

Monte Carlo. It can be seen that before any track selection cuts the multiplicity distributions for good tracks in data and Monte Carlo agree well. However the QIPBTAG selected track multiplicity distributions in data and Monte Carlo are not seen to agree so well, with a difference between the mean of the two distributions of $\sim$0.75 tracks.

The track type distributions for *all* tracks in data and Monte Carlo before QIPBTAG selection are shown in Figure 7.2 (a), whilst the track type distribution for all remaining tracks after QIPBTAG selection is shown in Figure 7.2 (b). The fraction of tracks selected (the ratio of remaining tracks over initial tracks) in data and Monte Carlo is shown in Figure 7.2 (c), with the data over Monte Carlo selection fraction ratios shown in Figure 7.2 (d). From these figures it can be seen that the fraction of tracks selected for track types 1, 2 and 4 are very similar in data and Monte Carlo. However the fractions selected for types 5 and 7 do not agree so well. For all tracks the difference in the fractions of tracks selected is $\sim$10 %. Numerical values for the number of tracks in data and Monte Carlo and the fractions selected are shown in Table 7.2. From this table it may be seen that although the fractions selected of the statistically dominant types 1, 2 and 4 agree well, the discrepancy between data and Monte Carlo in the fraction of all tracks selected is introduced primarily by a) the fraction of type 5 tracks selected and b) the removal of all type 0 tracks. Additionally it can be seen from the numbers of all initial and final tracks in data that the mean track multiplicity for all tracks in data is initially higher than the Monte Carlo, but after track selection is lower. As the initial good track distributions in data and Monte Carlo agree well, this is indicative of excess poor quality tracks in the data compared to Monte Carlo before track selection.

QIPBTAG does not make specific use of ALEPH defined good tracks. These are defined as tracks which:

- Have at least four hits in the TPC.
- Originate from within a cylinder of radius 2 cm (the $D0$ coordinate) and length 10 cm (the $Z0$ coordinate) centred on the interaction point.

- Have $\cos\theta < 0.95$ to ensure VDET acceptance.

The cuts imposed by `QIPBTAG` to select tracks are as follows:

- All V_0 (type 3) tracks are removed.
- Tracks must have a momentum of at least 400 MeV.
- Tracks must not have a momentum greater than 40 GeV.
- Tracks must have at least four hits in the TPC.
- All type 0 tracks are removed.
- The χ^2 of the track helix fit divided by the number of degrees of freedom must be less than 6.0.
- Tracks must have $D0 < 2.0$ cm and $Z0 < 5.0$ cm. Additionally the error from the track fitting on both $D0$ and $Z0$ must be less than 5.0 cm.
- Tracks in 5^{th} momentum ordered jets and below are removed.
- The angle between a track and its jet must not be greater than 45 degrees.

The minimum number of hits required in the TPC is exactly the same as the cut used in the definition of an ALEPH good track. The $D0/Z0$ requirement is a stronger cut than that used for the good track definition, and has an additional restriction on the maximum permissible error from the track fitting on these coordinates. There is no direct overlap with respect to the good track requirement that $\cos\theta < 0.95$. However the combination of the other `QIPBTAG` cuts results in only negligible numbers of poor quality tracks being selected. Virtually all ($\sim$99.5 %) of `QIPBTAG` selected tracks therefore conform to the ALEPH good track definition.

The initial excess of poor quality tracks in data is therefore not important. However it has been shown that whilst the initial multiplicity distributions of good tracks in data and Monte Carlo agreed well, the final selected distributions did not agree so well. The `QIPBTAG` track selection therefore introduces discrepancies between the

Track Type	MC track type selection			Data track type selection			F/I
	Initial	Final	F/I	Initial	Final	F/I	ratio
Type 0	85117	-	-	100622	-	-	-
Type 1	163797	128959	0.787	153181	120101	0.784	0.996
Type 2	19713	9413	0.478	18973	9236	0.487	1.019
Type 3	-	-	-	-	-	-	-
Type 4	44873	13206	0.294	46239	13414	0.290	0.986
Type 5	32379	559	0.017	44488	561	0.013	0.765
Type 6	2293	-	-	2644	-	-	-
Type 7	2191	260	0.119	2344	374	0.160	1.345
Type 8	4018	-	-	4779	-	-	-
Type 9	6487	-	-	8140	-	-	-
All types	360868	152397	0.422	381410	143686	0.377	0.893

Table 7.2: The number of tracks before and after QIPBTAG selection and the corresponding selection fraction by track type in data and Monte Carlo for 189 - 207 GeV. Note that for clarity errors have been omitted.

fraction of good tracks selected in data and Monte Carlo. The effect of the QIPBTAG selection cuts was therefore investigated.

Figure 7.3 (a) shows the number of good tracks in data and Monte Carlo remaining after successive track selection cuts, whilst Figure 7.3 (b) shows the corresponding fraction of tracks remaining. The data over Monte Carlo ratio of the track fractions remaining after each cut is shown in Figure 7.3 (c), with the change in this ratio between successive cuts shown in Figure 7.3 (d). Table 7.3 shows the numerical values for the fraction of tracks remaining after each cut in data and Monte Carlo, along with the data over Monte Carlo ratio and the change in the ratio between cuts. It can be clearly seen from Figure 7.3 (c) and (d) that the cuts which result in the largest discrepancies between data and Monte Carlo are the momentum greater than 400 MeV cut, the type 0 cut and the $D0/Z0$ cut.

An upper limit on the systematic effect of the discrepancies in the track selection introduced by these three cuts was estimated by suppressing these cuts, thus eliminating the differences in the track selection between data and Monte Carlo. The resulting systematic errors for each energy are shown in Table 7.4.

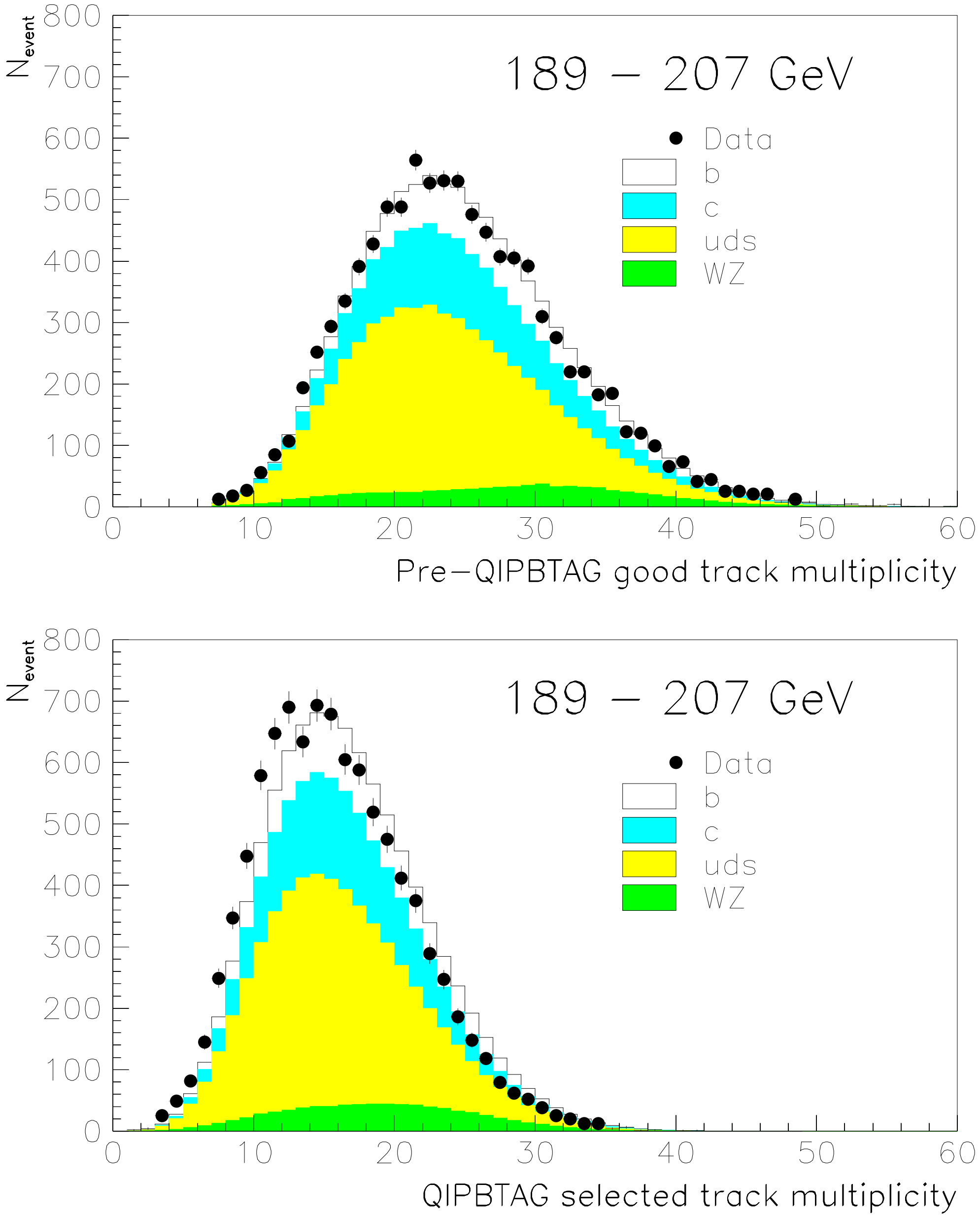

Figure 7.1: ALEPH "good" track multiplicities before `QIPBTAG` track selection (top) and `QIPBTAG` selected track multiplicities (bottom) in data and Monte Carlo for 189 - 207 GeV. The uds, c, b , W-pair and Z-pair contributions to the Monte Carlo are shown.

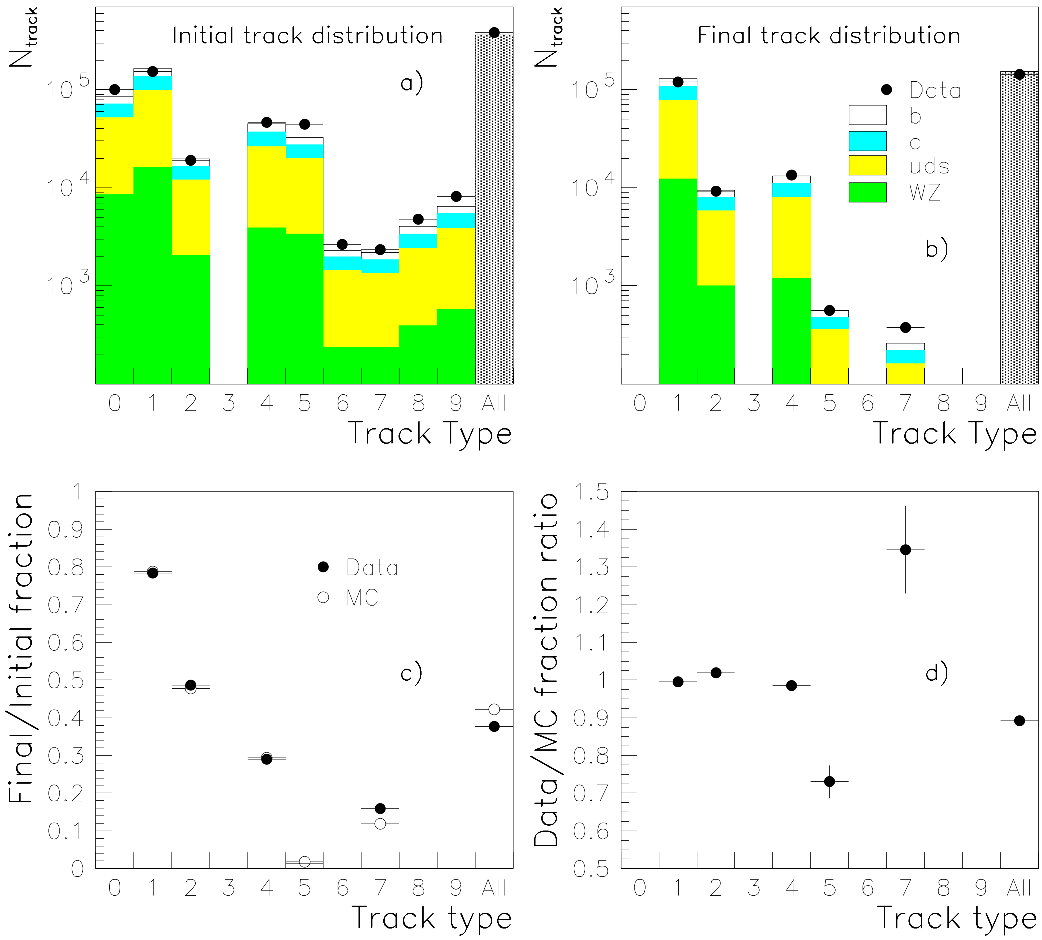

Figure 7.2: Track type distributions in data and Monte Carlo for 189 - 207 GeV before (a) and after (b) `QIPBTAG` track selection. The fraction of tracks remaining after `QIPBTAG` selection in data and Monte Carlo is shown in (c), with the data over Monte Carlo ratio of the remaining track fractions shown in (d).

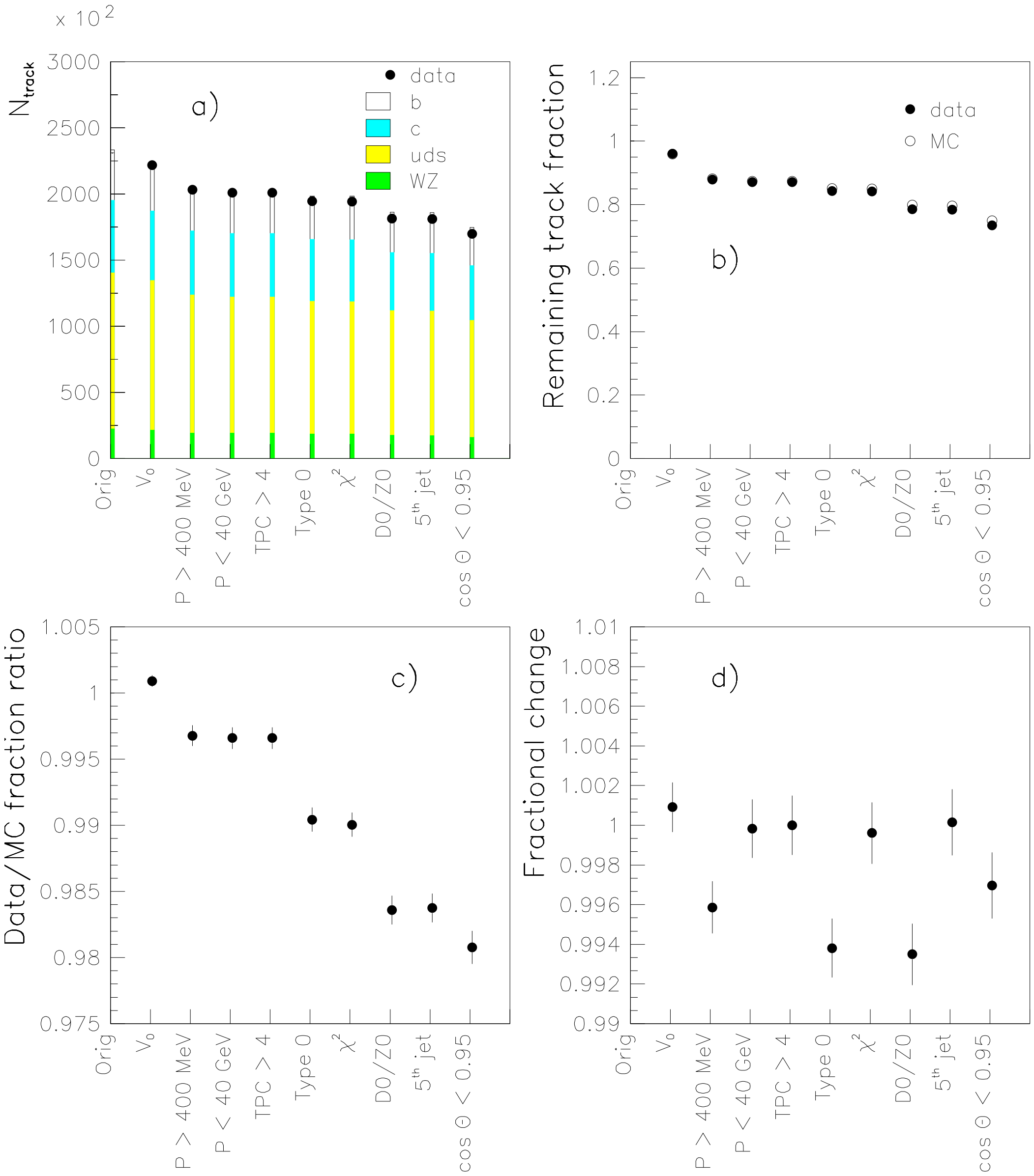

Figure 7.3: The number of tracks remaining after successive `QIPBTAG` track selection cuts (a) and the corresponding remaining fraction of tracks (b) in data and Monte Carlo for 189 - 207 GeV. The data over Monte Carlo ratio of the remaining track fractions in shown in (c), with the change in the ratio of remaining track fractions between successive cuts shown in (d).

Selection cut	Fraction kept in data	Fraction kept in MC	Data/MC ratio	Percentage change
V_0	0.9601 $\pm$ 0.0004	0.9592 $\pm$ 0.0001	1.0009 $\pm$ 0.0004	1.0009 $\pm$ 0.0013
P > 400 MeV	0.8792 $\pm$ 0.0007	0.8820 $\pm$ 0.0001	0.9968 $\pm$ 0.0008	0.9959 $\pm$ 0.0013
P < 40 GeV	0.8708 $\pm$ 0.0007	0.8738 $\pm$ 0.0001	0.9966 $\pm$ 0.0008	0.9998 $\pm$ 0.0015
TPC hits > 4	0.8708 $\pm$ 0.0007	0.8738 $\pm$ 0.0001	0.9966 $\pm$ 0.0008	1.0000 $\pm$ 0.0015
Type 0 tracks	0.8423 $\pm$ 0.0008	0.8505 $\pm$ 0.0001	0.9904 $\pm$ 0.0009	0.9938 $\pm$ 0.0015
χ^2	0.8415 $\pm$ 0.0008	0.8500 $\pm$ 0.0001	0.9900 $\pm$ 0.0009	0.9996 $\pm$ 0.0015
$D0/Z0$	0.7851 $\pm$ 0.0009	0.7982 $\pm$ 0.0002	0.9835 $\pm$ 0.0011	0.9934 $\pm$ 0.0015
5th jet tracks	0.7838 $\pm$ 0.0009	0.7967 $\pm$ 0.0002	0.9837 $\pm$ 0.0011	1.0002 $\pm$ 0.0017
$\cos\theta < 0.95$	0.7350 $\pm$ 0.0009	0.7494 $\pm$ 0.0002	0.9808 $\pm$ 0.0012	0.9970 $\pm$ 0.0017

Table 7.3: QIPBTAG track selection in data and Monte Carlo for 189 - 207 GeV.

Energy (GeV)	σ_{R_b} (p > 400 MeV)		σ_{R_b} ($D0/Z0$)		σ_{R_b} (Type 0)	
	Event tag	**Hemi tag**	**Event tag**	**Hemi tag**	**Event tag**	**Hemi tag**
189	0.00297	0.00458	0.00118	0.00035	0.00002	0.00003
192	0.00371	0.01774	0.00026	0.00049	0.00006	0.00001
196	0.00327	0.00820	0.00026	0.00275	0.00002	0.00011
200	0.00235	0.00592	0.00022	0.00052	0.00003	0.00005
202	0.00580	0.01195	0.00161	0.00044	0.00140	0.00064
205	0.00332	0.00705	0.00153	0.00133	0.00006	0.00011
207	0.00599	0.00221	0.00097	0.00155	0.00004	0.00006
189 - 207	0.00366	0.00551	0.00046	0.00049	0.00008	0.00004

Table 7.4: The systematic errors σ_{R_b} for each energy due to the QIPBTAG p > 400 MeV, $D0/Z0$ and type 0 track selection cuts.

Energy (GeV)	σ_{R_b} (Smearing parameters)	
	Event tag	**Hemi tag**
189	0.00104	0.00138
192	0.00063	0.00166
196	0.00068	0.00112
200	0.00064	0.00131
202	0.00186	0.00057
205	0.00126	0.00212
207	0.00112	0.00218
189 - 207	0.00099	0.00146

Table 7.5: The systematic errors σ_{R_b} for each energy due to the smearing parameters.

7.5 Impact parameter smearing

The smearing parameters were subject to a statistical uncertainty due to the finite statistics available in the Z^0 peak calibration data and Monte Carlo. A systematic error due to the statistical errors on the smearing parameters was evaluated for each energy by adjusting the smearing parameters by their error. The resulting errors on R_b are shown in Table 7.5.

7.6 B physics

For any measurement which involves the selection of $e^+e^- \to b\bar{b}$ events the B modelling in data and Monte Carlo must agree well. It was therefore important that the physics of B production and decay was well reproduced in the Monte Carlo.

Secondary vertex impact parameter magnitudes are a function of the B lifetime and the number of impact parameters a function of the B decay multiplicity. Additionally each B species has its own mean lifetime and multiplicity. It was therefore important for good b-tagging in the Monte Carlo that the lifetimes, multiplicities and B production rates were well modelled.

7.6.1 The B lifetime

The current measured values for the mean lifetimes of the different B species were used as input parameters in the Monte Carlo. From Figure 7.4 a) it may be seen

Species	τ ($s \times 10^{-12}$)	$\Delta\tau$ ($s \times 10^{-12}$)
$B^{\pm}$	1.653	0.028
B_0	1.548	0.032
$B_{\rm s}$	1.493	0.062
Other	1.229	0.080
Mean	1.576	0.016

Table 7.6: The current measured values for the B mean lifetimes and their errors. Taken from reference [8].

that there is a good agreement between the B mean lifetime for all B species in the Monte Carlo and the measured values shown in Table 7.6. However the error on these lifetime measurements means that the B decay times in the Monte Carlo may not be modelled correctly. In order to estimate the resulting uncertainty on R_b, each B hadron in the Monte Carlo was assigned a weight as follows.

The number $N_\tau(t)$ of unstable (decaying) particles with mean lifetime τ decaying at time t is described by the well known exponential decay law:

$$N_\tau(t) \propto e^{-t/\tau} \quad . \tag{7.2}$$

If the mean lifetime is changed by its error $\Delta\tau$ then the number of particles decaying at time t changes by a factor W_τ

$$W_\tau \;=\; \frac{N_{\tau+\Delta\tau}(t)}{N_\tau(t)} \;=\; \frac{e^{-t/(\tau+\Delta\tau)}}{e^{-t/\tau}} \tag{7.3}$$

where $N_{\tau+\Delta\tau}(t)$ and $N_\tau(t)$ are the number of particles decaying at time t with mean lifetimes $\tau+\Delta\tau$ and τ respectively. This factor W_τ was therefore the weight applied to each B hadron in the Monte Carlo. The weight for a hemisphere or event was then taken as the product of the weights for each of the B hadrons in that event or hemisphere. The B lifetime event weight distribution for all 189 - 207 GeV Monte Carlo is shown in Figure 7.4 (b). The resulting systematic errors are shown in Table 7.7.

7.6.2 The B multiplicity

Unlike the B lifetime the current measurements for the mean B decay multiplicities were not used as input parameters in the Monte Carlo. Any discrepancies between

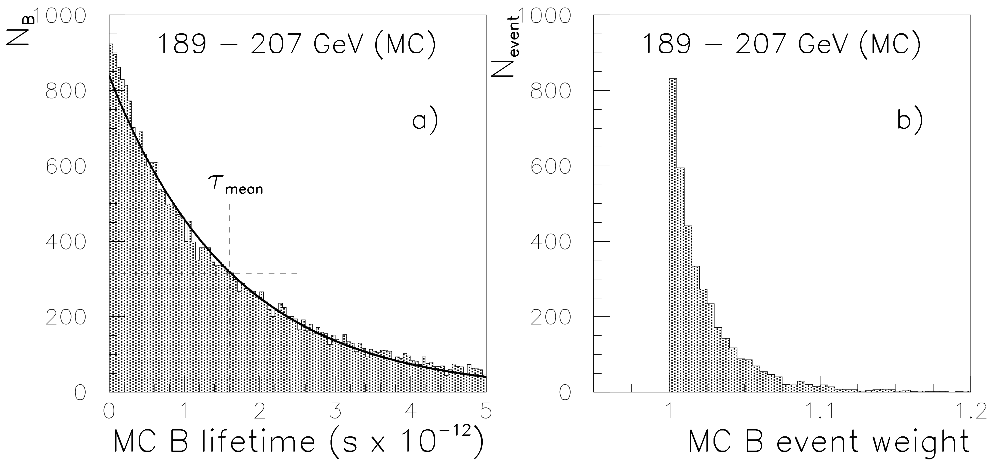

Figure 7.4: The B decay times in 189 - 207 GeV Monte Carlo for all B species (a), and the resulting B lifetime event weights for all B species (b).

Energy (GeV)	σ_{R_b} (B lifetime)	
	Event tag	**Hemi tag**
189	0.00022	0.00003
192	0.00019	0.00006
196	0.00019	0.00001
200	0.00019	0.00001
202	0.00014	0.00002
205	0.00017	0.00002
207	0.00013	0.00002
189 - 207	0.00018	0.00001

Table 7.7: The systematic errors σ_{R_b} for each energy due to the B lifetime.

the decay multiplicity distributions in data and Monte Carlo will therefore lead to a systematic uncertainty on R_b. The B decay multiplicity distribution may be approximated by a Gaussian function, so that the number of B decays $N(\beta)$ with mean multiplicity μ decaying with multiplicity β is given by:

$$N(\beta) \;\propto\; e^{(\beta-\mu)^2/2\sigma^2} \tag{7.4}$$

where σ is the root mean square (rms) width of the multiplicity distribution. Figure 7.5 (a) shows the multiplicity distribution for all B species in 189 - 207 GeV Monte Carlo and the resulting Gaussian approximation. If for a given B species the mean decay multiplicity in data is $\mu_{\rm data}$ and the mean multiplicity in Monte Carlo is μ_{MC}, then the weight W_β for each B decay with multiplicity β is:

$$W_\beta \;=\; \frac{N_{\rm data}(\beta)}{N_{\rm MC}(\beta)} \;=\; \frac{e^{(\beta-\mu_{\rm data})^2/2\sigma^2_{\rm MC}}}{e^{(\beta-\mu_{\rm MC})^2/2\sigma^2_{\rm MC}}} \tag{7.5}$$

where $N_{\rm data}(\beta)$ and $N_{\rm MC}(\beta)$ are the number of B hadrons decaying with multiplicity β in data and Monte Carlo respectively. It should be noted that as no measurement for the rms width of the B decay multiplicity has been made, the value for the rms width in data is approximated with the width from the Monte Carlo. Currently there are also no reliable measurements of the mean decay multiplicities for separate B species, only a single measurement for all species. The values for the mean decay multiplicities in data for each of the B species were therefore estimated as:

$$\mu^{\rm s}_{\rm data} \;\simeq\; \mu^{\rm s}_{\rm MC} + \Delta\mu^{\rm all} \tag{7.6}$$

where $\mu^{\rm s}_{\rm data}$ is the estimated mean decay multiplicity in data for species s, $\mu^{\rm s}_{\rm MC}$ is the mean multiplicity in Monte Carlo for species s and $\Delta\mu^{\rm all}$ is defined as:

$$\Delta\mu^{\rm all} \;=\; \mu^{\rm all}_{\rm data} - \mu^{\rm all}_{\rm MC} \tag{7.7}$$

where $\mu^{\rm all}_{\rm data}$ is the current measured value of the mean multiplicity for all B hadrons and $\mu^{\rm all}_{\rm MC}$ the mean multiplicity for all B hadrons in Monte Carlo. The value of the measured mean multiplicity for all B hadrons $\mu^{\rm all}_{\rm data}$ was taken as 4.955 ± 0.062 from reference [52]. The root mean square values for the data distributions were taken to be the same as the rms values $\sigma_{\rm MC}$ for the Monte Carlo distributions.

Energy (GeV)	σ_{R_b} (B multiplicity)	
	Event tag	**Hemi tag**
189	0.00055	0.00002
192	0.00051	0.00008
196	0.00055	0.00003
200	0.00080	0.00003
202	0.00062	0.00002
205	0.00048	0.00002
207	0.00054	0.00004
189 - 207	0.00059	0.00002

Table 7.8: The systematic errors σ_{R_b} for each energy due to the B multiplicity.

The weight for a hemisphere or event was then taken as the product of the weights of all the B decays in that event or hemisphere. The B multiplicity event weight distribution for all B hadrons in 189 - 207 GeV Monte Carlo is shown in Figure 7.5 (b). The resulting systematic errors are shown in Table 7.8.

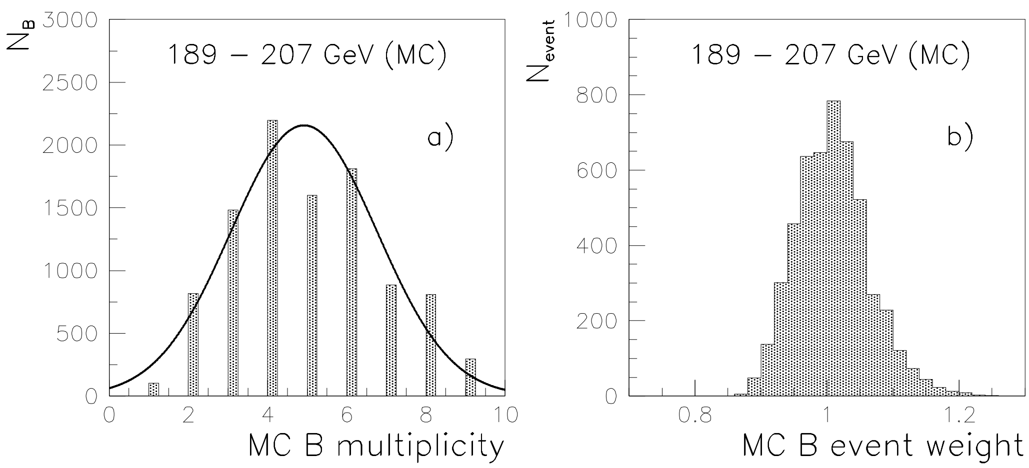

Figure 7.5: The B multiplicity distribution in 189 - 207 GeV Monte Carlo for all B species (a), and the resulting B multiplicity event weights for all B species (b).

7.6.3 The B production fractions

Different B species have different mean decay multiplicities and lifetimes, introducing a systematic uncertainty if the production fractions of the different B species in

Monte Carlo do not match those in data. The numbers of the different B species present in 189 - 207 GeV Monte Carlo (normalised to 10,000 events) are shown in Figure 7.6. The corresponding production fractions and the current measured values are shown in Table 7.9. The Monte Carlo production fractions agree with the measured values to within two sigma. Therefore for simplicity the weights applied to each B hadron in the Monte Carlo corresponded to the errors on the measured production fractions. The resulting systematic errors for $B^{\pm}$ and B_0 production are shown in Table 7.10. The systematic errors for B_s production and all other B species production are shown in Table 7.11.

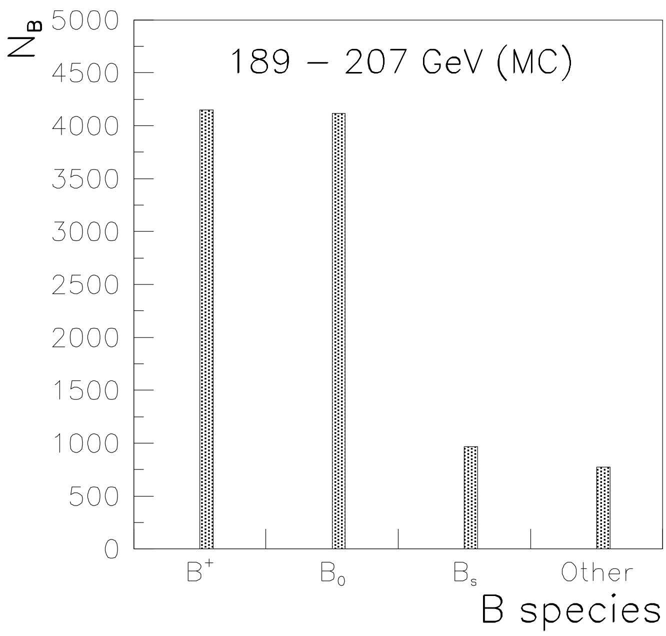

Figure 7.6: B species production in 189 - 207 GeV Monte Carlo, normalised to 10,000 events.

7.7 Jet rates

It was considered possible that the tagging of events and hemispheres may have been dependent on the number of jets clustered (jet topology). If the jet topologies in data and Monte Carlo did not match, then this would introduce a source of

Species	N_B^{MC}	f_B^{MC} (%)	f_B^{data} (%)
$B^{\pm}$	281764	40.9	38.9 ± 1.3
B_0	279622	40.6	38.9 ± 1.3
B_s	67550	9.8	10.7 ± 1.4
Other	59893	8.7	11.6 ± 2.0

Table 7.9: B production fractions in 189 - 207 GeV Monte Carlo and the current measured values, taken from reference [8]. The statistical errors on the Monte Carlo fractions are negligible.

Energy (GeV)	σ_{R_b} ($B^{\pm}$ production)		σ_{R_b} (B_0 production)	
	Event tag	**Hemi tag**	**Event tag**	**Hemi tag**
189	0.00003	0.00000	0.00001	0.00000
192	0.00003	0.00003	0.00000	0.00002
196	0.00002	0.00002	0.00001	0.00002
200	0.00004	0.00005	0.00000	0.00000
202	0.00001	0.00000	0.00002	0.00001
205	0.00002	0.00004	0.00001	0.00006
207	0.00001	0.00001	0.00001	0.00001
189 - 207	0.00002	0.00001	0.00001	0.00002

Table 7.10: The systematic errors σ_{R_b} for each energy due to the $B^{\pm}$ and B_0 production fractions.

Energy (GeV)	σ_{R_b} (B_s production)		σ_{R_b} (B_{other} production)	
	Event tag	**Hemi tag**	**Event tag**	**Hemi tag**
189	0.00005	0.00003	0.00016	0.00005
192	0.00000	0.00006	0.00013	0.00010
196	0.00001	0.00007	0.00016	0.00003
200	0.00002	0.00011	0.00018	0.00001
202	0.00003	0.00000	0.00009	0.00002
205	0.00002	0.00000	0.00011	0.00001
207	0.00002	0.00000	0.00012	0.00001
189 - 207	0.00001	0.00003	0.00014	0.00001

Table 7.11: The systematic errors σ_{R_b} for each energy due to the B_s and B_{other} production fractions.

systematic error. The tagging of events with two, three and four jets in data and Monte was therefore investigated, along with a comparison of the jet topologies.

In Figure 7.7 it may be seen that the jet topologies for all preselected events in 189 - 207 GeV data and Monte Carlo agree well. Additionally it can also be seen that the fraction of two, three and four jet events as a function of the event tag in both data and Monte Carlo agree well, to within one sigma on the statistical error. Therefore it is not important if the tagging is dependent on the number of jets clustered. However the flatness of the plots demonstrates that the tagging is in fact independent of the number of jets.

Due to the good agreement between the jet topologies in data and Monte Carlo, it was therefore unnecessary to include any systematic error on R_b.

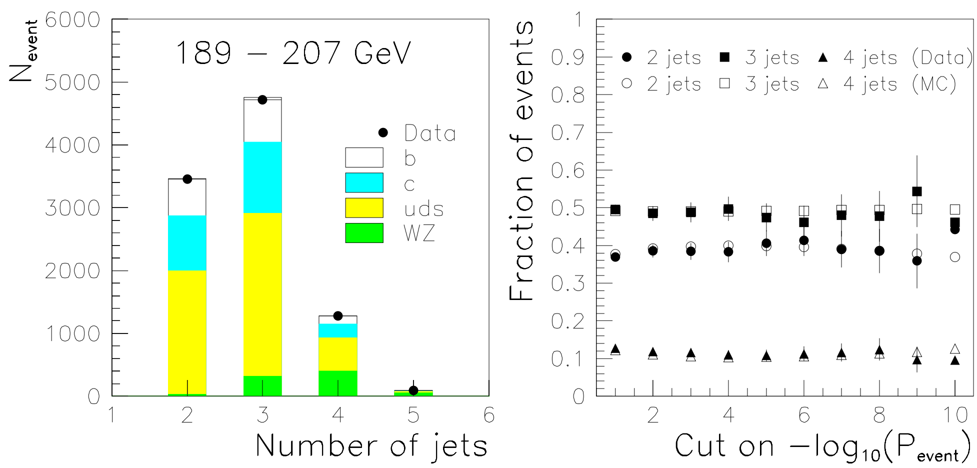

Figure 7.7: The jet clustering distributions for all preselected events in 189 - 207 GeV data and Monte Carlo (left) and the fraction of two, three and four jet events as a function of the event tag (right).

7.8 Hadronic background modelling

The measurement of R_b is dependent on accurate modelling of the *uds* and *c* backgrounds in the Monte Carlo. A peak in the measurement of R_b using Z calibration data for low cut values with the event tag indicated that the backgrounds in Monte Carlo may not accurately reproduce the data. This was one of the motivations for smearing the impact parameters. This hypothesis was supported by the discrepancies between the B efficiencies measured in data (which is a function of the Monte Carlo estimated backgrounds) and Monte Carlo using the hemisphere tag for low cut values.

7.8.1 Non-radiative hadronic background

The uncertainty on the uds and c backgrounds was estimated using the hemisphere tag, by adjusting the uds and c efficiencies for each hemisphere cut value so that the B hemisphere efficiencies in data and Monte Carlo matched. For each selection cut on the b-tag the uds and c efficiencies were varied by ± 100 % in 1 % increments, resulting in a total of 200×200 different efficiency combinations. The value for the B efficiency in data was calculated for each uds and c efficiency combination, and the result compared to the Monte Carlo estimated B efficiency.

As the efficiencies were incremented in finite steps of 1 %, an exact match in the B efficiencies was generally not seen. A B efficiency match was therefore defined as the combination of uds and c efficiencies which immediately preceded a change in the sign of the difference between the two B efficiencies, or when the two B efficiencies agreed to within 0.5 %. These criteria resulted in multiple possible combinations of the uds and c efficiencies for each cut. A single combination was then selected by choosing the combination which minimised the change to both the uds and c efficiencies.

It is extremely difficult to convert a hemisphere uncertainty for a given cut value to an equivalent event uncertainty. The hemisphere uncertainties obtained were therefore used to put an approximate *upper* limit on the uds and c background uncertainties for both event and hemisphere tags. For the region between a hemisphere selection cut of 1.5 and 3.5, where statistics are maximised, the change required for both the uds and c efficiencies was found to be $\sim$11 %. This uncertainty was therefore applied to both the uds and c efficiencies estimated from Monte Carlo for both

Energy (GeV)	σ_{R_b} (uds background)		σ_{R_b} (c background)	
	Event tag	**Hemi tag**	**Event tag**	**Hemi tag**
189	0.00063	0.00008	0.00236	0.00202
192	0.00062	0.00012	0.00231	0.00316
196	0.00065	0.00008	0.00236	0.00214
200	0.00068	0.00008	0.00235	0.00230
202	0.00064	0.00007	0.00214	0.00216
205	0.00068	0.00008	0.00228	0.00246
207	0.00067	0.00008	0.00222	0.00250
189 - 207	0.00065	0.00008	0.00230	0.00224

Table 7.12: The systematic errors σ_{R_b} for each energy due to the uds and c backgrounds.

Energy (GeV)	σ_{R_b} (Radiative background)	
	Event tag	**Hemi tag**
189	0.00266	0.00128
192	0.00251	0.00176
196	0.00255	0.00128
200	0.00265	0.00129
202	0.00213	0.00122
205	0.00223	0.00133
207	0.00230	0.00130
189 - 207	0.00247	0.00129

Table 7.13: The systematic errors σ_{R_b} for each energy due to radiative background.

the event and hemisphere tags for all cut values. The resulting systematic errors on R_b for all energies are shown in Table 7.12.

7.8.2 Radiative hadronic background

Due to the small radiative background content it was difficult to ascertain how well modelled the radiative background was in Monte Carlo. A systematic error on R_b was estimated by varying this background by $\pm$ 50 %. The resulting errors are shown in Table 7.13.

7.9 Standard Model cross-sections

The values for the hadronic, W^+W^- and Z^0Z^0 cross-sections in the Standard Model are subject to a theoretical error. This therefore leads to an uncertainty on the

Energy (GeV)	σ_{R_b}(Hadronic cross-section)		σ_{R_b}(WW/ZZ cross-section)	
	Event tag	**Hemi tag**	**Event tag**	**Hemi tag**
189	0.00009	0.00002	0.00032	0.00016
192	0.00009	0.00004	0.00031	0.00021
196	0.00009	0.00002	0.00033	0.00016
200	0.00009	0.00003	0.00036	0.00021
202	0.00008	0.00004	0.00028	0.00011
205	0.00009	0.00003	0.00029	0.00014
207	0.00009	0.00004	0.00032	0.00021
189 - 207	0.00009	0.00002	0.00032	0.00017

Table 7.14: The systematic errors σ_{R_b} for each energy due to the hadronic and W^+W^-/Z^0Z^0 theoretical cross-sections.

efficiencies and backgrounds estimated from Monte Carlo. Values for the theoretical errors were taken from [53], which quotes the hadronic cross-section error to be 0.26 %, with W^+W^- and Z^0Z^0 cross-section errors of ~2 %. The systematic uncertainty on R_b was evaluated by adjusting the cross-sections by their errors. The resulting systematic errors are shown in Table 7.14.

7.10 Electromagnetic calorimeter calibration

An additional systematic error on R_b arises from uncertainties in the calibration of the electromagnetic calorimeter. Studies of the calorimeter energy scale calibration [54] put the resulting uncertainty on the event preselection at ~1.0 %. The event preselection in the Monte Carlo was therefore adjusted by this amount in order to evaluate the uncertainty on R_b, resulting in the systematic errors listed in Table 7.15.

7.11 Monte Carlo statistics

The backgrounds estimated from Monte Carlo were subject to a statistical error due to the finite Monte Carlo statistics available. The resulting Monte Carlo statistical errors on R_b are listed in Table 7.16.

Energy (GeV)	σ_{R_b} (ECAL calibration)	
	Event tag	**Hemi tag**
189	0.00040	0.00003
192	0.00040	0.00007
196	0.00041	0.00004
200	0.00041	0.00004
202	0.00037	0.00008
205	0.00039	0.00002
207	0.00039	0.00002
189 - 207	0.00040	0.00003

Table 7.15: The systematic errors σ_{R_b} for each energy due to the ECAL energy scale calibration.

Energy (GeV)	σ_{R_b} (Monte Carlo statistics)	
	Event tag	**Hemi tag**
189	0.00074	0.00047
192	0.00070	0.00077
196	0.00072	0.00049
200	0.00081	0.00053
202	0.00071	0.00051
205	0.00082	0.00071
207	0.00073	0.00060
189 - 207	0.00028	0.00020

Table 7.16: The systematic errors σ_{R_b} for each energy due to Monte Carlo statistics.

Energy (GeV)	Luminosity (pb^{-1})	Luminosity Errors (pb^{-1})			
		Stat.	Theo.	Syst.	Total
189	174.209	0.202	0.213	0.706	0.765
192	28.931	0.083	0.035	0.113	0.145
196	79.857	0.141	0.097	0.312	0.356
200	86.277	0.150	0.105	0.337	0.384
202	41.893	0.106	0.051	0.164	0.202
205	81.644	0.149	0.100	0.337	0.382
207	133.654	0.193	0.163	0.552	0.607

Table 7.17: Data integrated luminosities and the statistical, theoretical and systematic errors for each energy.

Energy (GeV)	σ_{R_b} (Luminosity)	
	Event tag	Hemi tag
189	0.00022	0.00000
192	0.00022	0.00001
196	0.00023	0.00000
200	0.00023	0.00001
202	0.00020	0.00003
205	0.00021	0.00001
207	0.00021	0.00001
189 - 207	0.00022	0.00000

Table 7.18: The systematic errors σ_{R_b} for each energy due to the integrated luminosity.

7.12 The data integrated luminosity

The total data integrated luminosities recorded for each energy are subject to statistical, systematic and theoretical errors. These errors are shown in Table 7.17. As the Monte Carlo is normalised according to the integrated luminosity, these errors result in a systematic uncertainty on R_b. A single systematic error was evaluated for each energy by adjusting the integrated luminosities by their total error. The resulting errors are shown in Table 7.18.

7.13 The hemisphere tagging correlation coefficient

The probability of tagging both hemispheres in an event is not exactly the square of the probability of tagging one hemisphere as discussed in Section 4.6.7. In order to

Energy (GeV)	ρ
189	1.00422
192	0.99727
196	1.00271
200	1.00355
202	0.99748
205	0.99760
207	0.99740
189 - 207	1.00031

Table 7.19: The B hemisphere tagging correlation coefficients, ρ, from Monte Carlo for each energy.

Energy (GeV)	σ_{R_b} (Hemi tag correlation)	
	Event tag	**Hemi tag**
189		0.00081
192		0.00068
196		0.00086
200	NA	0.00087
202		0.00079
205		0.00055
207		0.00108
189 - 207		0.00027

Table 7.20: The systematic errors σ_{R_b} for each energy due to the hemisphere tagging correlation coefficient. Note this error is not applicable for the event tag.

account for this the hemisphere tagging correlation coefficient ρ is estimated from B Monte Carlo. The values found for ρ at each energy are listed in Table 7.19. As it was not clear how well the B event and hemisphere efficiencies were modelled in the Monte Carlo, a systematic on R_b was evaluated by setting $\rho = 1$. The resulting systematic errors for each energy are shown in Table 7.20.

7.14 Total systematic errors

All the systematic errors were assumed to be independent. The total systematic error for each energy was therefore obtained by adding all the individual systematic errors in quadrature. All the systematic errors evaluated for each energy and their totals are shown in Tables 7.21 and 7.22 for the event and hemisphere tags respectively.

Systematic (Event tag)	189	192	196	200	202	205	207	189 - 207
y_{cut} ± **50 %**	0.00366	0.00523	0.00155	0.00666	0.00853	0.00840	0.00450	0.00319
`QIPBTAG` **track selection**								
p > 400 MeV	0.00297	0.00371	0.00327	0.00235	0.00580	0.00332	0.00599	0.00366
$D0/Z0$	0.00118	0.00026	0.00026	0.00022	0.00161	0.00153	0.00097	0.00046
Type 0	0.00002	0.00006	0.00002	0.00003	0.00140	0.00006	0.00004	0.00008
B **physics**								
B lifetime	0.00022	0.00019	0.00019	0.00019	0.00014	0.00017	0.00013	0.00018
B multiplicity	0.00055	0.00051	0.00055	0.00080	0.00062	0.00048	0.00054	0.00059
$B^{\pm}$ production	0.00003	0.00003	0.00002	0.00004	0.00001	0.00002	0.00001	0.00002
B_0 production	0.00001	0.00000	0.00001	0.00000	0.00002	0.00001	0.00001	0.00001
B_{s} production	0.00005	0.00000	0.00001	0.00002	0.00003	0.00002	0.00002	0.00001
Other production	0.00016	0.00013	0.00016	0.00018	0.00009	0.00011	0.00012	0.00014
Background modelling								
uds content	0.00063	0.00062	0.00065	0.00068	0.00064	0.00068	0.00067	0.00065
c content	0.00236	0.00231	0.00236	0.00235	0.00214	0.00228	0.00222	0.00230
Radiative hadronic	0.00266	0.00251	0.00255	0.00265	0.00213	0.00223	0.00230	0.00247
SM cross-sections								
Hadronic	0.00009	0.00009	0.00009	0.00009	0.00008	0.00009	0.00009	0.00009
W^+W^-/Z^0Z^0	0.00032	0.00031	0.00033	0.00036	0.00028	0.00029	0.00032	0.00032
ECAL calibration	0.00040	0.00040	0.00041	0.00041	0.00037	0.00039	0.00039	0.00040
MC statistics	0.00074	0.00070	0.00072	0.00081	0.00071	0.00082	0.00073	0.00028
Smearing parameters	0.00104	0.00063	0.00068	0.00064	0.00186	0.00126	0.00112	0.00099
Luminosity	0.00022	0.00022	0.00023	0.00023	0.00020	0.00021	0.00021	0.00022
Total	0.00624	0.00739	0.00523	0.00806	0.01118	0.00986	0.00838	0.00611

Table 7.21: All evaluated systematic errors and their totals for each energy with the event tag.

Systematic (Hemisphere tag)	189	192	196	200	202	205	207	189 - 207
y_{cut} ± **50 %**	0.00424	0.02212	0.00434	0.00633	0.01216	0.00840	0.00654	0.00289
`QIPBTAG` **track selection**								
p > 400 MeV	0.00458	0.01774	0.00820	0.00592	0.01195	0.00705	0.00221	0.00551
$D0/Z0$	0.00035	0.00049	0.00275	0.00052	0.00044	0.00133	0.00155	0.00049
Type 0	0.00003	0.00001	0.00011	0.00005	0.00064	0.00011	0.00006	0.00004
B **physics**								
B lifetime	0.00003	0.00006	0.00001	0.00001	0.00002	0.00002	0.00002	0.00001
B multiplicity	0.00002	0.00008	0.00003	0.00003	0.00002	0.00002	0.00004	0.00002
$B^{\pm}$ production	0.00000	0.00003	0.00002	0.00005	0.00000	0.00004	0.00001	0.00001
B_0 production	0.00000	0.00002	0.00002	0.00000	0.00001	0.00006	0.00001	0.00002
B_{s} production	0.00003	0.00006	0.00007	0.00011	0.00000	0.00000	0.00000	0.00003
Other production	0.00005	0.00010	0.00003	0.00001	0.00002	0.00001	0.00001	0.00001
Background modelling								
uds content	0.00008	0.00012	0.00008	0.00008	0.00007	0.00008	0.00008	0.00008
c content	0.00202	0.00316	0.00214	0.00230	0.00216	0.00246	0.00250	0.00224
Radiative hadronic	0.00128	0.00176	0.00128	0.00129	0.00122	0.00133	0.00130	0.00129
SM cross-sections								
Hadronic	0.00002	0.00004	0.00002	0.00003	0.00004	0.00003	0.00004	0.00002
W^+W^-/Z^0Z^0	0.00016	0.00021	0.00016	0.00021	0.00011	0.00014	0.00021	0.00017
ECAL calibration	0.00003	0.00007	0.00004	0.00004	0.00008	0.00002	0.00002	0.00003
MC statistics	0.00047	0.00077	0.00049	0.00053	0.00051	0.00071	0.00060	0.00020
Smearing parameters	0.00138	0.00166	0.00112	0.00131	0.00057	0.00212	0.00218	0.00146
Luminosity	0.00000	0.00001	0.00000	0.00001	0.00003	0.00001	0.00001	0.00000
Hemisphere tag correlation	0.00081	0.00068	0.00086	0.00087	0.00079	0.00055	0.00108	0.00027
Total	0.00690	0.02866	0.01011	0.00923	0.01729	0.01163	0.00802	0.00692

Table 7.22: All evaluated systematic errors and their totals for each energy with the hemisphere tag.

Chapter 8

The calibrated event tag and final results

8.1 Introduction

Previous ALEPH measurements of R_b at LEP2 have all been made with the event tag due to low statistics. In order to be compatible with previously published results, it was desirable to use the same tag. However the hemisphere tag technique is a much more reliable method as the B selection efficiency is measured from data.

Due to an observed discrepancy between the B selection efficiencies in data and Monte Carlo, the hemisphere tag was used to calibrate the event tag. In this chapter the calibration of the event tag is described, followed by the evaluation of the statistical and systematic errors on the calibrated results. The final calibrated results for all energies between 189 and 207 GeV are then presented.

8.2 The B hemisphere selection efficiency at LEP2

Studies at the Z^0 peak showed that the B efficiency modelling in Monte Carlo agreed to within $\sim$0.5 % of the data and one sigma of the statistical error for regions of high statistics. Thus it was concluded that the B modelling in the Z^0 peak Monte Carlo was sufficiently accurate to enable a reliable measurement of R_b at the Z^0 peak with the event tag. However a much larger discrepancy was found between the

B hemisphere selection efficiencies in data and Monte Carlo at LEP2.

From Figure 6.2 it can be seen that for the region $2.0 < b$-tag < 4.0 (in which the optimum cut value is found) the B efficiencies in all 189 - 207 GeV data and Monte Carlo agree to within one sigma of the statistical error. However the discrepancy between the efficiencies is $\sim$4 %, which is nearly an order of magnitude greater than the discrepancy at the Z^0 peak. As expected this discrepancy in the efficiencies is seen to result in discrepancies between the event and hemisphere tag values for R_b, as seen in Figure 6.4.

In order to compensate for this discrepancy between the B efficiencies, the hemisphere tag was used to calibrate the event tag. This therefore enabled the reliability of the hemisphere tag to be utilised, whilst taking advantage of the higher statistical resolution afforded by the event tag.

8.3 Event tag calibration

Each event tag result is weighted by the ratio of the hemisphere and event tag results obtained for the whole data set. The calibration ratio C is therefore defined as

$$C = \frac{(R_b^{\mathrm{h}})_{\mathrm{all}}}{(R_b^{\mathrm{e}})_{\mathrm{all}}} \tag{8.1}$$

where $(R_b^{\mathrm{h}})_{\mathrm{all}}$ and $(R_b^{\mathrm{e}})_{\mathrm{all}}$ are R_b measured with the hemisphere and event tags respectively for all 189 - 207 GeV data. Each event tag result is then scaled by this factor C to produce the final values for R_b at each energy:

$$(R_b^{\mathrm{f}})_{\mathrm{i}} = (R_b^{\mathrm{e}})_{\mathrm{i}} \times C \tag{8.2}$$

where $(R_b^{\mathrm{f}})_{\mathrm{i}}$ is the final value for R_b at energy i and $(R_b^{\mathrm{e}})_{\mathrm{i}}$ is the event tag value at energy i. The errors on $(R_b^{\mathrm{h}})_{\mathrm{all}}$ and $(R_b^{\mathrm{e}})_{\mathrm{all}}$ result in an error on C, which therefore introduces an additional source of error on the final R_b values. However there is a correlation between C and $(R_b^{\mathrm{e}})_{\mathrm{i}}$ as the events used to measure $(R_b^{\mathrm{e}})_{\mathrm{i}}$ are included in C. In order to evaluate the errors on the final calibrated event tag results at each individual energy point, knowledge of this correlation is thus required.

However this is not true for the final combined result. If the event tag result for all data combined is scaled by the calibration factor:

$$(R_b^{\rm f})_{\rm all} \;=\; (R_b^{\rm e})_{\rm all} \times C \;=\; (R_b^{\rm e})_{\rm all} \times \frac{(R_b^{\rm h})_{\rm all}}{(R_b^{\rm e})_{\rm all}} \;=\; (R_b^{\rm h})_{\rm all} \tag{8.3}$$

so that by definition the calibrated event tag value of R_b for all data combined is given by the value of R_b measured with the hemisphere tag for all data combined. Additionally, as proved in Appendix B, the errors (both statistical and systematic) on the calibrated event tag value of R_b for all data combined should also be the same as those for the combined hemisphere tag value:

$$\sigma_{\rm all}^{\rm f} \;=\; \sigma_{\rm all}^{\rm h} \tag{8.4}$$

where $\sigma_{\rm all}^{\rm f}$ is the error on the calibrated event tag result for all data combined and $\sigma_{\rm all}^{\rm h}$ is the error on the hemisphere tag result for all data combined. The final result for the combined data is therefore given by the result obtained with the hemisphere tag for the combined data, and thus no knowledge of the correlation is required[1].

However for the individual energy points the correlation between C and $(R_b^{\rm e})_{\rm i}$ must be evaluated. Determining this correlation is not trivial, and thus an alternative approach was implemented.

8.4 The weighted mean

The results presented in Chapter 6 for all 189 - 207 GeV data were evaluated by summing the selected events or hemispheres at each energy point, as described in Section 6.2. However an alternative definition for the combined value of R_b is given by the weighted mean of the individual results at each energy. The weighted mean value for each tag is given by:

$$(R_b^{\rm e})_{\rm mean} \;=\; \sum_{\rm i=1}^{\rm i=7} \alpha_{\rm i} \times (R_b^{\rm e})_{\rm i} \;\; ; \quad \left(R_b^{\rm h}\right)_{\rm mean} \;=\; \sum_{\rm i=1}^{\rm i=7} \beta_{\rm i} \times \left(R_b^{\rm h}\right)_{\rm i} \tag{8.5}$$

[1]As shown in Appendix B, the final calibrated errors for the combined data are equal to those obtained with the hemisphere tag because the correlations cancel.

Tag	Combined R_b	Mean R_b
Event	0.14236 ± 0.00564	0.14217 ± 0.00563
Hemisphere	0.15138 ± 0.01200	0.15056 ± 0.01195

Table 8.1: The weighted mean and original combined values of R_b plus their statistical errors measured with the event and hemisphere tags.

where the contributions of each individual result for the event tag, α_i, and for the hemisphere tag, β_i, are inversely proportional to the square of their statistical errors:

$$\alpha_{\mathrm{i}} \;=\; \left(\sigma^2_{x_{\mathrm{i}}} \sum_{\mathrm{i}=1}^{\mathrm{i}=7} \frac{1}{\sigma^2_{x_{\mathrm{i}}}}\right)^{-1} \quad ; \quad \beta_{\mathrm{i}} \;=\; \left(\sigma^2_{y_{\mathrm{i}}} \sum_{\mathrm{i}=1}^{\mathrm{i}=7} \frac{1}{\sigma^2_{y_{\mathrm{i}}}}\right)^{-1} \tag{8.6}$$

where $\sigma_{x_{\mathrm{i}}}$ and $\sigma_{y_{\mathrm{i}}}$ are the statistical errors at energy i on the event and hemisphere tag results respectively. Similarly to Equation 8.5, the statistical errors on the weighted mean values are given by

$$(\sigma_x)_{\mathrm{mean}} \;=\; \sum_{\mathrm{i}=1}^{\mathrm{i}=7} \alpha_{\mathrm{i}} \times \sigma_{x_i} \;;\quad (\sigma_y)_{\mathrm{mean}} \;=\; \sum_{\mathrm{i}=1}^{\mathrm{i}=7} \beta_{\mathrm{i}} \times \sigma_{y_i} \quad . \tag{8.7}$$

This method for evaluating a combined result should yield very similar values to those obtained with the original method of summing the selected events or hemispheres at each energy, and then evaluating R_b. The weighted mean values, the original combined values and their statistical errors for both tags are shown in Table 8.1, where it can be seen that the results for the two methods are indeed very similar.

The motivation for using the weighted mean is that this definition for the combined R_b value allows the evaluation of the statistical errors on the final calibrated values without having to evaluate a correlation between C and $(R_b^{\mathrm{e}})_{\mathrm{i}}$. The calibration factor C is now redefined as

$$C \;=\; \frac{(R_b^{\mathrm{h}})_{\mathrm{mean}}}{(R_b^{\mathrm{e}})_{\mathrm{mean}}} \tag{8.8}$$

which results in a value of $C = 1.05901$. This definition of C is then used to evaluate the statistical errors on the calibrated results as follows.

8.5 Evaluation of the statistical errors

Letting $(R_b^{\mathrm{e}})_{\mathrm{i}} = x_{\mathrm{i}}$, $\left(R_b^{\mathrm{h}}\right)_{\mathrm{i}} = y_{\mathrm{i}}$ and $\left(R_b^{\mathrm{f}}\right)_{\mathrm{i}} = R_{\mathrm{i}}$ in order to simplify the notation, then from Equations 8.2 and 8.8 the final value for R_b at energy i is given by

$$R_{\mathrm{i}} \;=\; x_{\mathrm{i}} \times \frac{(\beta_1 y_1 + ... + \beta_7 y_1)}{(\alpha_1 x_1 + ... + \alpha_7 x_7)} \tag{8.9}$$

so that R_b is simply a function of all the individual energy measurements made with both tags:

$$R_{\mathrm{i}} \;=\; R_{\mathrm{i}}\,(x_1, .., x_7, y_1, .., y_7) \quad . \tag{8.10}$$

The error on R_{i} can then be calculated from standard error propagation. The only correlations present are those between the two values of R_b measured with each tag at the same energy, as these results are based on the same data. Results at different energies are statistically completely independent of each other as they are calculated from separate data. Thus the statistical error on R_{i} is given by

$$\sigma_{R_{\mathrm{i}}}^2 \;=\; \sum_{\mathrm{i}=1}^{\mathrm{i}=7} \left[\left(\frac{\partial R_{\mathrm{i}}}{\partial x_{\mathrm{i}}}\right)^2 \sigma_{x_{\mathrm{i}}}^2 + \left(\frac{\partial R_{\mathrm{i}}}{\partial y_{\mathrm{i}}}\right)^2 \sigma_{y_{\mathrm{i}}}^2 + 2\rho_{x_{\mathrm{i}} y_{\mathrm{i}}} \left(\frac{\partial R_{\mathrm{i}}}{\partial x_{\mathrm{i}}}\right) \left(\frac{\partial R_{\mathrm{i}}}{\partial y_{\mathrm{i}}}\right) \sigma_{y_{\mathrm{i}}} \sigma_{y_{\mathrm{i}}} \right] \tag{8.11}$$

where $\rho_{x_{\mathrm{i}} y_{\mathrm{i}}}$ is the correlation at energy i between the measurements of R_b with each tag. Evaluating the statistical errors in this way therefore does not require a knowledge of the correlation between C and $(R_b^{\mathrm{e}})_{\mathrm{i}}$, but only requires knowledge of the correlation between the event and hemisphere tag results at each energy. However for this to be a valid method of calculating the statistical errors on the final calibrated values, the weighted mean values of R_b must yield very similar values to the original method of summing the selected events or hemispheres at each energy. From Table 8.1 this was seen to be the case. However, for consistency, the original definition for the combined values of R_b was discarded, and the combined value redefined as the weighted mean value.

All the quantities in Equation 8.11 are therefore known, with the exception of the correlations between the event and hemisphere tag measurements at each energy. Assuming this correlation is the same for each energy, it is expected from Equation 8.9 that the first term on the right hand side, x_{i}, will suppress the correlations between each of the $x_{\rm i}$, $y_{\rm i}$ pairs in the second term as, by definition:

$$\sum_{\rm i=1}^{\rm i=7} \alpha_{\rm i} = 1 \; ; \quad \sum_{\rm i=1}^{\rm i=7} \beta_{\rm i} = 1 \; . \tag{8.12}$$

The correlation between the event and hemisphere tag results was estimated from data, and is described in the following section.

8.6 Hemisphere and event tag correlation

The correlation between R_b measured with the event and hemisphere tags was assumed to be the same for each energy. Thus the correlation was calculated from the two sets of results obtained with each tag. The correlation ρ between two data sets x and y is defined as

$$\rho = \frac{\mathrm{cov(x,y)}}{\sigma_x \sigma_y} = \frac{\overline{x.y} - \overline{x}.\overline{y}}{\sigma_x \sigma_y} \tag{8.13}$$

where σ_x (σ_y) is the standard deviation on x (y), defined as:

$$\sigma_x = \sqrt{\overline{x^2} - \overline{x}^2} \tag{8.14}$$

which results in a correlation coefficient of $\rho = 0.48$ for the two sets of R_b results. The two sets of results obtained with the event and hemisphere tags are therefore reasonably well positively correlated. A scatter plot of the results is shown in Figure 8.1. Having found the correlation coefficient the final statistical errors may then be calculated according to Equation 8.11.

The statistical errors on the final calibrated values for R_b were evaluated at each energy and for the weighted mean value with several different values for the correlation coefficient. The results for all energies are shown in Table 8.2 for correlation coefficients of 0, 0.48 and 1. As expected the results have little dependence on the value of the correlation coefficient. Additionally the result for the weighted mean value is completely independent of the correlation. This was also expected as by definition the statistical error on the final calibrated value for R_b is given by the statistical error on the weighted mean hemisphere tag result, whatever the correlation between the event and hemisphere tag results. The statistical errors obtained with a correlation coefficient of 0.48 were then taken as the final statistical errors.

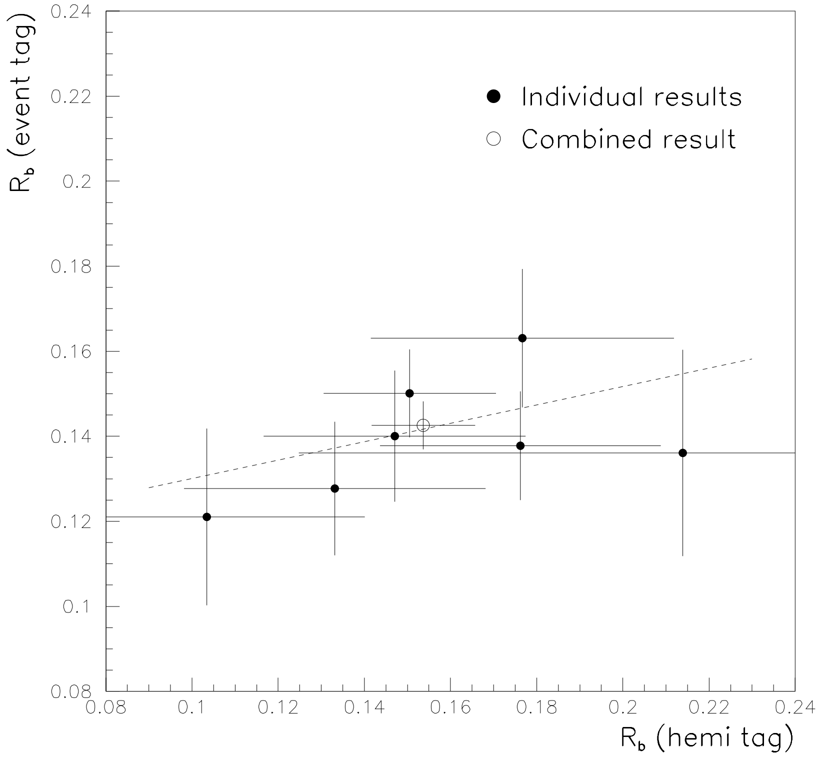

Figure 8.1: Scatter plot of R_b measured with an event tag versus a hemisphere tag for all 189 - 207 GeV energies. The combined data point is also shown; however this was not included in the calculation of the correlation between the two sets of results and the best fit line shown.

Energy (GeV)	σ_{R_b} (Statistical error)		
	$\rho = 0$	$\rho = 0.48$	$\rho = 1$
189	0.01560	0.01571	0.01583
192	0.02752	0.02708	0.02660
196	0.01921	0.01938	0.01957
200	0.02119	0.02089	0.02057
202	0.02353	0.02397	0.02444
205	0.01888	0.01898	0.01909
207	0.01680	0.01655	0.01628
189 - 207	0.01195	0.01195	0.01195

Table 8.2: The statistical errors on the final calibrated event tag measurements for three different correlations between the event and hemisphere tag results.

8.7 Evaluation of the systematic errors

Although the evaluation of some of the systematic errors depends on the available statistics, there is no reason why any of the systematic uncertainties should vary significantly between each energy point at which R_b has been measured. The value of each of the systematic errors evaluated for the whole 189 - 207 GeV data set therefore represents the best estimation of each systematic uncertainty for both tags.

The systematic errors were assumed to be independent of energy, so that the fractional systematic errors at each energy point are equal to the fractional systematic errors for the combined data set:

$$\frac{\sigma_{\mathrm{i}}^{\mathrm{f}}}{\left(R_b^{\mathrm{f}}\right)_{\mathrm{i}}} = \frac{\sigma_{\mathrm{all}}^{\mathrm{f}}}{\left(R_b^{\mathrm{f}}\right)_{\mathrm{all}}} = \frac{\sigma_{\mathrm{all}}^{\mathrm{h}}}{\left(R_b^{\mathrm{h}}\right)_{\mathrm{all}}} \tag{8.15}$$

so that

$$\sigma_{\mathrm{i}}^{\mathrm{f}} = \left(R_b^{\mathrm{f}}\right)_{\mathrm{i}} \times \frac{\sigma_{\mathrm{all}}^{\mathrm{h}}}{\left(R_b^{\mathrm{h}}\right)_{\mathrm{all}}} \tag{8.16}$$

where $\sigma_{\mathrm{i}}^{\mathrm{f}}$ is the systematic error at energy i on the calibrated event tag value of R_b. The systematic errors on the hemisphere tag weighted mean result were taken to be those evaluated with the original summed data sample. Equation 8.16 therefore becomes:

$$\sigma_{\mathrm{i}}^{\mathrm{f}} = \left(R_b^{\mathrm{f}}\right)_{\mathrm{i}} \times \frac{\sigma_{\mathrm{all}}^{\mathrm{h}}}{\left(R_b^{\mathrm{h}}\right)_{\mathrm{mean}}} \tag{8.17}$$

which was used to calculate values for all the systematic errors considered in Chapter 7 for each calibrated event tag result. The final systematic errors on the calibrated event tag results are listed in Table 8.3.

8.8 Final results for R_b at 189 - 207 GeV

The final values for R_b were obtained by weighting the event tag results by the calibration factor C as described in Section 8.3. The combined R_b values for the whole 189 - 207 GeV data set were taken to be the weighted mean values. The statistical and systematic errors were evaluated as described in Sections 8.5 and 8.7.

Systematic (Hemisphere tag)	189	192	196	200	202	205	207	189 - 207
y_{cut} **± 50 %**	0.00305	0.00277	0.00285	0.00332	0.00246	0.00260	0.00280	0.00289
`QIPBTAG` **track selection**								
p > 400 MeV	0.00582	0.00527	0.00543	0.00632	0.00469	0.00495	0.00534	0.00551
$D0/Z0$	0.00052	0.00047	0.00048	0.00056	0.00042	0.00044	0.00047	0.00049
Type 0	0.00004	0.00004	0.00004	0.00005	0.00003	0.00004	0.00004	0.00004
B **physics**								
B lifetime	0.00001	0.00001	0.00001	0.00001	0.00001	0.00001	0.00001	0.00001
B multiplicity	0.00002	0.00002	0.00002	0.00002	0.00002	0.00002	0.00002	0.00002
$B^{\pm}$ production	0.00001	0.00001	0.00001	0.00001	0.00001	0.00001	0.00001	0.00001
B_0 production	0.00002	0.00002	0.00002	0.00002	0.00002	0.00002	0.00002	0.00002
B_s production	0.00003	0.00003	0.00003	0.00003	0.00003	0.00003	0.00003	0.00003
Other production	0.00001	0.00001	0.00001	0.00001	0.00001	0.00001	0.00001	0.00001
Background modelling								
uds content	0.00236	0.00214	0.00221	0.00257	0.00191	0.00201	0.00217	0.00224
c content	0.00008	0.00008	0.00008	0.00009	0.00007	0.00007	0.00008	0.00008
Radiative hadronic	0.00136	0.00123	0.00127	0.00148	0.00110	0.00116	0.00125	0.00129
SM cross-sections								
Hadronic	0.00002	0.00002	0.00002	0.00002	0.00002	0.00002	0.00002	0.00002
W^+W^-/Z^0Z^0	0.00018	0.00016	0.00017	0.00020	0.00014	0.00015	0.00016	0.00017
ECAL calibration	0.00003	0.00003	0.00003	0.00003	0.00003	0.00003	0.00003	0.00003
MC statistics	0.00021	0.00019	0.00020	0.00023	0.00017	0.00018	0.00019	0.00020
Smearing parameters	0.00154	0.00140	0.00144	0.00167	0.00124	0.00131	0.00142	0.00146
Luminosity	0.00000	0.00000	0.00000	0.00000	0.00000	0.00000	0.00000	0.00000
Hemisphere tag correlation	0.00029	0.00026	0.00027	0.00031	0.00023	0.00024	0.00026	0.00027
Total	0.00731	0.00663	0.00682	0.00794	0.00589	0.00622	0.00671	0.00692

Table 8.3: All evaluated systematic errors and their totals for each energy with the calibrated event tag.

The final calibrated results for R_b and their statistical, systematic and total errors are shown in Table 8.4. The final values as a function of energy, together with previously published ALEPH results, are shown in Figure 8.2.

The final values for R_b at each energy point between 189 and 207 GeV are therefore presented as:

$$R_b \textbf{ at 188.6 GeV} = \mathbf{0.159 \pm 0.016 \ (stat) \pm 0.007 \ (syst)}$$

$$R_b \textbf{ at 191.6 GeV} = \mathbf{0.144 \pm 0.027 \ (stat) \pm 0.007 \ (syst)}$$

$$R_b \textbf{ at 195.5 GeV} = \mathbf{0.148 \pm 0.019 \ (stat) \pm 0.007 \ (syst)}$$

$$R_b \textbf{ at 199.5 GeV} = \mathbf{0.173 \pm 0.021 \ (stat) \pm 0.008 \ (syst)}$$

$$R_b \textbf{ at 201.6 GeV} = \mathbf{0.128 \pm 0.024 \ (stat) \pm 0.006 \ (syst)}$$

$$R_b \textbf{ at 204.9 GeV} = \mathbf{0.135 \pm 0.019 \ (stat) \pm 0.006 \ (syst)}$$

$$R_b \textbf{ at 206.5 GeV} = \mathbf{0.146 \pm 0.017 \ (stat) \pm 0.007 \ (syst)}$$

The mean weighted energy was calculated according to the total integrated luminosities used at each energy in this analysis, so that the final value for all 189 - 207 GeV data is:

$$R_b \textbf{ at 197.9 GeV} = \mathbf{0.151 \pm 0.012 \ (stat) \pm 0.007 \ (syst)}$$

The dominant error in these measurements of R_b is the statistical error. The individual systematic errors for each energy are shown in Table 8.3.

With the exception of 201.6 and 204.9 GeV all these results are all within one sigma of the Standard Model prediction, as shown in Figure 8.2. However the results for 201.6 and 204.9 GeV are well within 1.5 sigma of the Standard Model prediction. Additionally the result for all data combined is within 1.05 sigma of the Standard Model prediction. Thus it can be concluded that these results are in agreement with the theoretical predictions and are therefore not indicative of new physics.

Energy (GeV)	Calibrated event tag results			
	R_b	σ_{stat}	σ_{syst}	σ_{total}
189	0.15894	0.01571	0.00731	0.01733
192	0.14412	0.02708	0.00663	0.02788
196	0.14827	0.01938	0.00682	0.02055
200	0.17271	0.02089	0.00794	0.02235
202	0.12820	0.02397	0.00589	0.02468
205	0.13524	0.01898	0.00622	0.01997
207	0.14594	0.01655	0.00671	0.01786
189 - 207	0.15056	0.01195	0.00692	0.01381

Table 8.4: The calibrated event tag results for each LEP2 energy point between 189 and 207 GeV and all data combined. The statistical, systematic and total errors are also shown.

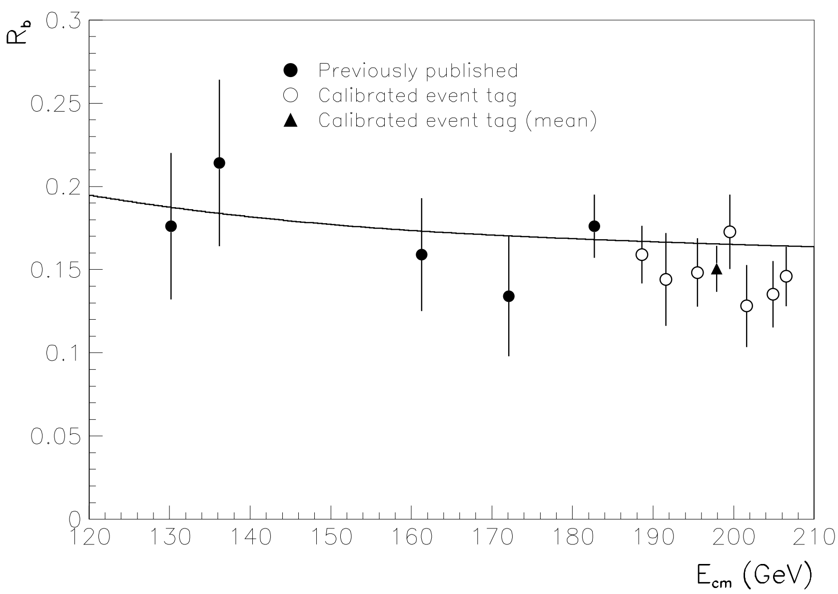

Figure 8.2: R_b at each energy and all data combined (189 - 207 GeV) measured with the calibrated event tag, plus the results previously published by ALEPH [3]. The Standard Model prediction for R_b as a function of energy is also shown.

Chapter 9

Conclusion

In this thesis the latest ALEPH measurements of the branching ratio R_b have been presented. Individual values of R_b were evaluated at each LEP2 energy point between 189 and 207 GeV. An improved analysis technique was employed, in which the hemisphere tag was used to calibrate the event tag, increasing the reliability of the measurements. Combining all the available statistics allowed the most statistically accurate LEP2 measurement of R_b with the ALEPH detector to be evaluated. The final combined result is:

$$R_b \textbf{ at 197.9 GeV} = \mathbf{0.151 \pm 0.012 \ (stat) \pm 0.007 \ (syst)}$$

which is within 1.05 sigma of the Standard Model prediction and therefore not indicative of new physics. As with earlier R_b measurements, this result may be used to further constrain the energy scales of new physics such as four-fermion contact interactions and supersymmetry. This result may also be combined with measurements from the other LEP experiments and thus contribute to a new world average value of R_b.

A comprehensive set of possible sources of systematic uncertainty was investigated. However, even with the combined statistics, the statistical error is dominant and therefore largely responsible for limiting the precision of the measurement. This is in contrast to the LEP1 measurements in which the systematic error dominated. As the LEP accelerator and ALEPH detector have now been dismantled to make way for the LHC, no more data will be collected and the measurement presented here therefore represents the final ALEPH measurement of R_b.

9.1 Future Outlook

Future measurements of R_b now rely on new accelerators. The LHC is scheduled to be online in 2007. However this is a proton-proton collider, with an emphasis on direct searches for new physics. The majority of interactions will be mediated by gluon-gluon fusion, so although $Z^0/\gamma \to b\bar{b}$ decays will occur, they will be swamped by direct $b\bar{b}$ production. It is unlikely therefore that measurements of R_b will be feasible at the LHC.

The next real opportunity for measurements are likely to be at the proposed Liner Collider [55]. This will be a 500 to 1000 GeV e^+e^- collider and will therefore considerably extend the reach for physics beyond the Standard Model. New high energy measurements of R_b will be possible, thus allowing even higher energies to be probed for new physics. However this machine will not be operational for at least a decade, and so it will be some time before new measurements of R_b will be available.

Appendix A

Calculation of R_b using a hemisphere tag

The fraction of single hemispheres tagged in data is defined as

$$f_{\mathrm{s}} = \frac{N_{\mathrm{sel}}}{N} \tag{A.1}$$

where N is the number of preselected hemispheres in data and N_{sel} is the number of selected hemispheres from the preselection for a given cut on the negative logarithm of the hemisphere probability. Taking into account the hadronic content and background, the number of selected hemispheres is given by:

$$N_{\mathrm{sel}} = N_{\mathrm{b}}\epsilon_{\mathrm{b}} + N_{\mathrm{c}}\epsilon_{\mathrm{c}} + N_{\mathrm{uds}}\epsilon_{\mathrm{uds}} + N_{\mathrm{w}}\epsilon_{\mathrm{w}} + N_{\mathrm{z}}\epsilon_{\mathrm{z}} + N_{\mathrm{q\,rad}}\epsilon_{\mathrm{q\,rad}} \tag{A.2}$$

where N_{b} is the number of hemispheres in the B preselection, ϵ_{b} is the B selection efficiency, and similarly for the other hadronic, W^+W^-, Z^0Z^0 and radiative hadronic contributions. Assuming the preselection efficiency for each of the hadronic flavours is the same, the branching ratio for a flavour f is defined as

$$R_f = \frac{N_{\mathrm{f}}}{N_{\mathrm{q}}} \tag{A.3}$$

where N_{q} is the total non-radiative hadronic preselection and N_{f} is the non-radiative preselection for hadronic flavour f. Dividing f_{s} through by N_{q} therefore gives

$$\frac{f_{\mathrm{s}}}{N_{\mathrm{q}}} = \frac{R_b\epsilon_{\mathrm{b}} + R_c\epsilon_{\mathrm{c}} + R_{uds}\epsilon_{\mathrm{uds}}}{N} + \frac{N_{\mathrm{w}}\epsilon_{\mathrm{w}} + N_{\mathrm{z}}\epsilon_{\mathrm{z}} + N_{\mathrm{q\,rad}}\epsilon_{\mathrm{q\,rad}}}{N_{\mathrm{q}}N} \tag{A.4}$$

Below the threshold for top production, R_{uds} is defined as

$$R_{uds} = (1 - R_b - R_c) \tag{A.5}$$

so that the fraction of single hemispheres tagged is given by

$$f_\mathrm{s} = \frac{R_b\epsilon_\mathrm{b} + R_c\epsilon_\mathrm{c} + (1 - R_b - R_c)\,\epsilon_\mathrm{uds}}{(N/N_\mathrm{q})} + \frac{N_\mathrm{w}\epsilon_\mathrm{w} + N_\mathrm{z}\epsilon_\mathrm{z} + N_\mathrm{q\,rad}\epsilon_\mathrm{q\,rad}}{N} \tag{A.6}$$

The fraction of *events* with both hemispheres tagged in data is defined as

$$f_\mathrm{d} = \frac{N^\mathrm{e}_\mathrm{sel}}{N^\mathrm{e}} \tag{A.7}$$

where N^e is the number of preselected events in data and $N^\mathrm{e}_\mathrm{sel}$ is the number of selected events from the preselection with both hemispheres tagged. As the efficiency for tagging both hemispheres in an event is simply the square of the efficiency for tagging one hemisphere, the number of selected events for a given cut on the b-tag is defined as

$$N^\mathrm{e}_\mathrm{sel} = N^\mathrm{e}_\mathrm{b}\epsilon^2_\mathrm{b} + N^\mathrm{e}_\mathrm{c}\epsilon^2_\mathrm{c} + N^\mathrm{e}_\mathrm{uds}\epsilon^2_\mathrm{uds} + N^\mathrm{e}_\mathrm{w}\epsilon^2_\mathrm{w} + N^\mathrm{e}_\mathrm{z}\epsilon^2_\mathrm{z} + N^\mathrm{e}_\mathrm{q\,rad}\epsilon^2_\mathrm{q\,rad} \tag{A.8}$$

Dividing $N^\mathrm{e}_\mathrm{sel}$ by N^e_q and proceeding as before, the fraction of events with both hemispheres tagged is given by

$$f_\mathrm{d} = \frac{R_b\epsilon^2_\mathrm{b}\,(1 + \rho_b) + R_c\epsilon^2_\mathrm{c} + (1 - R_b - R_c)\,\epsilon^2_\mathrm{uds}}{\left(N^\mathrm{e}/N^\mathrm{e}_\mathrm{q}\right)} + \frac{N^\mathrm{e}_\mathrm{w}\epsilon^2_\mathrm{w} + N^\mathrm{e}_\mathrm{z}\epsilon^2_\mathrm{z} + N^\mathrm{e}_\mathrm{q\,rad}\epsilon^2_\mathrm{q\,rad}}{N^\mathrm{e}} \tag{A.9}$$

where the B hemisphere tagging correlation correction factor ρ_b is defined as:

$$\rho_b = \frac{\epsilon^\mathrm{d}_\mathrm{b} - \epsilon^2_\mathrm{b}}{\epsilon^2_\mathrm{b}} \tag{A.10}$$

where ϵ_b is the B hemisphere tagging efficiency and $\epsilon^\mathrm{d}_\mathrm{b}$ is the efficiency for tagging both hemispheres in a B event, both of which are estimated from the Monte Carlo.

The expressions for f_s and f_d can then be solved simultaneously for R_b and ϵ_b. Rearranging Equation A.6 for R_b gives:

$$R_b = \left[\left(f_\mathrm{s} - \frac{N_\mathrm{w}\epsilon_\mathrm{w} + N_\mathrm{z}\epsilon_\mathrm{z} + N_\mathrm{q\,rad}\epsilon_\mathrm{q\,rad}}{N}\right)\left(\frac{N}{N_\mathrm{q}}\right) - R_c\epsilon_\mathrm{c} - \epsilon_\mathrm{uds} + R_c\epsilon_\mathrm{uds}\right](\epsilon_\mathrm{b} - \epsilon_\mathrm{uds})^{-1} \tag{A.11}$$

Rearranging Equation A.9 for R_b gives:

$$R_b = \left[\left(f_{\mathrm{d}} - \frac{N^{\mathrm{e}}_{\mathrm{w}}\epsilon^2_{\mathrm{w}} + N^{\mathrm{e}}_{\mathrm{z}}\epsilon^2_{\mathrm{z}} + N^{\mathrm{e}}_{\mathrm{q\,rad}}\epsilon^2_{\mathrm{q\,rad}}}{N^{\mathrm{e}}}\right)\left(\frac{N^{\mathrm{e}}}{N^{\mathrm{e}}_{\mathrm{q}}}\right) - R_c\epsilon^2_{\mathrm{c}} - \epsilon^2_{\mathrm{uds}} + R_c\epsilon^2_{\mathrm{uds}}\right]\left(\epsilon^2_{\mathrm{b}}\left(1+\rho\right) - \epsilon^2_{\mathrm{uds}}\right)^{-1} \tag{A.12}$$

Setting Equations A.11 and A.12 equal and solving for ϵ_{b} leads to:

$$\epsilon_{\mathrm{b}} = \frac{-B \pm \left(B^2 - 4AC\right)^{\frac{1}{2}}}{2A} \tag{A.13}$$

where

$$A = \left[\left(f_{\mathrm{s}} - \frac{N_{\mathrm{w}}\epsilon_{\mathrm{w}} + N_{\mathrm{z}}\epsilon_{\mathrm{z}} + N_{\mathrm{q\,rad}}\epsilon_{\mathrm{q\,rad}}}{N}\right)\left(\frac{N}{N_{\mathrm{q}}}\right) - R_c\epsilon_{\mathrm{c}} - \epsilon_{\mathrm{uds}} + R_c\epsilon_{\mathrm{uds}}\right]\left(1+\rho\right) \tag{A.14}$$

$$B = \left(f_{\mathrm{d}} - \frac{N^{\mathrm{e}}_{\mathrm{w}}\epsilon^2_{\mathrm{w}} + N^{\mathrm{e}}_{\mathrm{z}}\epsilon^2_{\mathrm{z}} + N^{\mathrm{e}}_{\mathrm{q\,rad}}\epsilon^2_{\mathrm{q\,rad}}}{N^{\mathrm{e}}}\right)\left(\frac{N^{\mathrm{e}}}{N^{\mathrm{e}}_{\mathrm{q}}}\right) - R_c\epsilon^2_{\mathrm{c}} - \epsilon^2_{\mathrm{uds}} + R_c\epsilon^2_{\mathrm{uds}} \tag{A.15}$$

$$C = \epsilon_{\mathrm{uds}}\left(B - \frac{A\epsilon_{\mathrm{uds}}}{1+\rho}\right) \tag{A.16}$$

The value for ϵ_{b} from Equation A.13 can then be substituted into Equation A.11 or Equation A.12 for R_b.

Appendix B

Equality of errors

The final result for R_b at each energy i is defined as:

$$(R_b^{\mathrm{f}})_{\mathrm{i}} \;=\; (R_b^{\mathrm{e}})_{\mathrm{i}} \times C \;=\; (R_b^{\mathrm{e}})_{\mathrm{i}} \times \frac{(R_b^{\mathrm{h}})_{\mathrm{all}}}{(R_b^{\mathrm{e}})_{\mathrm{all}}} \tag{B.1}$$

where $(R_b^{\mathrm{e}})_{\mathrm{i}}$ is R_b measured with the event tag at energy i, and $(R_b^{\mathrm{h}})_{\mathrm{all}}$, $(R_b^{\mathrm{e}})_{\mathrm{all}}$ are R_b measured with the hemisphere and event tags respectively for all data 189 - 207 GeV. If $(R_b^{\mathrm{e}})_{\mathrm{i}} = (R_b^{\mathrm{e}})_{\mathrm{all}}$ then by definition the value for $(R_b^{\mathrm{h}})_{\mathrm{all}}$ is recovered. However the error on $(R_b^{\mathrm{h}})_{\mathrm{all}}$ should also be recovered, which can be proved as follows.

If Equation B.1 is rewritten as:

$$R \;=\; \frac{R_1 R_2}{R_3} \tag{B.2}$$

then

$$\begin{aligned}
\sigma_R^2 \;=\;& \left(\frac{\partial R}{\partial R_1}\right)^2 \sigma_{R_1}^2 + \left(\frac{\partial R}{\partial R_2}\right)^2 \sigma_{R_2}^2 + \left(\frac{\partial R}{\partial R_3}\right)^2 \sigma_{R_3}^2 \\
&+\; 2\rho_{R_1R_2} \left(\frac{\partial R}{\partial R_1}\right)\left(\frac{\partial R}{\partial R_2}\right) \sigma_{R_1}\sigma_{R_2} \\
&+\; 2\rho_{R_1R_3} \left(\frac{\partial R}{\partial R_1}\right)\left(\frac{\partial R}{\partial R_3}\right) \sigma_{R_1}\sigma_{R_3} \\
&+\; 2\rho_{R_2R_3} \left(\frac{\partial R}{\partial R_2}\right)\left(\frac{\partial R}{\partial R_3}\right) \sigma_{R_2}\sigma_{R_3}
\end{aligned} \tag{B.3}$$

so that evaluating the partial differentials:

$$\begin{aligned}\left(\frac{\sigma_R}{R}\right)^2 &= \left(\frac{\sigma_{R_1}}{R_1}\right)^2 + \left(\frac{\sigma_{R_2}}{R_2}\right)^2 + \left(\frac{\sigma_{R_3}}{R_3}\right)^2 \\ &+ 2\rho_{R_1R_2}\left(\frac{\sigma_{R_1}}{R_1}\right)\left(\frac{\sigma_{R_2}}{R_2}\right) \\ &- 2\rho_{R_1R_3}\left(\frac{\sigma_{R_1}}{R_1}\right)\left(\frac{\sigma_{R_3}}{R_3}\right) \\ &- 2\rho_{R_2R_3}\left(\frac{\sigma_{R_2}}{R_2}\right)\left(\frac{\sigma_{R_3}}{R_3}\right) \end{aligned} \tag{B.4}$$

For the case where $(R_b^{\mathrm{e}})_{\mathrm{i}} = (R_b^{\mathrm{e}})_{\mathrm{all}}$ then from comparing Equations B.1 and B.2:

$$R_1 = R_3 \tag{B.5}$$

so that $\sigma_{R_1} = \sigma_{R_3}$, $\rho_{R_1R_2} = \rho_{R_2R_3}$, $\rho_{R_1R_3} = 1$ and $R = R_2$. Substituting these equalities into Equation B.4 leads to:

$$\begin{aligned}\left(\frac{\sigma_R}{R}\right)^2 &= \left(\frac{\sigma_{R_1}}{R_1}\right)^2 + \left(\frac{\sigma_{R_2}}{R_2}\right)^2 + \left(\frac{\sigma_{R_1}}{R_1}\right)^2 \\ &+ 2\rho_{R_1R_2}\left(\frac{\sigma_{R_1}}{R_1}\right)\left(\frac{\sigma_{R_2}}{R_2}\right) \\ &- 2\left(\frac{\sigma_{R_1}}{R_1}\right)\left(\frac{\sigma_{R_1}}{R_1}\right) \\ &- 2\rho_{R_2R_1}\left(\frac{\sigma_{R_2}}{R_2}\right)\left(\frac{\sigma_{R_1}}{R_1}\right) \end{aligned} \tag{B.6}$$

which reduces to:

$$\left(\frac{\sigma_R}{R}\right)^2 = \left(\frac{\sigma_{R_2}}{R_2}\right)^2 \tag{B.7}$$

With $R = R_2$ then $\sigma_R = \sigma_{R_2}$. Therefore scaling the event tag result for all data combined should result not only in the same value as R_b measured with the hemisphere tag for all data combined but, as expected, the same error as well.

References

[1] I. Tomalin *et al.*, “A measurement of R_b using a Lifetime-Mass Tag”, European Organisation for Nuclear Research, CERN-PPE/97-017.

[2] M. Caccia, “Measurements of R_b and R_c at LEP”, *Nucl. Phys. B* **75** (1999) 246-252.

[3] ALEPH Collaboration, I. Tomalin *et el.*, “Study of Fermion Pair Production in e^+e^- Collisions at 130 - 183 GeV”, Tech. Rep. ALEPH 98-060, ALEPH internal report 1998.

[4] R. Brun, O. Couet, C. Varidoni and P. Zanarini, “PAW Physics Analysis Workstation”, CERN program library entry **Q121**.

[5] S. L. Glashow, “Partial Symmetries of weak interactions”, *Nucl. Phys.* **B22** (1961) 579-588.
S. Weinberg, “A model of leptons”, *Phys. Rev. Lett* **19** (1967) 1264-1266.
A. Salam, “Elementary particle theory”, Proceedings of the 8th Nobel Symposium, p367, ed. Svartholm, Almqvist and Wiksell, Stockholm 1968.

[6] S. L. Glashow, I. Iliopoulos and L. Maiani, “Weak interactions with lepton-hadron symmetry”, *Phys. Rev.* **D2** (1970) 1285-1292.

[7] H. Y. Han and Y. Nambu, “Three triplet model with double SU(2) symmetry”, *Phys. Rev.* **B139** (1965) 1006-1010.

[8] Particle Data Group, “Particle Physics Booklet”, July 2002.

[9] The ALEPH collaboration, “Final results of the searches for neutral Higgs bosons in e^+e^- collisions at $\sqrt{s}$ up to 209 GeV”, *Phys. Lett.* **B526** (2002) 191-205.

[10] G. W. F. Drake, S. P. Goldman and A. van Wijngaarden, "$He^{\pm}$ Lamb-shift measurement by the quenching-radiation anisotropy method", *Phys. Rev.* **A20** 1299.

[11] P. M. Watkins, "Proceedings of the School for Young High Energy Physicists", Rutherford Appleton Laboratory, RAL-TR-2001-016.

[12] N. Ellis and J. March-Russell, "2001 European School of High Energy Physics", Eurepean Organisation for Nuclear Research, CERN 2002-002.

[13] R. R. White, "Search for the Standard Model Higgs Boson in the Missing Mass Channel at the ALEPH experiment", Ph.D Thesis, Imperial College London 2001.

[14] The Super-Kamiokande Collaboration, "Atmospheric Neutrino Results from Super-Kamiokande", Paper submitted to ICHEP2000.

[15] N. Cabbibo, *Phys. Rev. Lett* **10** (1963) 10. M. Kobayashi and K. Maskawa, *Prog. Theor. Phys* **49** (1973) 652.

[16] J. Ellis, "Beyond the Standard Model for Hillwalkers", European Organisation for Nuclear Research, CERN-TH/98-329.

[17] R. S. Chivukula and J. Wormersley, "Dynamical Electroweak Symmetry Breaking", *The European Physical Journal* **C15** (2000) 1.

[18] D. Griffiths, "Introduction to elementary particles", John Wiley and Sons (1987), p198.

[19] P. B. Renton, "Electroweak interactions", Cambridge University Press (1990).

[20] ALEPH Collaboration, I. Tomalin *et al.*, "Fermion pair production in e^+e^- Collisions at 189 GeV and limits on physics beyond the Standard Model", Tech. Rep. ALEPH 99-018, ALEPH internal report 1999.

[21] ALEPH Collaboration, D.Decamp *et al.*, "ALEPH: A Detector for electron-positron annihilations at LEP", *Nucl. Instrum. Meth.* **A294** (1990) 121-178.

[22] S. Myers and E. Picasso, "The Design, Construction and Commissioning of the CERN Large Electron Positron Collider", *Contemp. Phys.* **31** (1990) 387.

[23] The LHC Study Group, "THE LARGE HADRON COLLIDER Conceptual Design Report", European Organisation for Nuclear Research, CERN/AC/95-05(LHC).

[24] OPAL Collaboration, K. Ahmet *et al.*, "The OPAL detector at LEP", *Nucl. Instrum. Meth.* **A305** (1991) 275-319.

[25] DELPHI Collaboration, P. Aarnio *et al.*, "The DELPHI detector at LEP", *Nucl. Instrum. Meth.* **A303** (1991) 233-276.

[26] L3 Collaboration, "The construction of the L3 experiment", *Nucl. Instrum. Meth.* **A289** (1990) 35.

[27] ALEPH Collaboration, "The ALEPH Handbook 1999 Vol. 1", European Organisation for Nuclear Research, CERN, Geneva, 1995.
ALEPH Collaboration, "The ALEPH Handbook 1999 Vol. 2", European Organisation for Nuclear Research, CERN, Geneva, 1995.

[28] ALEPH Collaboration, D. Buskulic *et al.*, "Performance of the ALEPH Detector at LEP", *Nucl. Instrum. Meth.* **A360** (1995) 481-506.

[29] D. Creanza *et al.*, "The new ALEPH Silicon Vertex Detector", *Nucl. Instrum. Meth.* **A409** (1998) 157.

[30] G. J. Barber *et al.*, "Performance of the Three-Dimensional Readout of the ALEPH Inner Tracking Chamber", *Nucl. Instrum. Meth.* **A279** (1989) 212.

[31] W. B. Atwood *et al.*, "Performance of the ALEPH Time Projection Chamber", *Nucl. Instrum. Meth.* **A306** (1991) 446-458.

[32] J. Knobloch, "`JULIA` Users and Programmers Guide", Tech. Rep. ALEPH 90-11, ALEPH internal report 1990.

[33] Kalman, Rudolph, Emil, "A new approach to Linear Filtering and Prediction Problems", Transactions of the ASME, **82(D)** (1960) 35-45.

[34] T. Sjostrand *et al.*, "High-energy-physics event generation with `PYTHIA` 5.7 and `JETSET` 7.4", *Comp. Phys. Comm.* **82** (1994) 74-89.

[35] S. Jadach, B.F.L. Ward and Z. Was, "The Precision Monte Carlo Event Generator $\mathcal{KK}$ For Two-Fermion Final States In e^+e^- Collisions", *Comp. Phys. Comm.* **130(3)** (2000) 260-325.

[36] T. Sjostrand *et al.*, "High-energy-physics event generation with Pythia 6.1", *Comp. Phys. Comm.* **135(2)** (2001) 238-259.

[37] S. Jadach, B.F.L. Ward and Z. Was, "The Monte Carlo program `KORALZ` version 4.0 for the lepton or quark pair production at LEP/SLC energies", *Comp. Phys. Comm.* **79** (1994) 503.

[38] S. Jadach, W. Placzek, M. Skrzypek, B. F. L. Ward and Z. Was, "The Monte Carlo Program `KoralW` version 1.51 and The Concurrent Monte Carlo `KoralW` &`YFSWW3` with All Background Graphs and First-Order Corrections to W-Pair Production", *Comp. Phys. Comm.* **140(3)** (2001) 475-512.

[39] J.E. Campagne and R. Zitoun, "The `DYMU2` Event Generator", *Z. Phys.* **C43** (1989) 469.

[40] F. Ranjard, "`GALEPH`- Monte Carlo program for ALEPH", Tech. Rep. ALEPH 88-119, ALEPH internal report 1988.

[41] R. Brun, F. Bruyant, M. Maire, A. C. McPherson and P. Zanarini, "GEANT3", European Organisation for Nuclear Research, CERN-DD/EE/84-1.

[42] H. Albrecht, E. Blucher and J. Boucrot *et al.*, "ALEPH PHYSICS ANALYSIS PACKAGE", Tech. Rep. ALEPH 99-087, ALEPH internal report 1999.

[43] `JADE` collaboration, W. Bartel *et al.*, "Experimental studies on Multi-jet Production in e^+e^- Annihilation at PETRA energies", *Z. Phys.* **C33** (1986) 23.

[44] D. Brown *et al.*, "`QFNDIP`, a primary vertex finder", Tech. Rep. ALEPH 92-047, ALEPH internal report 1992.

[45] B. Bloch-Deveux, "Run Selection and Luminosity", http://alephwww.cern.ch/~sical/Wlumi/.

[46] ALEPH Collaboration, D. Buskulic *et al.*, "Heavy Flavour Production and Decay with Prompt Leptons in the ALEPH Detector", *Z. Phys.* **C62** (1994) 179.

[47] ALEPH Collaboration, D. Buskulic *et al.*, "Measurement of the ratio $\frac{Z\to b\bar{b}}{Z\to \mathrm{Hadrons}}$ using event shape variables", *Phys. Lett.* **B313** (1993) 549.

[48] D. Brown and M. Frank, "Tagging b hadrons using track impact parameters", Tech. Rep. ALEPH 92-135, ALEPH internal report 1992.

[49] R. Barlow, "Statistics: A Guide to the Use of Statistical Methods in the Physical Sciences", John Wiley and Son Ltd 1993, p45.

[50] D. Bardin *et al.*, "ZFITTER A Semi-Analytical Program for Fermion Pair Production in e^+e^- Annihilation", Tech. Rep. DESY 99-070, DESY internal report 1999.

[51] C. Goy, "Measurement of R_b and A^b_{FB} at $\sqrt{S}$ = 189 GeV/c^2. Update with respect Winter/Summer conference note.", Tech. Rep. ALEPH 99-106, ALEPH internal report.

[52] LEP Heavy Flavour Working Group, "Input Parameters for the LEP/SLD Electroweak Heavy Flavour Results for Summer 1998 Conferences", LEPHF/98-01.

[53] G. Altarelli, T. Sjostrand and F. Zwirner, "Physics at LEP2 (Volume 2)", European Organisation for Nuclear Research, CERN 96-01.

[54] Reported in a private communication with Corinne Goy (ALEPH Collaboration).

[55] International Linear Collider Technical Review Committee, "Second Report", ILC-TRC/2003.